Laser-hybrid Accelerator for Radiobiological Applications (LhARA)

Conceptual Design Report

G. Aymar[1], T. Becker[2], S. Boogert[3], M. Borghesi[4], R. Bingham[5a], C. Brenner[1], P. Burrows[6], O.C. Ettlinger[7], T. Dascalu[7], S. Gibson[3], T. Greenshaw[8], S. Gruber[9], D. Gujral[10], C. Hardiman[10], J. Hughes[8], W.G. Jones[7b], K. Kirkby[11], A. Kurup[7†], J-B. Lagrange[1], K. Long[7a], W. Luk[7], J. Matheson[1], P. Mckenna[5], R. Mclauchlan[10], Z. Najmudin[7], H.T. Lau[7], J. Parsons[8], J. Pasternak[7a], J. Pozimski[7a], K. Prise[4], P. Ratoff[12], G. Schettino[13c], W. Shields[3], S. Smith[14], J. Thomason[1], S. Towe[15], P. Weightman[8], C. Whyte[5], R. Xiao[16]

1. *STFC Rutherford Appleton Laboratory, Harwell Oxford, Didcot, OX11 0QX, UK*
2. *Maxeler technologies Limitted, 3 Hammersmith Grove, London W6 0ND, UK*
3. *Royal Holloway, University of London, Egham, Surrey, TW20 0EX, UK*
4. *Queens University Belfast, University Road, Belfast, BT7 1NN, Northern Ireland, UK*
5. *University of Stratchclyde, 16 Richmond Street, Glasgow, G1 1XQ, UK*
6. *The John Adams Institute, Denys Wilkinson Building, Keble Road, Oxford OX1 3RH, UK*
7. *Imperial College London, Exhibition Road, London, SW7 2AZ, UK*
8. *University of Liverpool, Liverpool L69 3BX, UK*
9. *Christian Doppler Laboratory for Medical Radiation Research for Radiation Oncology, Medical University of Vienna, Spitalgasse 23, 1090 Vienna, Austria*
10. *Imperial College NHS Healthcare Trust, The Bays, South Wharf Road, St Mary's Hospital, London W2 1NY, UK*
11. *University of Manchester, Oxford Road, Manchester, M13 9PL, UK*
12. *The Cockcroft Institute Daresbury Laboratory, Sci-Tech Daresbury, Daresbury, Warrington, WA4 4AD, UK*
13. *National Physical Laboratory, Hampton Road, Teddington, Middlesex, TW11 0LW, UK*
14. *STFC Daresbury Laboratory, Daresbury, Cheshire, WA4 4AD, UK*
15. *Leo Cancer Care, Broadview, Windmill Hill, Hailsham, East Sussex, BN27 4RY, UK*
16. *Cororain, 14F, Changfu Jinmao Building(CFC), Trade-free Zone, Futian District, Shenzhen, Guangdong, China*

a. *Also at STFC Rutherford Appleton Laboratory, Harwell Oxford, Didcot, OX11 0QX, UK*
b. *Also at Imperial Patient and Public Involvement Group (IPPIG), Imperial College London, Exhibition Road, London, SW7 2AZ, UK*
c. *Also at University of Surrey, 388 Stag Hill, Guilford, GU2 7XH, UK*
† *Corresponding author, Email: a.kurup@imperial.ac.uk*

Executive summary

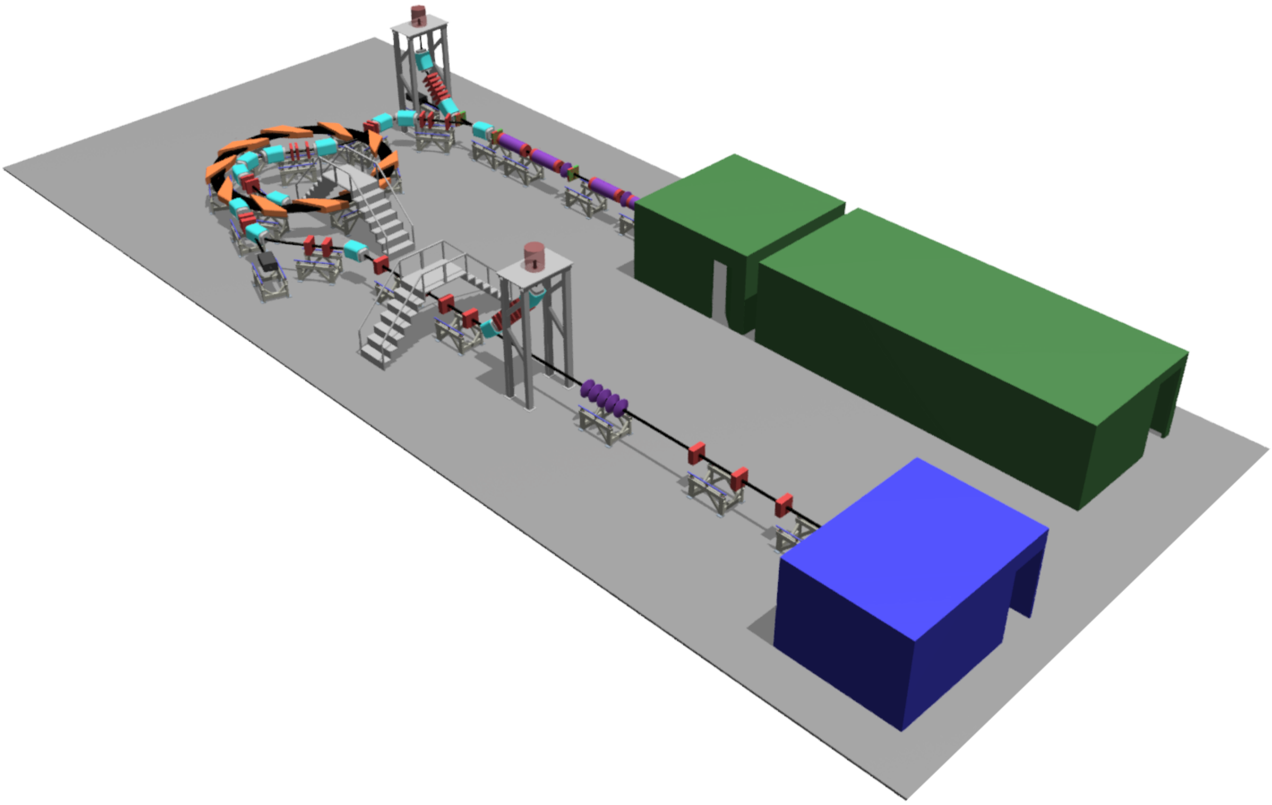

Figure 1: LhARA—the Laser-hybrid Accelerator for Radiobiological Applications.

Cancer is the second most common cause of death globally [1]. In 2018, 18.1 million new cancer cases were diagnosed, 9.6 million people died of cancer-related disease, and 43.8 million people were living with cancer [2, 3]. It is estimated that 26.9 million life-years could be saved in low- and middle-income countries (LMIC) if radiotherapy capacity could be scaled up [4]. Novel techniques incorporated in facilities that are at once robust, automated, efficient, and cost-effective are required to deliver the required scale-up in provision.

Radiation therapy (RT), a cornerstone of cancer treatment, is used in over 50% of cancer patients [5]. The most frequently used types of radiotherapy employ photon or electron beams with MeV-scale energies. Proton and ion beams offer substantial advantages over X-rays because the bulk of the beam energy is deposited in the Bragg peak. This allows dose to be conformed to the tumour while sparing healthy tissue and organs at risk.

The benefits of proton and ion-beam therapy (PBT) are widely recognised. There are approximately 88 PBT centres worldwide, and at least 40 under construction [6]. PBT today is routinely delivered in fractions of ~ 2 Gy per day over several weeks. Usually, each fraction is delivered at a low dose rate (< 10 Gy/min) deposited uniformly over the target treatment volume. Exciting evidence of therapeutic benefit has recently been reported when dose is delivered at ultra-high dose-rate, $\gtrsim 40$ Gy/s (“FLASH” RT) [7, 8], or provided in multiple micro-beams with diameter less than 1 mm distributed over a grid with inter-beam spacing of ~ 3 mm [9]. However, the radiobiological mechanisms by which the therapeutic benefit is generated are not properly understood.

LhARA, the Laser-hybrid Accelerator for Radiobiological Applications, is conceived as the new, highly flexible, source of radiation that is required to explore the vast “terra incognita” of the mechanisms by which the biological response to ionising radiation is determined by the physical characteristics of the beam [10]. The LhARA collaboration’s concept, shown in figure 1, is to exploit a laser to drive the creation of a large flux of protons or light ions which are captured and formed into a beam by strong-focusing plasma lenses. The laser-driven source allows protons and ions to be captured at energies significantly above the proton- and ion-capture energies that pertain in conventional facilities, thereby evading the current space-charge limit on the instantaneous dose rate that can be delivered [11]. The plasma (Gabor) lenses provide the same focusing strength as high-field solenoids at a fraction of the cost. Post-acceleration, performed using a fixed field alternating gradient accelerator (FFA), will preserve the unique flexibility in the time, energy, and spatial structure of the beam afforded by the laser-driven source.

We propose that LhARA be developed in two stages. In the first stage, the laser-driven beam, captured and transported using plasma lenses and bending magnets, will serve a programme of in-vitro experiments with proton beams of energy of up to 15 MeV. In stage two, the beam will be accelerated using an FFA. This will allow experiments to be carried out in vitro and in vivo with proton-beam energies of up to 125 MeV. Ion beams (including C^{6+}) with energies up to 30 MeV per nucleon will also be available. Figure 2 compares the energy and estimated maximum instantaneous dose rate of LhARA to the performance of other clinical and laboratory facilities that provide, or plan to provide, proton and ion beams for radiobiology. The beam energy at LhARA has been specified to allow in-vitro experiments and in-vivo studies using small mammals. The LhARA collaboration's hybrid approach will allow the unique properties of the laser-driven source—extremely high instantaneous flux in an extremely sort pulse over a tiny area—to be preserved and exploited to deliver radiobiological investigations in completely new regimes.

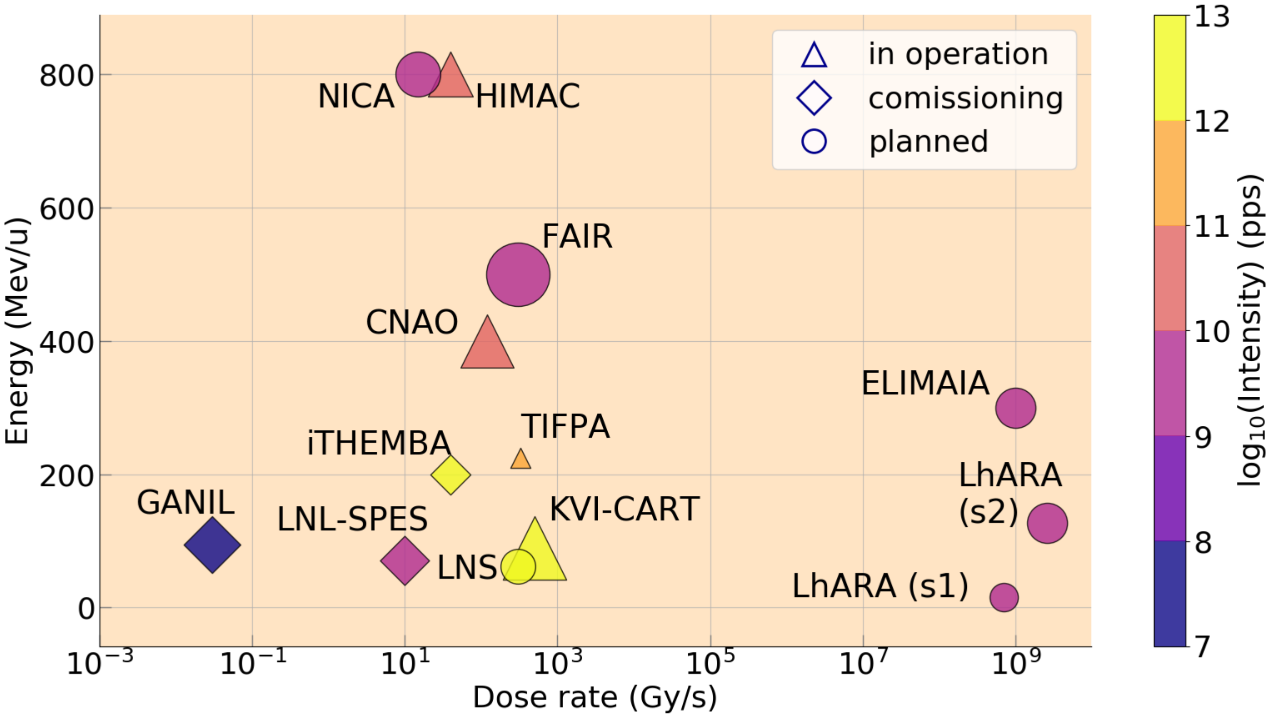

Figure 2: Comparison of the projected performance of LhARA at Stage 1 (S1) and Stage 2 (S2) with the performance of other facilities that provide, or plan to provide, beams for radiobiology [12–30]. The energy of the beam provided is plotted against the maximum instantaneous dose. The range of ion species that are provided by the facility is indicated by the relative size of the marker.

LhARA will not be developed or operate in isolation. Proton and ion beams for radiobiological research are available at a number of laboratories in Europe, the Americas, Africa, and in Asia. A number of clinical proton- and ion-beam centres (e.g. [22, 24]) also provide beams for research. Beam time for radiobiology at research laboratories is often restricted by the pressure of other users while time to do research at clinical facilities is limited by the demands of patient treatment. A small number of laboratories in Europe actively seek to develop laser-driven sources for biomedical applications (e.g. [21]). The LhARA collaboration's vision is to build on this work to demonstrate the feasibility of capturing and manipulating the flux created in the laser-target interaction to provide a beam that can be accelerated rapidly to the desired energy.

The laser pulse that initiates the production of protons or ions at LhARA may be triggered at a repetition rate of up to 10 Hz. The time structure of the beam may therefore be varied to interrupt the chemical and biological pathways that determine the biological response to ionising radiation with 10 ns to 40 ns long proton or ion bunches repeated at intervals as small as 100 ms. The technologies chosen to capture, transport, and accelerate the beam in LhARA have been made so that this unique capability is preserved. The LhARA beam may be used to deliver an almost uniform dose distribution over a circular area with a maximum diameter of between 1 cm and 3 cm. Alternatively the beam can be focused to a spot with diameter of $\sim$ 1 mm. The key features of LhARA for the study of radiobiology will be:

- *Flexibility*: to provide a wide variety of temporal, spectral, and spatial beam structures to enable exhaustive investigation of the impact of beam parameters on the micro-biophysical processes that determine the response of living tissue to ionising radiation.
- *Low beam divergence*: as it enters the in-vitro and the in-vivo end-stations is a feature of the optical design of the facility. This will be an important advantage in the study of spatially fractionated radiotherapy.
- *Multiple ion species*: will be provided over a variety of temporal and spatial distributions in a single facility to allow direct comparison of the radiobiological impact of the different species and provide a means to assess their relative benefits for therapy.
- *Availability*: the specification of the laser-driven source has been made to allow the dose delivered to the biological samples to be accurate and reproducible. This, combined with the fact that LhARA will be a facility dedicated to the study of radiobiology will allow the assessment of temporal and spatial fractionation schemes in combination with immunotherapy and chemotherapy and the evaluation of the relative biological effectiveness using complex endpoints such as angiogenesis, inflammation etc.

The development of LhARA will drive advances in technique with application well beyond the study of radiobiology. By establishing LhARA, the research programme will:

- Prove the feasibility of the laser-hybrid technique, evading the instantaneous flux limit imposed by the space-charge effect in current proton and ion sources;
- Demonstrate that electron-plasma lenses are a viable alternative to high-field solenoids for the capture and transport of proton and ion beams;
- Demonstrate through operation that a fixed field alternating gradient accelerator with variable extraction energy is capable of the routine acceleration of proton and ion beams in a production facility; and
- Integrate real-time dose-deposition imaging in a fast feedback and control system to demonstrate the reproducible delivery of dose using a laser-hybrid accelerator system.

The technologies demonstrated in LhARA have the potential to be developed to make "best in class" treatments available to the many by reducing the footprint of future particle-beam therapy systems. The laser-hybrid approach, therefore, will allow radiobiological studies and eventually radiotherapy to be carried out in completely new regimes, delivering a variety of ion species in a broad range of time structures and spatial configurations at instantaneous dose rates up to and potentially significantly beyond the current ultra-high dose-rate "FLASH" regime.

The LhARA consortium is the multidisciplinary collaboration of clinical oncologists, medical and academic physicists, biologists, engineers, and industrialists required to deliver such a transformative particle-beam system. With this "pre Conceptual Design Report" (pre-CDR) we seek to lay out our concept for LhARA, its potential to serve a ground-breaking programme of radiobiology, and the technological advances that will be made in its execution. The work presented in the LhARA pre-CDR lays the foundations for the development of full conceptual and technical designs for the facility. The pre-CDR also contains a description of the R&D that is required to demonstrate the feasibility of critical components and systems. An initial cost and schedule exercise has been carried out. This analysis shows that the first radiobiological experiments could be carried out within five years of the start of the LhARA project if appropriate resources can be secured.

Lay summary

For many years the delivery of radiotherapy in the treatment of cancer has involved directing a beam of high-energy photons (X-rays) at cancer tumours, to kill the cancer cells. This has proved to be a very successful treatment for many cancers. However, it has the disadvantage that the photons in the beam not only kill cells in the tumour but also damage cells in the healthy tissue through which the the beam passes. Further damage can occur outside the beam because the photons can scatter as they pass through the patient. To reduce the severity of these unwanted effects requires that the X-ray dose delivered to the tumour is limited to avoid giving too high a dose to healthy tissues. Damage to healthy tissue can further be reduced by concentrating the photons on the tumour using beams directed from different angles, in a kind of cross-fire. This is achieved by rotating the source of the photons around the patient.

More recently a different type of radiotherapy "proton beam radiotherapy" has been developed. In this form of treatment a beam of high-energy protons (rather than photons) is directed at the tumour. The main advantage of using beams of protons is that they cause very little damage until they come to the end of their range at which point they deliver an enhanced dose by ionising atoms in a very small volume. The energy of the proton beams can be adjusted so that they stop within the tumour. This has the advantage that very little damage is done to the healthy tissue outside the tumour. Such proton machines need a very large and expensive proton accelerator to produce the beam, so there are very few of them in most countries. Moreover, because they are extremely large it is difficult to vary the angle of the beam (which is sometimes necessary) and also difficult to ensure that the proton beam stops exactly where required in the body.

Research shows that there is a significant advantage in delivering the protons as a series high intensity bunches and also in the form of several very narrow closely-spaced "micro beams". Other investigations underway at present involve the use of ions heavier than protons such as helium or carbon. These are exciting developments as they point to more effective destruction of cancer cells whilst also reducing damage to healthy cells. However, they also highlight the need to improve our understanding of the basic mechanisms by which protons and heavy ions generate biological impact. Thus, the most important aim of LhARA is to pursue this radiobiology research in new regimes to inform and help develop better treatments. The other aspect of LhARA is technological research to replace the large and expensive proton accelerator with a high-powered laser-based accelerator. This would prove to be more flexible, less expensive and better able to produce the very short intense pulses needed.

To summarise, the LhARA proposal is a crucial first step in a full R&D programme to transform proton beam therapy by enabling more effective higher doses to be given safely and accurately. It will also significantly benefit cancer patients by reducing their course of radiotherapy treatment to days rather than several weeks, as well as almost eliminating the risk of damage to the healthy tissue that surrounds the tumour. This requires (a) scientific research to explore radiobiology in new regimes and (b) research into the physics and technology of laser-hybrid proton accelerators in order to produce new machines.

W.G. Jones on behalf of the Imperial Patient and Public Involvement Group (IPPIG).

1 Introduction and motivation

Background and context

Cancer is a major cause of death with 17 million new cases each year globally and incidence rates predicted to increase to 27.5 million new cases per year by 2040 [31]. Radiotherapy (RT) is one of the most effective cancer treatments, particularly for solid tumours including head-and-neck tumours and glioblastoma, and is used in 50% of all cancer patients [5]. Conventional radiotherapy uses X-rays to deliver dose to the tumour, causing damage that can eventually lead to the death of cancerous cells. The dose delivered using X-rays falls exponentially with depth; this characteristic implies a fundamental limit on the maximum dose that can be delivered to the tumour without delivering an unacceptably large dose to healthy tissue. Tumours that lie deep within the patient will receive a dose significantly lower than that delivered to the healthy tissues through which the beam passes on its way to the treatment site. X-rays that pass through the tumour will also deliver a dose to the tissues that lie behind. Dose delivered to healthy tissues can cause the death of the healthy cells and create adverse side effects. Modern X-ray facilities mitigate these effects by using a number of different treatment fields, i.e. delivering beams from several different directions. In practice, the maximum X-ray dose that can be delivered is limited by the presence of sensitive organs such as the brain and spinal cord. This situation is particularly acute in infants for whom dose to healthy tissue, sensitive organs, and bone can lead to developmental issues and a higher probability of secondary malignancies later in life. The efficacy of X-ray radiotherapy is also impacted by biological factors such as the tumour microenvironment, the oxygen level (hypoxia) present in the tissue, and the inherent radioresistance of certain types of tumour.

Radiotherapy delivered using protons and ions, particle-beam therapy (PBT), has the potential to overcome the fundamental limitation of X-ray therapy in cancer treatment [32]. The physics of the interaction between ionising radiation and tissue determines the radiobiological effect. Energy loss through ionisation is the dominant mechanism at the beam energies relevant to proton- or ion-beam therapy. The energy lost per unit distance travelled (the linear energy transfer, LET) increases as the proton or ion slows down. At low velocity the rate of increase in LET is extremely rapid. This generates a ‘Bragg’ peak in the energy deposited at the maximum range of the beam just as the protons or ions come to rest. In contrast to photons, this characteristic allows the dose delivered to healthy tissue behind the Bragg peak to be reduced to zero for protons, and almost to zero for carbon ions. The effect of scanning the Bragg peak over the tumour volume is to increase the dose to the tumour while, in comparison to X-ray therapy, sparing tissues in front of the tumour. By choosing carefully the treatment fields, dose to sensitive organs can be reduced significantly compared to an equivalent treatment with photons, thus improving patient outcomes.

The Particle Therapy Co-Operative Group (PTCOG) lists 90 proton therapy facilities and 12 carbon ion therapy facilities, based on data published in February 2020 [6]. Figure 3 shows that these facilities are located predominantly in high-income countries. Low- and middle-income countries (LMIC) are relatively poorly served, indeed nearly 70% of cancer patients globally do not have access to RT [5]. It is estimated that 26.9 million life-years could be saved in LMIC if global access could be improved [4]. Novel techniques incorporated in facilities that are at once robust, automated, efficient, and cost-effective are required to deliver the required scale-up in provision. This presents both a challenge and an opportunity; developing the necessary techniques and scaling up RT provision will require significant investment but will also create new markets, drive economic growth through new skills and technologies and deliver impact through improvements in health and well-being.

The case for a systematic study of the radiobiology of proton and ion beams

The nature of the particle-tissue interaction confers on PBT the advantage that the dose can be precisely controlled and closely conformed to the tumour volume. However, there are significant biological uncertainties in

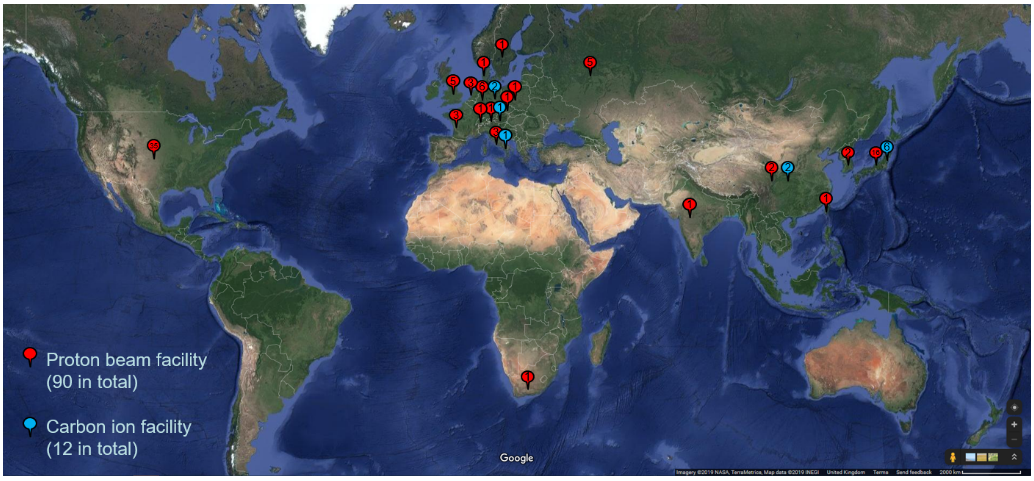

Figure 3: Location and number of proton and carbon ion therapy facilities world-wide. This figure is based on data published by PTCOG in February 2020 [6].

the impact of ionising radiation on living tissue. The efficacy of proton and ion beams is characterised by their 'relative biological effectiveness' (RBE) in comparison to reference photon beams. The treatment-planning software that is in use in the clinic today assumes an RBE value for protons of 1.1 [33]. This means that a lower dose of protons is needed to produce the same therapeutic effect that would be obtained using X-rays. However, the rapid rise in the LET at the Bragg peak leads to significant uncertainties in the RBE. It is known that RBE depends strongly on many factors, including particle energy, dose, dose rate, the degree of hypoxia, and tissue type [34], however, the radiobiology that determines these dependencies is not fully understood. A number of studies have shown that there can be significant variation in RBE [35–37]. Indeed, RBE values from 1.1 to over 3 have been derived from in-vitro clonogenic survival assay data following proton irradiation of cultured cell lines derived from different tumours [34, 38, 39]. Some of this variation may be due to the positioning of the cells during irradiation relative to the Bragg peak. RBE values of ~ 3 are accepted for high-LET carbon-ion irradiation, although higher values have been reported [40]. RBE uncertainties for carbon and other ion species are at least as large as they are for protons.

Uncertainties in RBE can lead to mis-estimation of the dose required to treat a particular tumour. Overestimation of the required dose leads to the risk of damage to healthy tissue, while an underestimate runs the risk that the tumour will not be treated sufficiently for it to be eradicated. Radiotherapy causes cell death by causing irreparable damage to the cell's DNA. Hence, differences in RBE can also affect the spectrum of DNA damage induced within tumour cells. The larger RBE values corresponding to higher LET, can cause increases in the frequency and complexity of DNA damage, particularly DNA double strand breaks (DSB) and complex DNA damage (CDD) where multiple DNA lesions are induced in close proximity [41, 42]. These DNA lesions are a major contributor to radiation-induced cell death as they represent a significant barrier to the cellular DNA repair machinery. Furthermore, the specific nature of the DNA damage induced by ions determines the principal DNA repair pathways employed to effect repair; base excision repair is employed in response to DNA-base damage and single-strand breaks, while non-homologous end-joining and homologous recombination is employed in response to DSBs [43]. Consequently, there is significant uncertainty in the precise radiobiological mechanisms that arise in PBT and a more detailed and precise understanding is required for optimal patient-treatment strategies to be devised. Detailed systematic studies of the biophysical effects of the interaction of protons and ions, under different physical conditions, with different tissue types would provide important information on RBE variation and could enable enhanced treatment-planning algorithms to be devised. In addition,

Table 1: Summary of expected dose per pulse and dose rates that LhARA can deliver. These estimates are based on Monte Carlo simulations using a bunch width of 2 ns for the instantaneous dose rate and the average dose rate is based on the 10 Hz repetition rate of the laser source.

	12 MeV Protons	15 MeV Protons	127 MeV Protons	33.4 MeV/u Carbon
Dose per pulse	5.16 Gy	2.19 Gy	0.58 Gy	5.24 Gy
Instantaneous dose rate	2.6×10^9 Gy/s	1.09×10^9 Gy/s	2.9×10^8 Gy/s	2.62×10^9 Gy/s
Average dose rate	51.6 Gy/s	21.9 Gy/s	5.8 Gy/s	52.4 Gy/s

studies examining the impact of combination therapies with PBT (e.g. targeting the DNA damage response, but also the tumour microenvironment) are currently sparse, and performing these is vital in devising future personalised patient therapy strategies using PBT. Such studies are needed, especially in the case of ion-beam radiotherapy.

The case for novel beams for radiobiology

PBT delivery to date has been restricted to a small number of beam characteristics. In a typical treatment regimen the therapeutic dose would be provided in a series of daily sessions delivered over a period of several weeks. Each session would consist of the delivery of a single fraction of $\sim$ 2 Gy delivered at a rate of $\lesssim$ 5 Gy/minute. The dose in each fraction would be distributed uniformly over an area of several square centimetres. Exciting evidence of therapeutic benefit has recently been reported when dose is delivered at ultra-high dose-rate, $\gtrsim$ 40 Gy/s (“FLASH” RT) [7, 8]. These studies indicate significantly reduced lung fibrosis in mice and skin toxicity in mini-pigs, and reduced side-effects in cats with nasal squamous cell carcinoma. Varian [44] has indicated that dose rates greater than 40 Gy/s are useful for FLASH irradiation, while IBA have indicated that the FLASH phenomenon is observed at dose rates above 33 Gy/s. In addition, therapeutic benefit has been demonstrated in the use of multiple micro-beams with diameter less than 1 mm distributed over a grid with inter-beam spacing of $\sim$ 3 mm [9]. However, there is still significant uncertainty of the thresholds and the radiobiological mechanisms by which therapeutic benefit is generated in FLASH and micro-beam therapy, which require further extensive study both in vitro and in appropriate in-vivo models.

The LhARA consortium has conceived LhARA, the Laser-hybrid Accelerator for Radiobiological Applications, as the highly flexible source that is required to elucidate the mechanisms that underlie the FLASH and micro-beam effects and to explore the vast “terra incognita” of the mechanisms by which the biological response to ionising radiation is modulated by the physical characteristics of the beam [10]. The simulations of LhARA that are described in this document have been used to estimate the dose delivered as a function of energy for protons and carbon ions. Details of the simulations can be found in sections 2.4 and 2.5. A summary of the results is given in table 1. The simulations show instantaneous particle rates on the order of 10^9 particles per shot can be achieved, corresponding to average dose rates up to 50 Gy/s. These estimates are based on the the baseline specifications for LhARA.

Laser-hybrid beams for radiobiology and clinical application

High-power lasers have been proposed as an alternative to conventional proton and carbon-ion facilities for radiotherapy [45–47]. The capability of laser-driven ion beams to generate protons and high-LET carbon ions at FLASH dose rates is a significant step forward for the provision of local tumour control whilst sparing normal tissue. High-power lasers have also been proposed to serve as the basis of electron, proton and ion-beams for radiobiology [48–53]. More recent projects (e.g. A-SAIL [54], ELI [55] and SCAPA [56]) will also investigate radiobiological effects using laser-driven ion beams. These studies will also address various technological issues [57–61].

The LhARA collaboration's concept is to exploit a laser to drive the creation of a large flux of protons or light ions which are captured and formed into a beam by strong-focusing plasma lenses. The laser-driven source allows protons and ions to be captured at energies significantly above those that pertain in conventional facilities, thus evading the current space-charge limit on the instantaneous dose rate that can be delivered. Rapid acceleration will be performed using a fixed-field alternating gradient accelerator (FFA) thereby preserving the unique flexibility in the time and spatial structure of the beam afforded by the laser-driven source.

Modern lasers are capable of delivering a Joule of energy in pulses that are 10s of femptoseconds in length at repetition rates of $\gtrsim 10$ Hz. At source, a laser-driven electron beam is reproducibly well collimated and has a modest ($\sim 5\%$) energy spread. By contrast, laser-driven proton and ion sources create beams that are highly divergent, have a large energy spread, and an intensity that varies by up to 40% pulse-to-pulse. Multiple ion species, from proton to carbon, can be produced from a single laser by varying the target foil and particle-capture optics. The realisation of LHARA requires that each of these issues be addressed.

The LhARA consortium's vision is that LhARA will prove the principal of the novel technologies required for the development of future therapy facilities. The legacy of the LhARA programme will therefore be: a unique facility dedicated to the development of a deep understanding of the radiobiology of proton and ion beams; and the demonstration in operation of technologies that will allow particle beam therapy to be delivered in completely new regimes.

2 LhARA facility

2.1 Overview

The LhARA facility, shown schematically in figure 4, has been designed to serve two end stations for in-vitro radiobiology and one end station for in-vivo studies. Proton beams with energies of between 12 MeV and 15 MeV will be delivered directly from the laser-driven source to the low-energy in-vitro end station via a transfer line. The high-energy in-vitro end station and the in-vivo end station will be served by proton beams with energy between 15 MeV and 125 MeV and by ion beams (including C^{6+}) with energies up to 33.4 MeV/u. This configuration makes it natural to propose that LhARA be constructed in two stages; Stage 1 providing beam to the low-energy in-vivo end station and Stage 2 delivering the full functionality of the facility. The development of LhARA Stage 1 will include machine performance and optimisation studies designed to allow in-vitro experiments to begin as soon as possible.

The principal components of the LhARA facility are:

- *Laser-driven proton and ion source*: protons and light ions will be generated using target normal sheath acceleration from a thin foil exposed to a laser that delivers 2.5 J in 25 fs pulses at 10 Hz.
- *Proton and ion capture section*: Two strong focusing electron-plasma (Gabor) lenses will be used to capture the divergent flux of particles arising from the laser target.
- *Matching and energy selection section*: Three Gabor lenses, two RF cavities, and two octopole magnets will be used to transport and match the beam into transfer lines that will take it either to the low-energy in-vitro end station or to the injection line of the FFA. The matching section will include a collimator for energy selection and bunching cavities to allow the time structure of the beam to be preserved.
- *Beam delivery to low-energy in-vitro end station*: A 90° vertical bend will take the low-energy beam from transfer line to the low-energy in-vitro end station. The presence of dispersion in the arc allows momentum selection through the use of an additional collimation system. The beam parameters at the end of the arc have been chosen to allow the installation of further focusing or spot-scanning magnets between the end of the arc and the in-vitro end station.

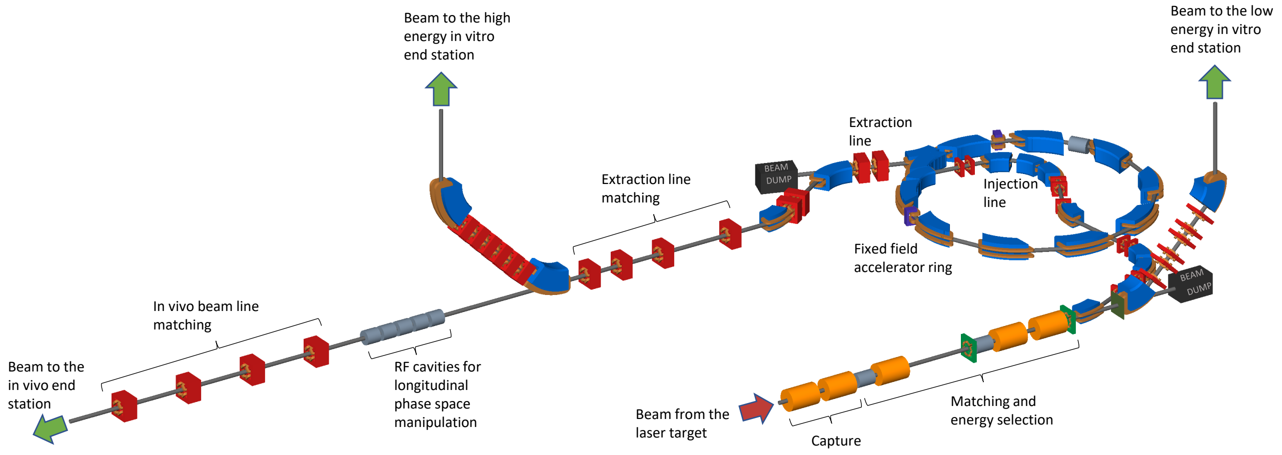

Figure 4: Schematic diagram of the LhARA beam lines. The particle flux from the laser-driven source is shown by the red arrow. The 'Capture' section is followed by the 'Matching and energy selection' section. The beam is then directed either into the 90° bend that takes it to the low-energy in-vitro end station, towards the FFA injection line, or to the low-energy beam dump. Post acceleration is performed using the 'Fixed field accelerator ring' on extraction from which the beam is directed either to the high-energy in-vitro end station, the in-vivo end station, or the high-energy beam dump.

- *Low energy abort line*: A transfer line through which the beam may be dumped safely during commissioning or in fault conditions leads to a passive beam dump.
- *Injection line for the FFA*: The beam is transported and matched to the injection section of the FFA post accelerator using a series of dipole and quadrupole magnets.
- *Fixed field alternating gradient accelerator*: A three-fold increase in beam momentum is provided using an FFA.
- *Extraction line*: The extraction line from the FFA is composed of dipole and quadrupole magnets. It includes a series of four quadrupoles to match the beam into either the in-vitro end station or the in-vivo beam line.
- *High energy abort line*: A transfer line through which the beam may be dumped safely during commissioning of in fault conditions leads to a passive beam dump.
- *Beam delivery to high-energy in-vitro end station*: A 90° vertical bend by which bean is delivered to the high-energy in-vitro end station. Again the beam parameters at the end of the arc have been designed to allow the subsequent installation of further focusing or spot-scanning magnets.
- *Transfer line to the in-vivo end station*: The transfer line that delivers beam to the in-vivo end station includes a series of quadrupole magnets to match the beam into the end station and five RF cavities for longitudinal phase-space manipulation. The installation of spot-scanning magnets between the end of the final focus section and the in-vivo end station is envisaged.

The design parameters for the various components of LhARA are given in tables 2 and 3. The design of the LhARA facility is described in the sections that follow.

2.2 Laser-driven proton and ion source

Laser-driven ions have been posited as a source for radiobiology studies for a number of years [62–64]. Until recently, however, the energies, energy spreads, and the shot-to-short reproducibility were such that laser-driven

Table 2: Design parameters of the components of the LhARA facility. The parameter table is provided in a number of sections. This section contains parameters for the laser-driven proton and ion source, the proton and ion capture section, and the Stage 1 beam transport section.

Parameter	**Value or range**	**Unit**
Laser driven proton and ion source		
Laser power	100	TW
Laser Energy	2.5	J
Laser pulse length	25	fs
Laser rep. rate	10	Hz
Proton energy	15	MeV
Proton and ion capture		
Beam divergence to be captured	50	mrad
Gabor lens effective length	0.857	m
Gabor lens length (end-flange to end-flange)	1.157	m
Gabor lens cathode radius	0.0365	m
Gabor lens maximum voltage	65	kV
Number of Gabor lenses	2	
Alternative technology: solenoid length	1.157	m
Alternative technology: solenoid max field strength	1.3	T
Stage 1 beam transport: matching & energy selection, beam delivery to low energy end station		
Number of Gabor lenses	3	
Number of re–bunching cavities	2	
Number of collimators for energy selection	1	
Arc bending angle	90	Degrees
Number of bending magnets	2	
Number of quadrupoles in the arc	6	
Alternative technology: solenoid length	1.157	m
Alternative technology: solenoid max field strength (to serve the injection line to the Stage 2)	0.8 (1.4)	T

Table 3: Design parameters of the components of the LhARA facility. The parameter table is provided in a number of sections. This section contains parameters for the Stage 2 beam transport and the in-vitro and in-vivo end stations.

Parameter	**Value or range**	**Unit**
Stage 2 beam transport: FFA, transfer line, beam delivery to high-energy end stations		
Number of bending magnets in the injection line	7	
Number of quadrupoles in the injection line	10	
FFA: Machine type	single spiral scaling FFA	
FFA: Extraction energy	15–127	MeV
FFA: Number of cells	10	
FFA: Orbit $\mathrm{R_{min}}$	2.92	m
FFA: Orbit $\mathrm{R_{max}}$	3.48	m
FFA: External R	4	m
FFA: Number of RF cavities	2	
FFA: RF frequency	1.46–6.48	MHz
FFA: spiral angle	48.7	Degrees
FFA: Max B field	1.4	T
FFA: k	5.33	
FFA: Magnet packing factor	0.34	
FFA: Magnet gap	0.047	m
FFA: Number of kickers	2	
FFA: Number of septa	2	
Number of bending magnets in the extraction line	2	
Number of quadrupoles in the extraction line	8	
Vertical arc bending angle	90	Degrees
Number of bending magnets in the vertical arc	2	
Number of quadrupoles in the vertical arc	6	
Number of cavities for longitudinal phase space manipulation	5	
Number of quadrupoles in the in vivo beam line	4	
In vitro biological end stations		
Maximum input beam diameter	1-3	cm
Input beam energy spread	< 2	%
Input beam uniformity	< 5	%
Scintillating fibre layer thickness	0.25	mm
Air gap length	5	mm
Cell culture plate thickness	1.3	mm
Cell layer thickness	0.03	mm
Number of end stations	2	
In vivo biological end station		
Maximum input beam diameter	1-3	cm
Input beam energy spread	< 2	%
Input beam uniformity	< 5	%
Beam options	Spot-scanning, passive scattering, micro-beam	

sources were not considered suitable to serve a radiobiology laboratory. While a number of radiobiology experiments have been conducted with laser-generated ions [65–68], these have been limited in scope to single-shot configurations, either due to low laser repetition rate or due to the want of an appropriate target for operation at high repetition rate. In addition, most of these experiments have been performed on laser facilities with rapidly shifting priorities and where the time to install dedicated, automated diagnostics, and control systems has not been possible. To date, a production-ready ion beam source based on a laser is not available anywhere in the world. Therefore LhARA will be a unique, state-of-the-art system for the study of radiobiology that exploits the numerous benefits of a laser-driven ion source.

Conventional ion sources are capable of producing ions with energies of the order 50–70 keV with currents of around 100–200 μA that are limited by space-charge effects [69]. The ions are captured and then accelerated to the required energy in large, expensive systems that are often unsuited to a clinical setting. A novel solution to these problems is to exploit the compact, flexible nature of a laser-driven source and couple this to a compact novel beam line.

The laser-driven source proposed for LhARA will operate in the sheath-acceleration regime [70–72]. Target-sheath acceleration is presently the most studied and best understood regime for the excitation and acceleration of ions using a laser. An intense, short-pulse laser beam is focused onto a target. The intense electric field generated at the target ionises the front surface and accelerates atomic electrons into the target. Electrons that gain sufficient energy will traverse the target, ionising the material as they go. As the high-energy electrons exit from the rear surface of the target a region of dense negative space charge is forms which in turn creates a strong electric field; the sheath. The electric field in turn accelerates ions from the rear of the target. The sheath-acceleration scheme has been shown to produce ion energies greater than 30 MeV/u at the highest laser intensities [73], with the peak proton energy, E_p, scaling with laser intensity as, $E_p \propto I^{\frac{1}{2}}$; the laser intensities required to reach $\lesssim 15\,\mathrm{MeV}$ are much more modest and can be obtained with laser intensities that are readily achievable. The laser system required for LhARA can therefore be compact, relatively inexpensive, and is commercially available.

Key to the operation of LhARA is a target that allows the ion-flux production to be reproducible. A number of schemes have been proposed for such targets, including high-pressure gases, cryogenic-hydrogen ribbons [74–76] liquid sheets [77] and tape drives [78]. For LhARA, a tape drive is proposed. Imperial College personnel have operated aluminium- and steel-foil tape drives with thicknesses down to $5\,\mu$m and $18\,\mu$m plastic-tape targets. These target systems have the benefit of being readily and continuously replenished, allowing high-charge (up to $100\,\mathrm{pC}$ at $8.9 \pm 1\,\mathrm{MeV}$, i.e. $> 10^9$ protons per shot), high-quality proton and ion generation at repetition rates of up to $10\,\mathrm{Hz}$ or more. Careful control of the tension of the tape is crucial for the production of a reproducible flux from a tape-drive target. The tape should be stretched to properly flatten the surface, without stretching it into its plastic response. Rippling of the front surface can modify the laser absorption dramatically; uncharacterised rippling can make shot-to-shot variation significant and unpredictable. Similarly, rear surface perturbations can modify the sheath field, resulting in spatial non-uniformities of the proton or ion flux or the suppression of the achievable peak energy. Tape drives with torsion control and monitoring to maintain such a high-quality tape surface have been constructed at Imperial. Work continues at Imperial to optimise further the design of such targets. The work centres on improving the reproducibility and flatness of the targets. In addition, new, thinner, tapes for improved ion generation and the generation of additional ion species are being developed. This active area of R&D will continue with the development of LhARA.

The scheme proposed for LhARA is unique when compared with previous attempts to exploit laser-driven ion sources for radiobiological applications since most experiments have been performed in single-shot configurations with high latency diagnostics. Other applications have used low repetition rates, usually due to the lack of an appropriate high rep-rate target. Further, to date most experiments have been performed either on low repetition rate laser systems or on laser facilities for which the rapidly shifting priorities leaves little time to install dedicated automated diagnostics and control systems. LhARA therefore offers a number of opportunities to push the frontiers in the field of laser-driven ion acceleration, in sustained high-frequency ion generation, advanced targetry solutions, and active, high repetition rate diagnostics. The successful development and execution of such methodologies would provide a leap forward in capability and open up exciting new fields to which the the laser-driven technique can be applied including medical isotope production and materials processing in addition to radiobiology. The target and diagnostic solutions which will be developed through the LhARA project will provide a step change in the scientific and technological application of laser-driven ion beams.

2.2.1 Technical challenges and R&D programme

A commercial laser system will be used to drive the ion production. However, the operation of a laser-driven proton and ion source at high repetition-rate is a relatively new area of research [78–82]. While such operating schemes pose a number of engineering challenges, they also offer the opportunity for enhanced acceleration. Such schemes have proved remarkably successful in producing enhanced particle beams, optimised for beam charge, peak energy, energy spread and divergence etc. While much of this research has so far focused on electron-beam production and optimising X-ray yields, such methods should translate well to proton and ion acceleration. These techniques will require an appropriate R&D effort, which we envisage shall be possible using existing capabilities across the LhARA consortium. High repetition-rate ion-beam diagnostics will also need to be produced to allow the successful execution of the LhARA programme. Instrumentation will be required to measure both the energy spectrum and composition of the ion beam as well as its spatial profile. Current methods are destructive, and often suitable only for low repetition rate. LhARA will require appropriate passive non-destructive diagnostics. Such detectors have not yet been demonstrated successfully and will require to be developed during the R&D phase of the LhARA project.

While the principle of a tape-drive target has been demonstrated, there are aspects of the target system that need to be developed to ensure reliability and to allow the possibility of parallel operation of different targets to produce a variety of ion species. These developments must be coupled with the development of post-target laser diagnostics. A programme of measurement coupled with simulation of the laser-target interaction will be performed to produce more accurate estimates of the beam. These estimates will primarily be used as input for particle tracking simulations through the LhARA beam line and into the end stations.

2.3 Proton and ion capture

The use of an electron cloud as a focusing element for charged particle beams was first proposed by Gabor in 1947 [83]. Gabor noted that a cloud of electrons uniformly distributed about the axis of a cylindrical vessel would produce an ideal focusing force on a beam of positively charged particles. In the original proposal, an axial magnetic field, produced using a solenoid, was proposed to provide radial confinement while an axial electrostatic field was employed to confine the cloud in the longitudinal direction. The solenoid field causes electrons to spiral around the central axis and confines them in the radial direction. A potential well was created using a cylindrical anode and grounded electrodes at the ends of the cylindrical volume to confine the electron cloud in the longitudinal direction. Gabor chose to introduce electrons from a hot-wire emitter placed in a cusp magnetic field. In this field configuration electrons couple into the lens with high transverse velocity and would therefore be well confined.

If the motion of electrons captured in the lens under the combined electric and the magnetic fields are considered using appropriate boundary conditions the confinement conditions can be determined [84]. In the radial direction, where there is magnetic confinement and Brillouin flow, the number density of electrons, n_e, is given by:

$$n_e = \frac{\epsilon_0 B^2}{2m_e e} = 5 \times 10^{18}\, B^2\,;$$

where B is the magnetic field, e the magnitude of the charge on the electron, m_e the mass of the electron, and ϵ_0 the permittivity of free space. In the longitudinal direction, where there is electrostatic confinement, n_e is given by:

$$n_e = \frac{4\epsilon_0 V_A}{eR^2}\,;$$

where R is the radius of the cylindrical anode which is held at the positive potential V_A. The longitudinal confinement condition imposes a strict limitation on the electron density relative to the anode voltage. In theory the number density varies with the origin of the electrons—those generated within the trap are better confined than those generated in regions outside the magnetic field. In practice the number density never reaches the theoretical limit—an 'efficiency factor' is required to obtain agreement between theory and measurement. Eliminating n_e between the two expressions allows a relationship between the magnetic and electric field strengths to be derived. The theoretical number density of confined electrons in the cloud is then defined by the dimensions of the apparatus and the magnitude of the fields. In the thin lens approximation, the focal length, f, of a Gabor lens can be expressed in terms of the magnetic field and the particle velocity, v_p:

$$\frac{1}{f} = \frac{e^2 B^2}{4 m_e m_p v_p^2} l\,; \tag{1}$$

where m_p is the mass of the particles in the beam. The focal length of the Gabor lens is therefore proportional to the kinetic energy or, equivalently, the square of the momentum, of the incoming beam. By comparison, the focal length for a solenoid is proportional to the square of the momentum and that of a quadrupole is proportional to momentum. For a given focal length, the magnetic field required in the Gabor lens is reduced compared to that of a solenoid that would give equivalent focusing:

$$B_{GPL} = B_{sol} \sqrt{Z \frac{m_e}{m_{ion}}}\,; \tag{2}$$

where B_{GPL} and B_{sol} are the magnetic fields in the Gabor lens and the equivalent solenoid respectively; m_{ion} is the mass of the ions being focused, and Z is the charge state of the ions. In the case of a proton beam the reduction factor is 43. Thus, for example, where a 2 T superconducting solenoid would be required, the magnetic field required for a Gabor lens would only be 47 mT. This means the cost of a Gabor lens can be significantly lower than the cost for a solenoid of equivalent focusing strength.

The plasma-confinement system described above is commonly known as a 'Penning trap' and has found wide application in many fields [85]. Variations on the Penning trap where axial apertures in the cathodes are introduced, such as the Penning-Malmberg trap [86, 87] are attractive for beam-based applications due to the excellent access provided to the plasma column, see figure 5. The properties of these particle traps are well described in the literature and a wealth of papers are available [88–90]. One feature of these types of Penning trap is the simple harmonic motion of the trapped particles in the combined electric and magnetic fields. This allows detailed investigation of the properties of the trapped particles through their oscillation frequencies. In a lens application, oscillation of the trapped particles is not problematic provided the electron oscillations do not introduce non-uniformity into the plasma cloud which would degrade the focusing performance. The field of magnetic confinement fusion provides useful insight; the history of magnetically confined fusion is populated with the discovery and suppression of plasma instabilities and this subject remains the object of much research effort.

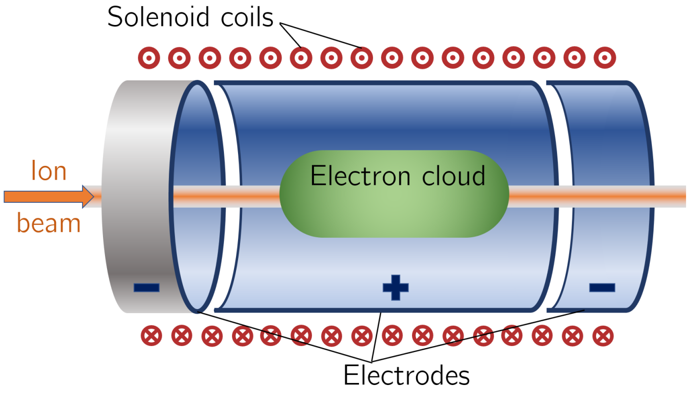

Figure 5: Schematic diagram of a Penning-Malmberg trap of the type proposed for use in the Gabor lenses to be used in LhARA. The solenoid coils, and the direction of current flow, are indicated by the red circles. The confining electrostatic potential is provided using a central cylindrical anode and two cylindrical negative end electrodes. The ion beam enters on-axis from the left and the electron cloud is indicated by the green shaded area.

As the number density of the trapped particles increases, the growth rate of instabilities increases and stability becomes more difficult to achieve. It might therefore be expected that a reduction in electron number density would provide a useful means to stabilise the plasma lens. However, the power of the focusing effect is linked to the number density and so there is a strong driver to maximise the number density. Thus, one design goal for the Gabor lens for LhARA is to maximise the available electron density.

Plasma dynamics causes instabilities in a plasma to grow at characteristic rates. It may therefore be expected that instabilities will appear after an initial stable period. As the beam source proposed for LhARA produces a very short pulse of positively charged particles, it is reasonable to propose a system that uses a transient electron cloud synchronised to the beam source. Gabor lenses can also operate at appreciable vacuum pressures, opening up the possibility of beam space-charge neutralisation, should the application require it.

The Stage 1 beam-transport system requires five electron-plasma focusing elements of approximately 1 m length. Beam simulations performed to date have used an equivalent solenoid to approximate the performance of the Gabor lens, with on-axis magnetic field strengths of 1.3 T or lower. The field in these magnets is getting close to the regime where warm magnets are possible but power-hungry and superconducting magnets may be desirable but expensive and not necessarily simple to design given the requirements to operate close to other field-sensitive components. By contrast, the coils for a Gabor lens are straight forward to design and air-cooled options may even be possible.

In the event that the LhARA requirements for the Gabor lens proves to be too challenging, an alternative technology would need to be implemented. From the optics simulations that have been done it will be relatively straight forward to exchange the Gabor lenses for solenoids. One caveat is that energy selection would then need to be done using a Wien filter [91]. The magnetic field required in the first solenoid is quite high but still achievable with normal conducting magnets. Suitable choices would need to be made to minimise power consumption and it is likely that pulsed solenoids would be the cheapest and easiest solution.

Gabor lenses have many attractive features for the LhARA project including the possibility of very strong focusing, simple construction, and low magnetic field. These attractive features come at the cost of relatively high voltage operation (> 50 kV) and possible vulnerability to instability.

2.3.1 Technical challenges and R&D programme

In the LhARA design a high-intensity positively-charged beam is produced from a point-like source with a significant divergence of more than 90°. The particles in the energy range of interest are produced with a smaller divergence of the order of a few degrees, which is still quite large. Beam capture requires strong focusing close to the target to produce a rectilinear beam. Lenses of similarly short focal length are required at other points in the beam line. The focusing required for beam capture is beyond the capabilities of Gabor lenses published to date—the design therefore uses two lenses in series for beam capture. A further three Gabor lenses of the same length are included in the design for optics matching and energy selection using a collimator.

The main technical challenges for the Gabor lens project are:

- Operation of the Gabor lens at the design parameters for LhARA and verification of its focusing characteristics. This requires, as a pre-requisite, an electrode system capable of reliable high-voltage operation as well as a vacuum system which can maintain the required vacuum in the Gabor lens.
- Instrumentation of the Gabor lens. Measurement or proxy measurement of the electron density within the lens. Measurement of beam parameters at the input and output of the Gabor lens.
- Verification of the stability of the Gabor lens.

We propose to investigate Gabor lenses in steady state operation with DC fields and pulsed operation using an electron emitter to force plasma cloud generation.

2.3.1.1 Steady state operation with DC fields

The first generation Gabor lens prototype for LhARA will be designed to operate in a steady state mode [92]. Future experimental work will focus on a Penning-Malmberg trap with conventional DC magnet coils and using a low current, high voltage DC supply. The primary aims of this study are to verify operation at the required peak operating voltage and under the vacuum conditions expected in the first Gabor lens of the LhARA beam line.

High Voltage design

Electrode configurations will be explored with both grounded-anode and grounded-cathode options with the electrodes profiled to manage local field enhancement and enable the Gabor lens to run at the desired peak operating voltage. The profiles will be studied using numerical modelling techniques and isolation will be achieved using commercial ceramic high-voltage stand-offs. Versatile DC magnets will be purchased from an industrial supplier and these robust coils will allow reconfiguration of the magnetic field profile to introduce field reversal to generate magnetic cusps if required. This will require appropriate support structures to accommodate the large forces inherent in such configurations.

Vacuum system

The vacuum vessel within which the laser target is mounted operates under relatively poor vacuum conditions (1×10^{-4} to 1×10^{-5} mBar) mainly due to vaporisation of the target and outgassing. The Gabor lens operates for preference under high-vacuum conditions ($< 1 \times 10^{-6}$ mBar [93]) and can be constructed and processed using established high-vacuum techniques from the high-power RF tube manufacturing industry to minimise the background pressure. The requirement for different vacuum conditions in two adjacent regions of the system requires either a thin window or a differential pumping system to separate the two vacuum regions. While a thin film may be convenient and simple, scattering will degrade the beam quality, therefore this option has been rejected and differential pumping is thus required. The initial design requires the target and the first Gabor lens to be separated by 10 cm to allow space for laser beam diagnostics. At this distance the beam to

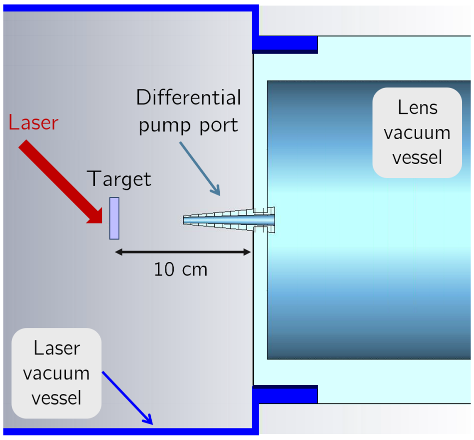

Figure 6: Schematic diagram of the interface between the laser target and the first Gabor lens. The laser vacuum vessel (dark blue) is connected to the lens vacuum vessel (light blue) with two flanges shown. The differential pump port is re-entrant into the laser vacuum volume with 5 cm closest approach to the target.

be captured by the Gabor lens will require a minimum aperture of 8 mm, based on the expected divergence of the beam. Using realistic pumping speeds for reasonably sized turbo-molecular drag pumps and designing a minimal cross-section aperture, the calculated pressure differential between the volumes is less than two orders of magnitude. This can be improved by using a re-entrant cone of length 50 mm, penetrating into the laser target vessel (figure 6), for which the predicted pressure differential can exceed three orders of magnitude. This will be sufficient to allow the Gabor lens to operate at a vacuum pressure of 1×10^{-7} mBar or lower. Increasing the re-entrant cone length will provide a greater pressure differential due to the decrease in the required entrance aperture for the beam. The detailed mechanical arrangement that allows line of sight for the laser diagnostics remains to be determined.

Pulsed operation using an electron emitter

A second generation Gabor lens will be designed and built for pulsed operation that incorporates an electron emitter to generate the plasma in the lens. At a voltage of 75 kV, the current density required to reach the desired electron number density is of the order of a few A/cm^2. This is well within the capabilities of established cathode technologies. With a lens length of 1 m, the transit time at 75 kV will be of the order of 6 ns for rectilinear trajectories, high transverse velocities will both increase the effective current density and the transit time, by as much as a factor of two. Provided the electron beam can be efficiently ‘mirrored’ at the end of the lens, trapped trajectories can be generated and the total current density, and hence effective number density may be increased. In this regard it may be wise to operate the electron emitter at a voltage slightly above that of the cathodes to ensure that no electrons are emitted with sufficient energy to reach the cathodes. With a round trip time of less than 25 ns, current pulses of the order of a few hundreds of ns will be required. This technique will saturate as the growing electron-cloud space charge suppresses electron emission at the cathode; Gabor discusses this effect in his original paper. The applied cathode voltage or the cathode current-pulse length can therefore be used to control the electron number density. Simulations will need to be performed to design the electron emitter and study the trajectories of the emitted electrons and this will be done as part of the theoretical investigation into Gabor lenses.

Theoretical study of Gabor lenses

The theoretical study of Gabor lenses will focus on two main subjects: plasma modelling to aid investigation of plasma instabilities; and electron beam production to support the investigation of pulsed operation. The results from these studies will be important to guide the design and experimental investigations of both the first and second generation Gabor lenses.

Plasma stability

Several 3D codes are available for the modelling of plasma instabilities (e.g. [94, 95]). Experience with these codes exists within a number of groups that are members of the LhARA consortium. These codes can be processor and memory intensive, requiring access to high-performance computing resources.

Lens filling using an electron emitter

CST [95] provides excellent electron-beam modelling capabilities with the opportunity to include extensive simulation diagnostics. CST has the capability to support the design of magnetic coils and to export full 3D magnetic field maps, which facilitates the inclusion of realistic magnetic field profiles in in the electron-beam models. CST will be used to design a high current, high transverse velocity electron beam coupling into the Gabor lens. As CST places considerably lower demands on computer processor and memory, simulations can be completed efficiently and rapid simulation progress achieved. This can be enhanced by enforcing suitable symmetries to reduce the simulation volume.

2.3.1.2 Diagnostics

Diagnostics for the experimental work will focus on a thorough characterisation of the lens when it is filled with plasma and when it is empty. This will require measuring the profile of a beam that passes through the lens and measuring the electron density within the lens.

Tests with an alpha source

A beam with characteristics sufficiently close to the proposed LhARA source can be produced using an alpha source. Alpha sources readily available emit alpha particles with energies near 5 MeV, significantly below the 12–15 MeV proposed for LhARA, but close enough for a viable comparison. Within the vacuum envelope of the lens, a sealed alpha source can be placed that is collimated and profiled using shaped apertures to allow determination of beam position, distribution and any angular rotation that may be induced about the axis of the Gabor lens. Alpha-particle detection will be by thin fluorescent film. It may be necessary to introduce optical filters to manage background lighting from the plasma cloud.

Electron density measurement

Experimentally, plasma lenses have been studied with electron densities up to $1 \times 10^{15}\,\mathrm{m}^{-3}$, though most have operated one to two orders of magnitude below that level [96–98]. The electron densities calculated are at the extreme lower end of those measurable by refractive index change. Any such measurement would necessarily employ the lowest possible probe frequency to provide the longest possible wavelength. Wave-guide confinement would be required due to the long interaction lengths necessary and any resultant measurement would therefore be integrated over the lens volume. Proof of principal numerical models of the required RF circuit have been constructed and calculation of the expected refractive index change for the prototype model configuration show phase shifts of the order of a degree at 3 GHz. Modern vector network analysers can detect phase differences of a fraction of a degree making this technique viable. Appropriate consideration of the mode of propagation of the probe radiation within the magnetised plasma would be required and is non-trivial, but the technique could provide an online, non-invasive measurement of the condition of the lens. As such, the measurement remains attractive despite the known limitations. Alternative techniques to measure the electron density have been demonstrated in the literature including energy spectrometry of the emitted ions, these techniques can be developed if required.

2.4 Beam transport and delivery to the low-energy in-vitro end station

The beam-transport and beam-delivery systems are required to provide beam at the low-energy in-vitro end station that is optimised for radiobiology. This requires that the dose distribution at the cell layer be uniform and that beam losses along the beamline are minimised so that the dose which can be delivered is maximised. The design must also provide space for diagnostics and the installation of RF cavities for longitudinal phase-space manipulation and for the transfer of the beam to the post accelerator in Stage 2. The ion flux created at the laser-driven source appears to diverge from a point. The transport line has therefore been designed to minimise regions in which the beam is brought to a secondary focus so as to reduce the impact of space-charge forces on the beam phase space.

The initial lattice for the transport line was developed in Beamoptics [99] and MADX [100] was used to provide an idealistic description of the machine. Both programs calculate optical functions using transfer matrices and consequently have very good agreement one with the another. To understand accurately the performance of the machine, Monte Carlo particle tracking from the laser target through to the end station has been performed. This requires space charge to be included in the particle tracking and the simulation of the interaction of the beam with the materials of the end station. The approach taken was to use two separate programs. The first is BDSIM [101], a Monte Carlo simulation program which uses the Geant4 [102], ROOT [103], and CLHEP toolkits to track particles through the 3D geometry and fields of a particle accelerator. BDSIM has the capability to record energy deposition arising from particle-matter interactions including the production of secondary particles. BDSIM is ideally suited to the simulation of beam losses and was used to quantify machine efficiency and to model accurately the beam profile and material interactions in the end station. The GPT [104] Monte Carlo software package was used to evaluate the full 3D impact of space charge through particle tracking in electromagnetic fields. The space charge routine used in GPT for all simulations was *spacecharge3Dmesh* with the Poisson solver method *MGCG* and a fixed-sized mesh of 50, 50 and 150 mesh lines in the x, y and z directions respectively. However, GPT lacks the detailed particle-matter interaction functionality that BDSIM can provide. The results obtained with both BDSIM and GPT are presented in the sections which follow so that the impact of space charge forces can be seen in the comparison.

In order to compare the tracking simulations with the beam-optics calculations, an idealised Gaussian beam was generated with a spot size of $4\,\mu$m FWHM, with an angular divergence of 50 mrad, 35 fs FWHM bunch length, and an energy spread of 1×10^{-6} MeV. The maximum estimated bunch charge is 1×10^{9} protons. This small initial spot size and the large bunch charge will result in significant space charge forces leading to emittance growth at production. However, the presence of a substantial flux of electrons produced from the laser target will have a compensating effect. To simulate this effect, the beam was first propagated using GPT for 5 cm without space charge and then for a further 5 cm with space charge. At this point the beam was at the exit of the laser-target vessel and the beam distribution was written out. Subsequent tracking of the beam through the capture section to the end station was then performed using BDSIM or GPT using the beam distribution generated using the procedure outlined above.

Figure 7 shows an overview of the Stage 1 beam transport-section as visualised in BDSIM. Standard BDSIM geometry is used for visualising all the machine components. The beam line can be considered to be composed of five sections: beam capture; matching and energy selection; beam shaping; vertical arc matching; and an abort line. The total length of this beam line is 17.255 m.

The Gabor lens assumed for LhARA has a peak cathode voltage of 65 kV, an inner radius of 3.65 cm, and a length of 1.16 m [105]. The capture section uses two such lenses to reduce the beam's transverse momentum

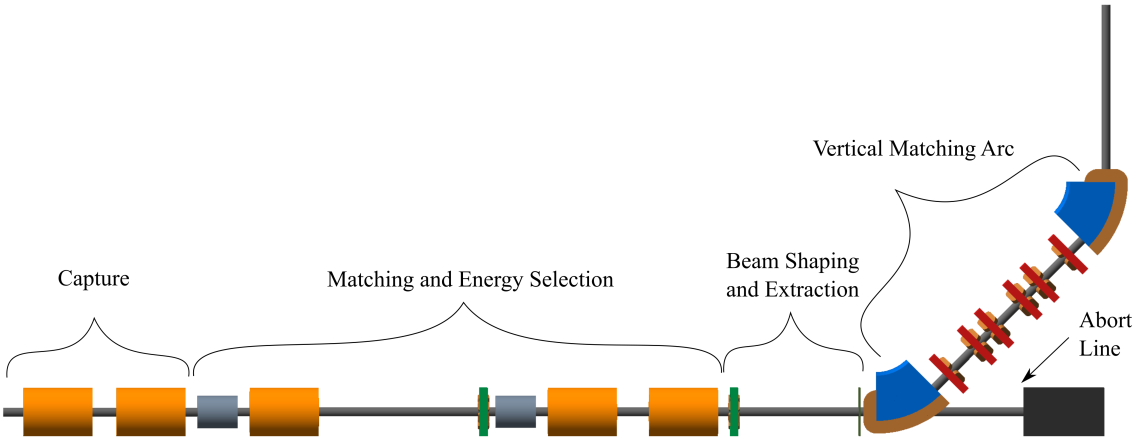

Figure 7: Beam transport for Stage 1 of LhARA visualised in BDSIM, showing 5 machine sections. The capture section is composed of two Gabor lenses (orange cylinders). The matching and energy selection section includes three Gabor lenses, two RF cavities (grey cylinders) and an octopole magnet (green disc). The beam shaping and extraction section includes a second octopole and a beam shaping collimator (black vertical bar). The vertical matching arc directs the beam into the low-energy in-vitro end station and is composed of two 45° dipoles and 6 quadrupoles.

to approximately zero. Beyond the capture section, an RF cavity permits control of the bunch length and manipulation of the longitudinal phase space. A third Gabor lens then focuses the bunch in both transverse planes to a small spot size through a 2.55 m long drift tube. This space has been allocated for collimation and diagnostics. A second RF cavity is located immediately after the focal plane to provide further longitudinal manipulation. Two further Gabor lenses bring the beam parallel once more in preparation for the vertical 90% arc. The effective length (i.e. the region where particles see the effect of the field) of all five Gabor lenses is the same, 0.857 m, and all lenses operate below the maximum cathode voltage.

A parallel beam provides significant flexibility in the beam shaping and extraction section; the length of this section can be varied to accommodate the switching dipole and other components required for shaping the beam to match the requirements of the radiobiological experiments. Delivering uniform dose distributions for both protons and ions with traditional passive scattering is non trivial given the low energy of the beam and potential shot-to-shot variations. A system to switch scattering material depending on particle species would be required to minimise beam degradation, which would introduce additional challenges of including a vertical nozzle within the end station. Therefore, it is proposed to include octupole magnets, a technique which has been been demonstrated in a number of facilities [106–108]. The third order focusing provided by the octupoles provides a perturbation to the first order focusing from the Gabor lenses, which should result in improved uniformity after sufficient transport through the beam line. Typically, octupoles would be located where the beam profile is large in one axis and small in the other to reduce aberrations and transverse coupling. As far as is known, octupoles have not been used in beam lines where focusing is achieved with solenoids or Gabor lenses alone, therefore further simulation efforts are required to ascertain their performance and optimal beam line location. A suitable position for placing an octupole was identified to be after the final Gabor lens where the beam is large, so its effect on the beam is expected to be significant. However, octupoles were not included in the GPT simulations as GPT does not have a standard component with an octupolar field. Using octupoles will produce a transverse distribution of the beam that is typically rectangular and would require collimation to match the circular geometry of typical cell culture plates that would be used in the in-vitro end station. A collimator is positioned at the start of the vertical arc to provide sufficient time for particles with large transverse momentum to move sufficiently off axis. The switching dipole to Stage 2 would be located between the second octupole and the collimator, requiring the octupole to be ramped down for Stage 2 running.

The vertical arc is a matching section consisting of two 0.8 m long identical dipoles and six 0.1 m long quadrupoles in two identical sets of three different strength magnets. All six have a vacuum aperture of 5 cm and the field gradient is constrained to ensure normal conducting magnets can be used. The parallel beam leaving the vertical arc propagates through a 2 m drift tube to penetrate the concrete shielding of the end-station floor and to bring the beam to bench height. The arc is designed as an achromat which cancels the vertical dispersion. Transparent optics are used where the phase advances in both transverse planes are a multiple of π. This choice ensures that the first order transverse map through the arc is equivalent to the identity transformation. In this design the beam properties are dictated by the settings of the Gabor lenses upstream of the arc. The presence of vertical dispersion in the arc can be exploited for momentum selection by using an additional collimation system.

The abort line consists of a drift followed by a beam dump as shown in figure 7. To abort the beam requires the first vertical dipole to ramp down, having the advantage of preventing charged-particle transportation through the magnetic fields to the end station. Sufficient space will be available beneath the vertical arc for a beam dump of the appropriate length and material to absorb a 15 MeV beam. A detailed design of the abort line and beam absorber will be done as part of the R&D programme. Alternative options using fast switching magnets will also be considered.

Simulations were run in both BDSIM and GPT, from the start of the capture section through to the end station, to verify the optical performance of the beam line. The physics model required to track particles through a plasma lens is currently not available in either BDSIM or GPT. The behaviour of the Gabor lens can be approximated by solenoid magnets using the conversion from Gabor lens anode voltage to solenoid current, see equations 5 and 10 in [84]. This has the advantage that the parameters of the equivalent solenoids are established early in the design process. The solenoid fields were constrained such that the anode voltage of the Gabor lens that was represented by the solenoid did not surpass the specified peak voltage. The length of the equivalent solenoids were set to the effective focusing length of the Gabor lens with an additional 15 cm of drift tube included before and after every solenoid to accommodate the physical length of the Gabor lens. Two zero-voltage RF cavities were included to guarantee that sufficient space for the longitudinal phase space manipulation cavities was included. Thus the effect of the RF cavities was not included in the simulations which follow and will be studied in the R&D phase.

10000 particles were simulated corresponding to a total bunch charge of 1×10^9, which is the estimated maximum flux. Thus, these simulations can be considered as the pessimistic case where space charge will have its strongest impact. Figure 8 shows a comparison of horizontal and vertical transverse beam sizes in BDSIM and GPT with space-charge effects included. Reasonable agreement is seen between BDSIM and GPT despite the simulation of space charge, with a nominal beam size at the location of the cell layer of 1.538 cm horizontally and 1.205 cm vertically. Emittance growth is observed prior to the first solenoid affecting optical performance throughout the remainder of the machine. However, the resulting beam dimensions at the end station are not significantly different from the BDSIM simulation results and it may be possible to adjust the quadrupoles in the vertical arc to compensate for this. In both BDSIM and GPT simulations, the transmission efficiency of the beam line is nearly 100%.

The presence of additional emittance growth beyond the initial few centimetres of transport was difficult to observe. Since the Gabor lens focuses in both axes, the focal point at which the energy-selection collimator is placed may be of concern if the effect of space charge has been underestimated. Quadrupolar focusing in the vertical arc also produces small beam dimensions. However, focusing is confined to one axis at a time, mitigating the potential for emittance growth due to space-charge forces. Further tuning of the Gabor lens

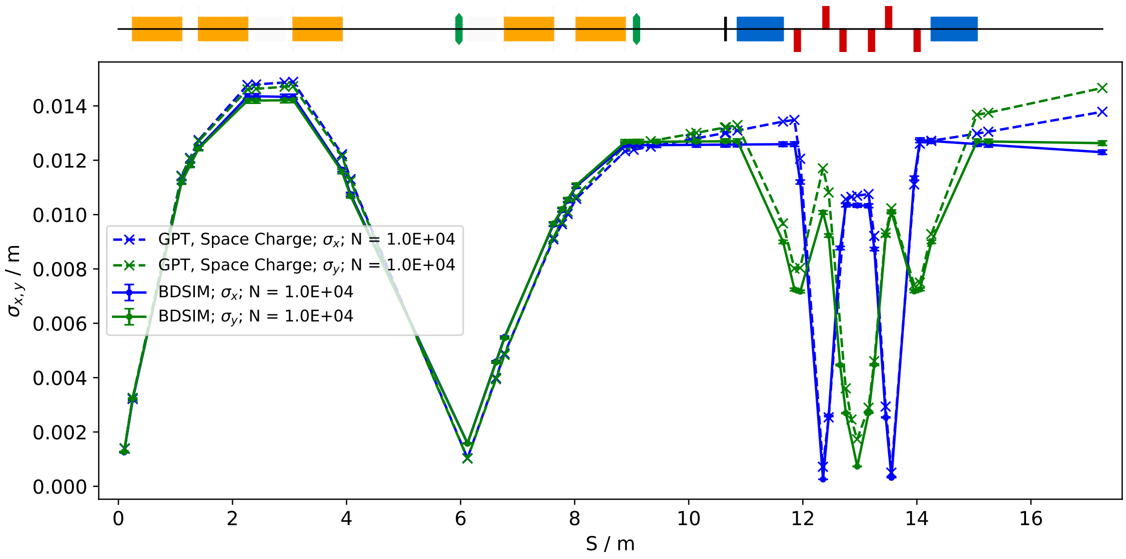

Figure 8: Horizontal (blue) and vertical (green) beam size, σ_x, and σ_y respectively, in Stage 1 simulated with (GPT, dashed lines) and without (BDSIM, solid lines) space-charge effects are shown as a function of distance from the laser target, S. The beam line elements are shown above the figure. The equivalent solenoids used to model the Gabor lenses are shown as the orange cylinders, the quadrupole, dipole, and octupole magnets are shown in blue, red, and green respectively.

voltages in the capture section may counter the non-zero transverse momentum seen entering the vertical arc, compensating the space-charge effect. The Twiss betatron functions in both transverse planes are shown in Figure 9 for both BDSIM and MADX.

The phase-space distributions at the start of the lattice, which is 10 cm downstream of the laser target, are shown in figure 10. The beam is Gaussian and has grown significantly from the original spot size. Unusually, the time distribution is slightly asymmetric, however this is not anticipated to be a concern as this is expected to grow significantly as a result of the Gaussian energy spread. The phase-space distributions at the focal plane in the energy-selection section reveal transverse aberrations arising from the solenoids, as shown in figure 11. The phase-space data was taken from the results of BDSIM simulations. These are a concern. However, the simulation of the Gabor lens using an electromagnetic field map is likely to change these aberrations, thus a field map needs to be implemented in the simulation before study of these aberrations continues. The longitudinal phase space shows that the bunch length has grown by two orders of magnitude compared to figure 10. This is due to the energy spread of the 15 MeV beam and is primarily seen as a spread in velocity.

Figure 12 shows the beam phase-space and particle distributions at the end of the Stage 1 beam transport recorded in BDSIM when not simulating the octupole fields and collimation. The transverse aberration has persisted to the end station. However, despite its more pronounced appearance, the divergence is smaller by approximately a factor of twenty. The spatial profile is Gaussian as expected. The beam phase space at the end station when octupoles and the beam shaping collimator were simulated is shown in figure 13. Both octupoles were arbitrarily set to a strength of K3=6000 with a magnetic length of 0.1 m and pole tip radius of 5 cm, which, for a 15 MeV beam, corresponds to pole tip field of 0.42 T. A 2 cm thick iron collimator was positioned 1.5 m downstream of the end of the octupole with a 40 mm diameter aperture. The transverse beam profiles in figure 13 show improved beam uniformity, indicating that the octupole and the beam shaping collimator are producing the desired effect. Further studies are needed to improve beam-profile uniformity using more realistic input beam distributions. The total beam width is 3.58 cm horizontally and 3.46 cm vertically which is

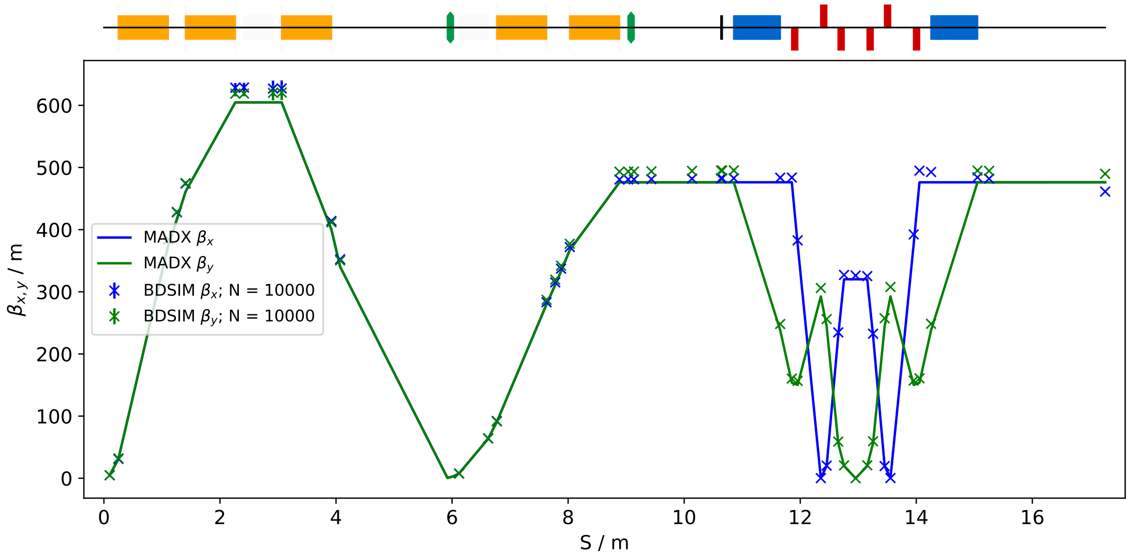

Figure 9: Horizontal and vertical Twiss beta functions in BDSIM and MADX. The beam-line elements are shown above the figure. The equivalent solenoids used to model the Gabor lenses are shown as the orange cylinders, the quadrupole, dipole, and octupole magnets are shown in blue, red, and green respectively.

sufficient to irradiate one well in a six-well cell-culture plate. The beam transmission through the collimator is estimated to be approximately 70%.

To obtain a more realistic input beam distribution, a simulation of the interaction between the laser and the laser target was performed using EPOCH [109]. The distribution of energy and angle obtained from this simulation is shown in figure 14. The peak energy has been set to 15 MeV and the angle is with respect to the laser direction. The angular distribution of the beam was shifted to centre it at -45° to make the particle distribution centred about the beam axis. The 2D results from the EPOCH simulation were then extrapolated into 3D, using the assumption that the distribution for the angle out of the simulation plane is Gaussian, and the results were filtered such that only particles between 10–15 MeV were considered. The initial treatment of the beam was the same as for the idealised Gaussian beam, i.e.: the first 5 cm was drifted without space charge and the second 5 cm was drifted with space charge. Space charge was also simulated throughout the remainder of the beam line using GPT. Figure 15 shows a significant difference compared to the idealised Gaussian beam in figure 10 in all six phase space dimensions. Notably, the population of particles at the design energy of 15 MeV is the lowest in the distribution, as expected.

At the end station, the beam displays significant emittance growth indicating that significant beam losses are observed, see figure 16. A large vertical beam size is artificially observed along the beam line as the beam line elements were set for 15 MeV optics. These losses continue to propagate in the simulation until they reach the plane where particle coordinates are written out. By selecting only those particles with a kinetic energy of 15 MeV $\pm$ 2%, the transverse particle distributions begin to show characteristics of a Gaussian beam. Poor statistics however prevents any definitive conclusions being drawn. It should be noted that the effect of the energy selection by collimation is not studied here allowing a beam with a broad energy spread to reach the end station. Therefore, implementing the energy selection collimator should improve this significantly.

The proposed design is capable of delivering beams of the desired size to the in-vitro end station. Initial studies indicate that a uniform beam can be delivered with further optimisation of the octupoles and collimator. Space charge has impacted the performance of the transport line but it is believed that this can be mitigated with minor adjustments to the Gabor lenses in the capture section. The beam focus in both planes in the energy-

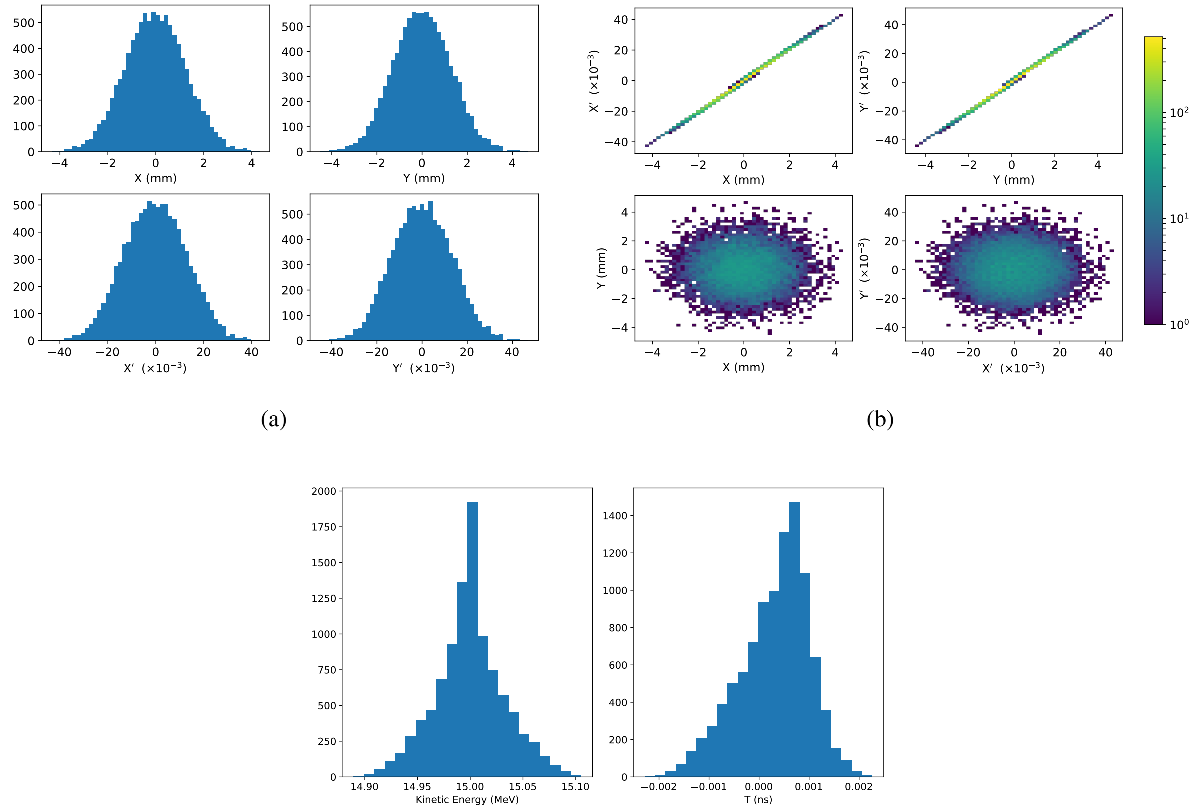

(a)

(b)

(c)

Figure 10: Beam phase space distributions in the transverse plane, (X, Y); X' and Y' give the slope relative to the Z axis. The transverse phase space is shown in figures a and b. The longitudinal phase space, kinetic energy and time, T, is shown in c. The phase-space distributions are plotted 10 cm from the laser target.

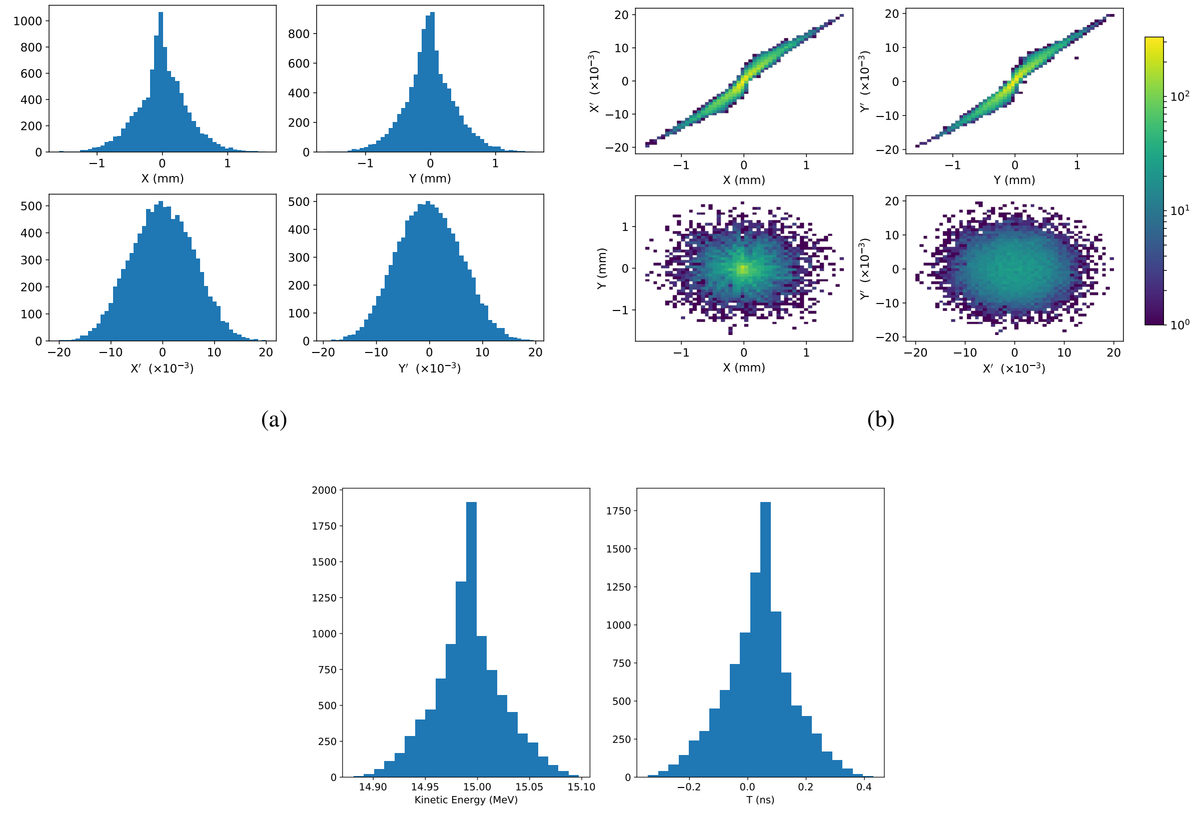

(a)

(b)

(c)

Figure 11: Beam phase space distributions in the transverse plane, (X, Y); X' and Y' give the slope relative to the Z axis. The transverse phase space is shown in figures a and b. The longitudinal phase space, kinetic energy and time, T, is shown in c. The phase-space distributions are plotted at the focus at $S = 6.02\,\mathrm{m}$.

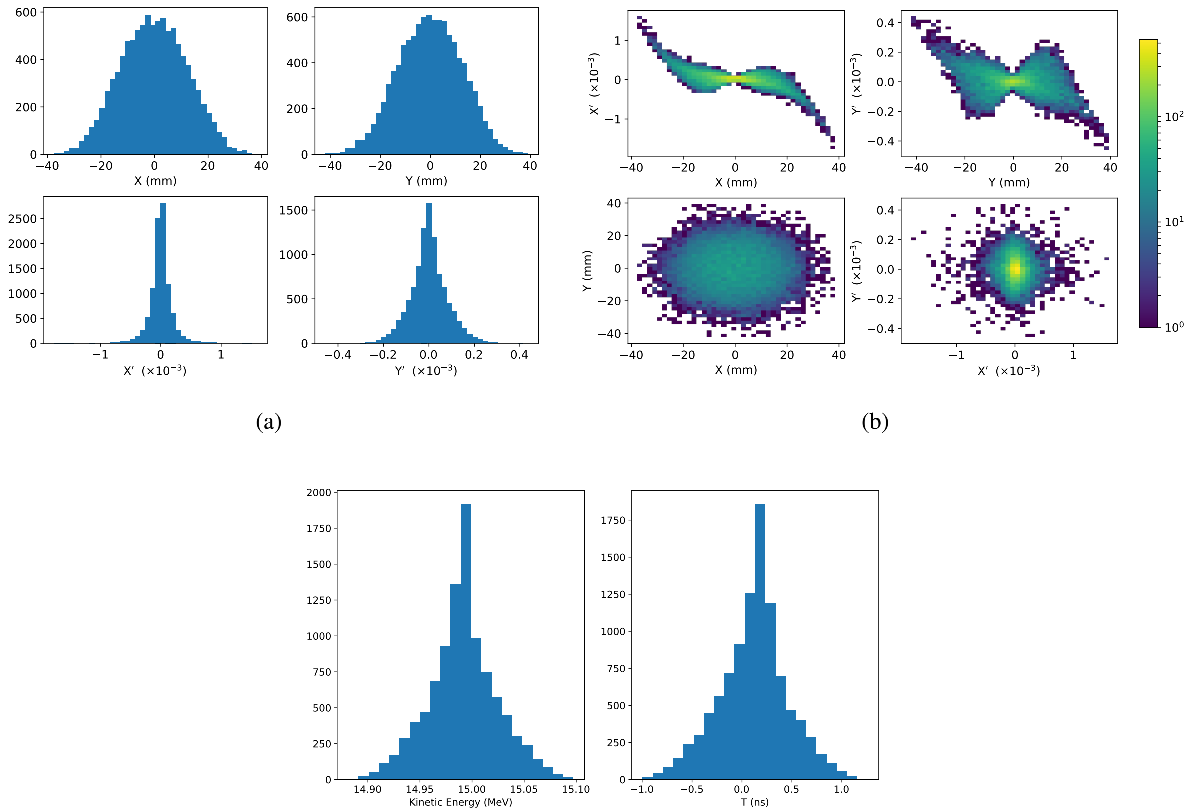

(a)

(b)

(c)

Figure 12: Beam phase space distributions in the transverse plane, (X, Y); X' and Y' give the slope relative to the Z axis. The transverse phase space is shown in figures a and b. The longitudinal phase space, kinetic energy and time, T, is shown in c. The phase-space distributions are plotted at the in-vitro end station without octupolar focusing.

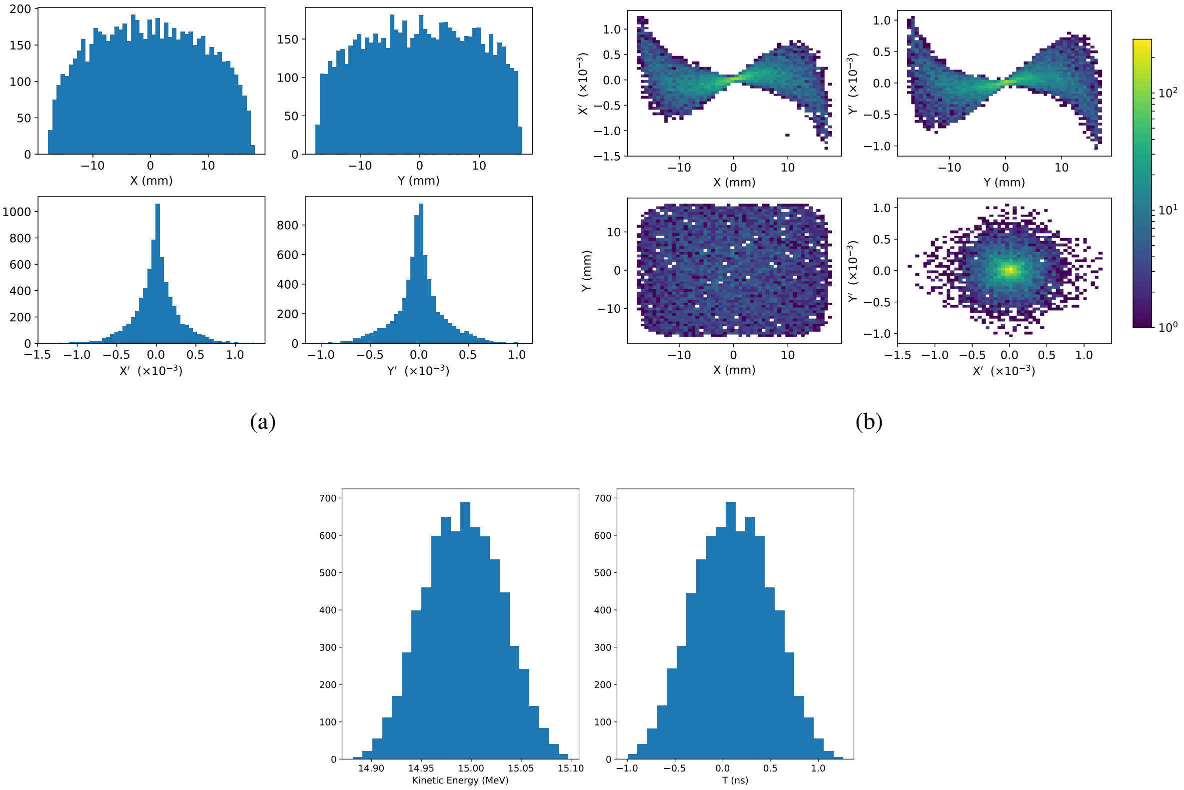

(a) (b)

(c)

Figure 13: Beam phase space distributions in the transverse plane, (X, Y); X' and Y' give the slope relative to the Z axis. The transverse phase space is shown in figures a and b. The longitudinal phase space, kinetic energy and time, T, is shown in c. The phase-space distributions are plotted at the in-vitro end station with the octupoles included.

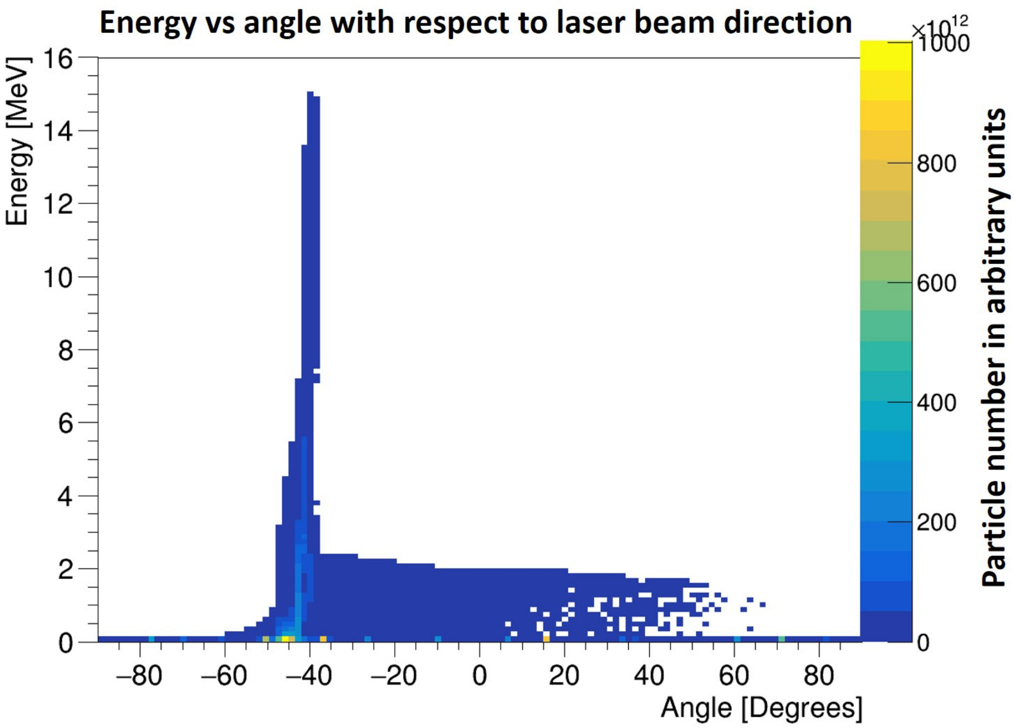

Figure 14: Distribution of energy and angle from a proton beam simulation using EPOCH showing a peak energy of 15 MeV. In this simulation 0 degrees is the direction of the laser.

selection system needs to be investigated in more detail as it may contribute to further emittance growth if space-charge effects have been underestimated by the GPT simulations.

2.4.1 Alternative design

The baseline design for the transport line described above maintains cylindrical symmetry as far as possible until the start of the vertical bend. As a result, the beam is focused in both transverse dimensions. An alternative design, in which quadrupole magnets replace the Gabor lenses in the matching and energy selection section has been developed to allow a focus to be produced in one plane at a time. This alternative design has been conceived to mitigate the effects of space charge in the event that they can not be managed in the baseline scheme. Figure 17 shows an overview of the alternative design. The fourth and fifth Gabor lenses are replaced by four quadrupoles all of length 0.1 m. The total length of this design is 15.439 m.

The beam size as a function of position along the beam line using an idealised Gaussian beam is shown in figure 18. Without space charge, simulations show that a beam size of 2.5 mm is achievable. However, the initial emittance growth due to space charge has a significant impact on the beam size. A larger beam size at the entrance to the first quadrupole results in an asymmetric bunch size, and ultimately to a divergent beam entering the end station. Despite appearing to suffer significantly from space-charge effects, it is believed that re-optimising the Gabor lenses in the capture section and the quadrupoles in the matching and energy selection section could compensate for the space-charge effects seen here and that beam parameters similar to those without space charge may be recovered. In the extraction section, beta is sufficiently low to enable injection into the FFA, as seen in figure 19. However, the design of the injection line may need to be re-optimised when the effect of space charge is included. Transmission through the alternative Stage 1 lattice is nearly 100%.

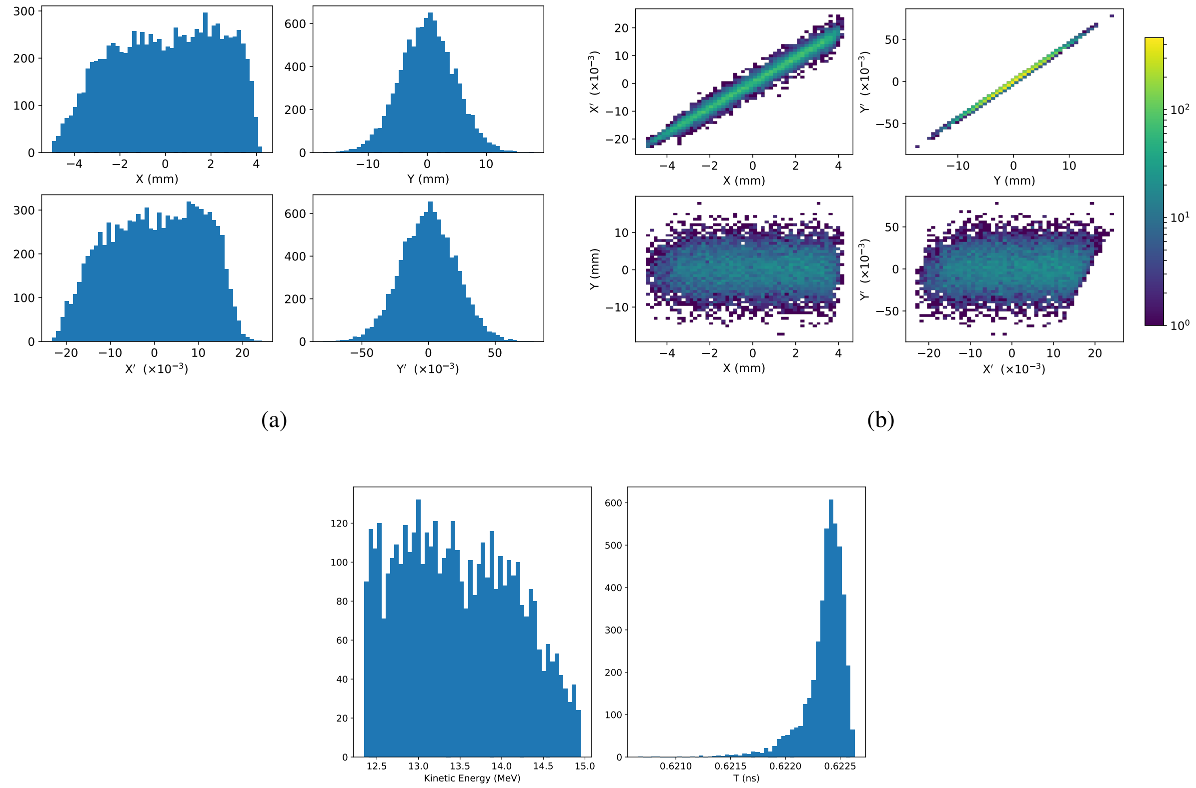

(a)

(b)

(c)

Figure 15: Phase space distributions and beam profiles for the beam derived from the EPOCH simulation 10 cm after the laser target. Distributions in the transverse plane, (X, Y); X' and Y' give the slope relative to the Z axis. The transverse phase space is shown in figures a and b. The longitudinal phase space, kinetic energy and time, T, is shown in c.

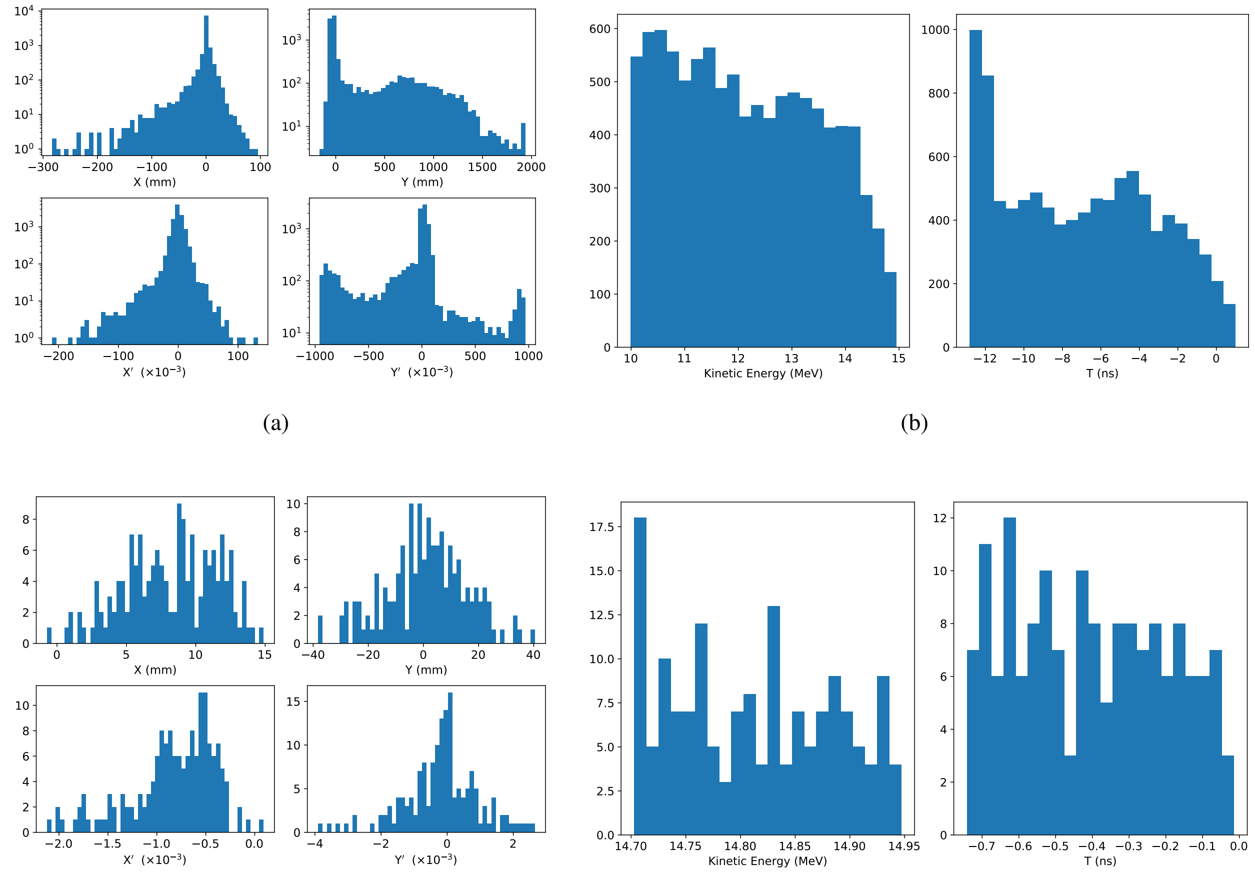

(a) (b)

(c) (d)

Figure 16: Phase-space distributions at the in-vitro end station from an EPOCH-derived beam. Particles with kinetic energies between 10 MeV and 15 MeV are shown (a & b), and for 15 MeV ± 2% (c & d). Distributions in the transverse plane, (X, Y); X' and Y' give the slope relative to the Z axis. The longitudinal phase space, kinetic energy and time, T.

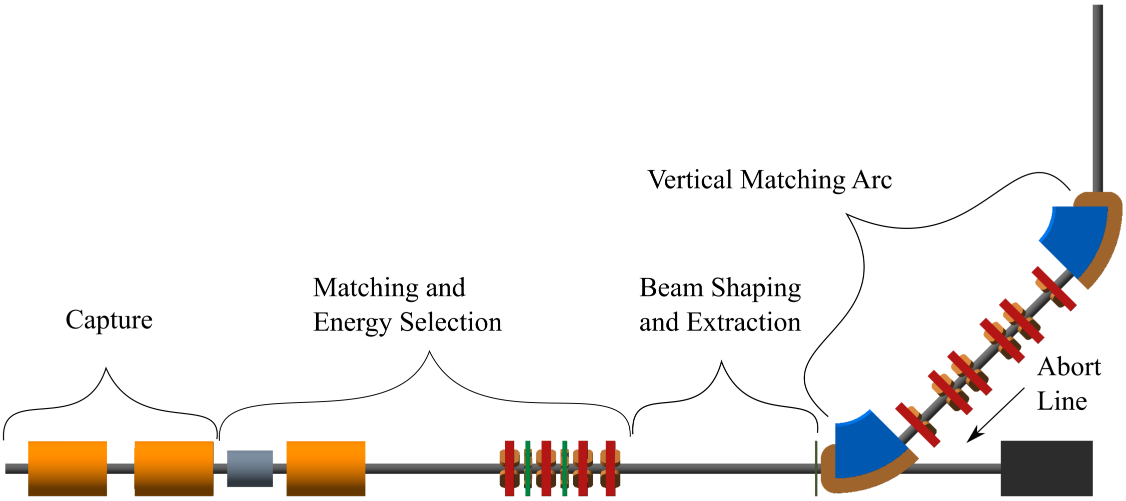

Figure 17: Beam transport for the alternative design for the Stage 1 transport lattice visualised in BDSIM. Gabor lenses are shown as orange cylinders, the RF cavities is shown as a grey cylinder, quadupole magnets are shown in red, and dipole magnets are shown in blue. The matching and energy selection section is modified to include one Gabor lens , one RF cavity, four quadrupoles, and two octupoles (green discs). The capture section, vertical matching arc, and abort line are taken over from the baseline scheme. The octupole magnet is not present in the beam shaping and extraction line.

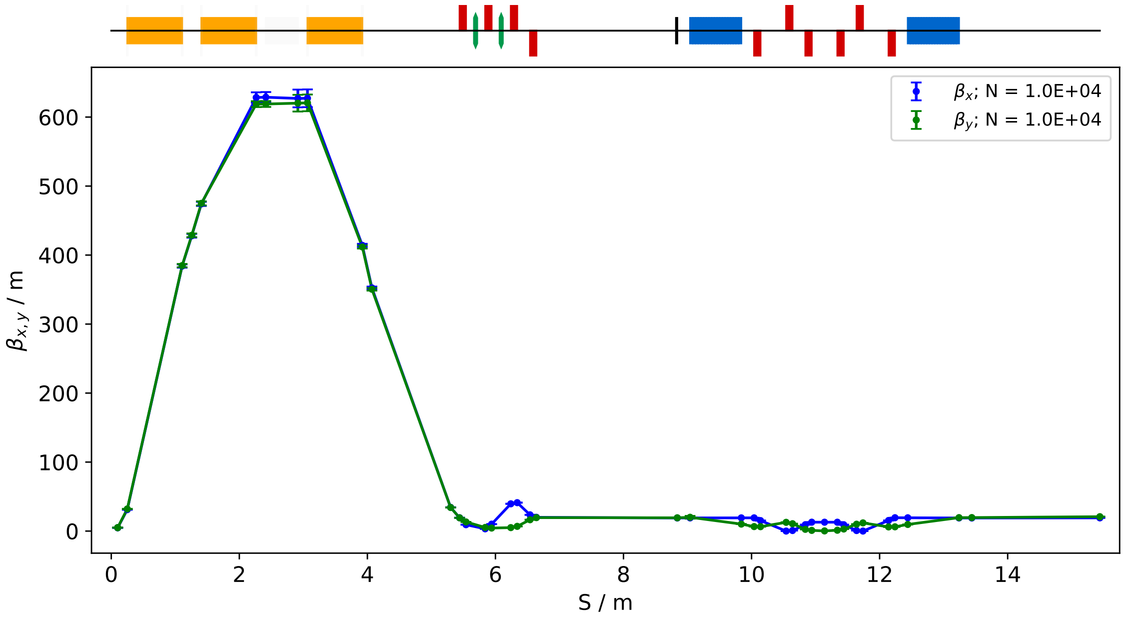

Figure 18: Horizontal and vertical betatron function, β_x (blue) and β_y (green) respectively, as a function of distance along the beam line from the laser target. The beam-line elements are shown above the figure. The equivalent solenoids used to model the Gabor lenses are shown as the orange cylinders, the qudruopole, dipole, and octopole magnets are shown in blue, red, and green respectively.

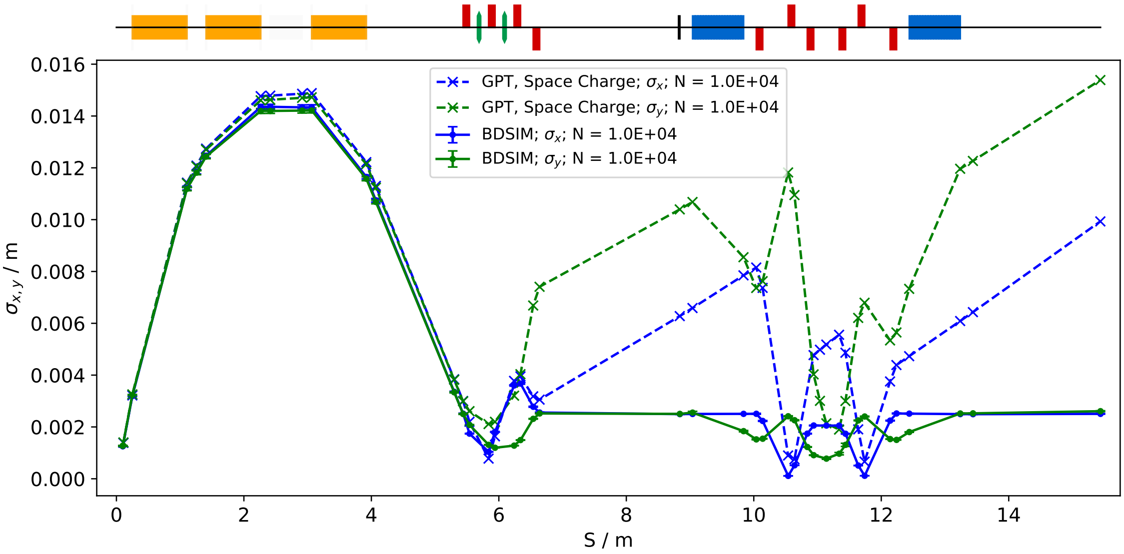

Figure 19: Horizontal and vertical beam size, σ_x (blue) and σ_y (green) respectively, in the alternative matching and energy selection section lattice simulated with (GPT, dashed lines) and without (BDSIM, solid lines) space charge effects as a function of distance from the laser target, S. The beam-line elements are shown above the figure. The equivalent solenoids used to model the Gabor lenses are shown as the orange cylinders, the quadrupole, dipole, and octupole magnets are shown in blue, red, and green respectively.

Two octupoles have been included in optimal positions within this design. The first is at S=5.665 m where the vertical beta is around an order of magnitude smaller than the horizontal beta, and the second at S=6.065 m where the reverse is true. The phase-space distributions shown in figure 20 are significantly less uniform than those produced by the baseline lattice. The final beam size is a factor three smaller; the smaller beam at the octupole locations experiences a smaller field strength. The beam derived from the EPOCH simulation was not tracked through the alternative lattice since its present optical performance using an idealised Gaussian beam shows the lattice design needs to be re-optimised.

The alternative design provides a solution that is more resilient to space-charge effects than the baseline. However, space charge again appear to have an impact on machine performance and a re-optimisation of the design is required. With an ideal beam, only the lower bound on the desired beam size is achievable. The octupoles, despite being optimally located, require further simulation to determine whether a uniform beam distribution at the end station can be achieved.

2.4.2 Simulation of the low-energy end station

BDSIM was used to investigate the energy deposition of the proton beam as it passes through the materials in the end station. The vacuum window was simulated with 0.075 mm of mylar, followed by 0.25 mm of a scintillating-fibre layer consisting of polystyrene. A 5 mm gap of air provides clearance for the automatic positioning of cell samples. Following the air gap, 1.3 mm of polystyrene represents the maximum thickness of a cell culture plate which contains a 0.03 mm thick cell layer. The cell layer is modelled using the Geant4 material “G4_SKIN_ICRP”, the composition of which is taken from the NIST database [110]. Finally, the cell layer is followed by 2.4 mm of water to represent the cell nutrients.

In figure 21 three different proton energies were simulated through the end station. The beam energy was

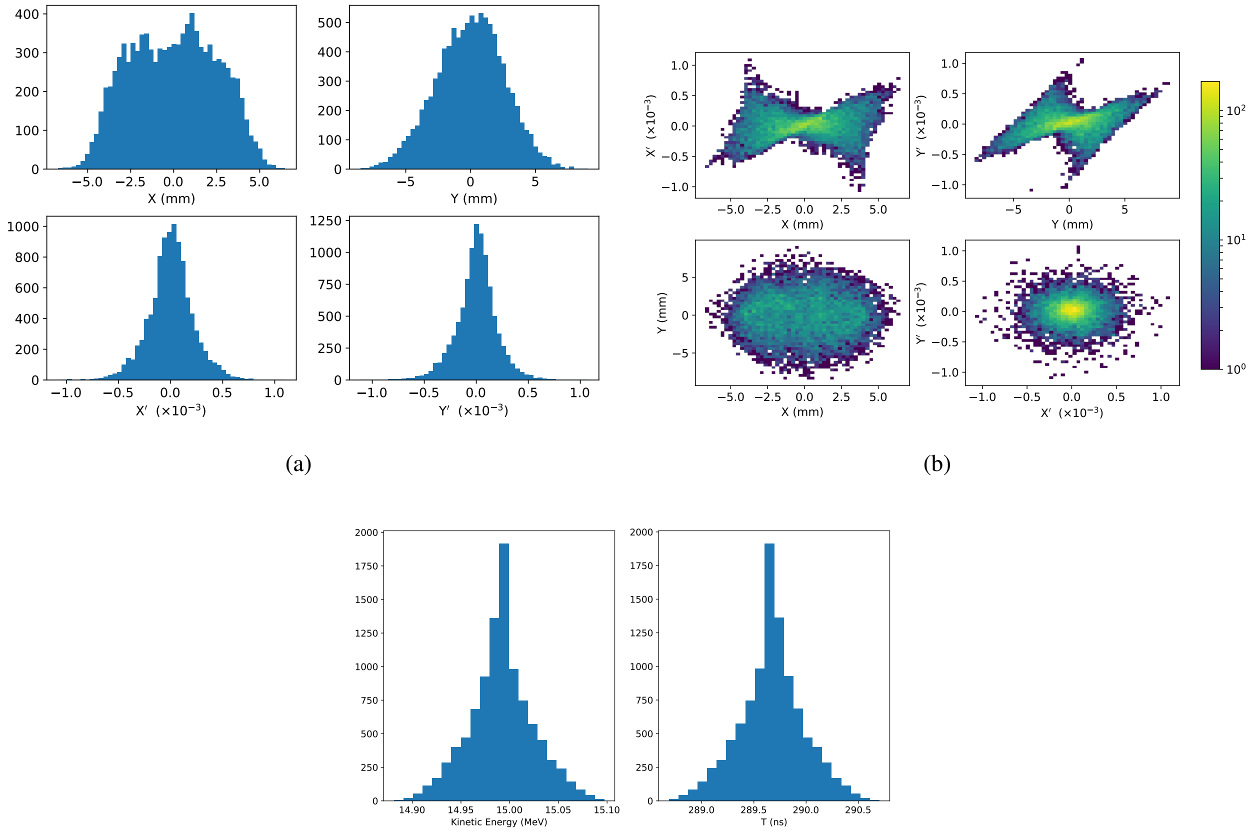

(a) (b)

(c)

Figure 20: Transverse (a & b) and longitudinal (c) phase space distributions and beam profiles in an alternate design at the in-vitro end station. Distributions in the transverse plane, (X, Y); X' and Y' give the slope relative to the Z axis. The longitudinal phase-space, kinetic energy and time, T.

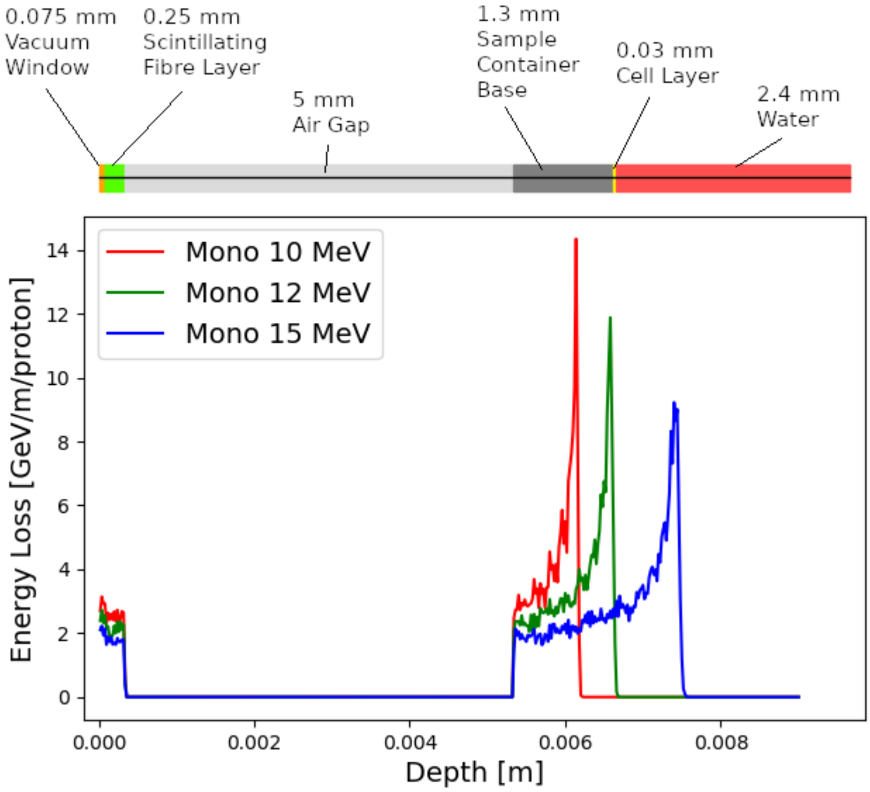

Figure 21: Energy loss as a function of depth in the low-energy in-vitro end station for three mono-energetic proton energies: 10 MeV; 12 MeV; and 15 MeV. Each beam was simulated using 10^4 particles at the start of the beam line.

Gaussian distributed with a spread small enough for it to be fully contained within the end station such that there would be no losses due to containment. The purpose of these simulations was to investigate the location of the Bragg peak relative to the expected position of the cell layer. Figure 21 shows that the beam with a kinetic energy of 10 MeV does not reach the cell layer, but the 12 MeV beam has the Bragg peak located close to the cell sample layer. The 15 MeV beam has a Bragg peak located beyond the cell layer. The ability to deliver various energies will allow the investigation of radiobiological effects for irradiations using different parts of the Bragg peak.

An idealised 15 MeV beam distribution with an energy spread of 2% was simulated. The distribution of energy deposited in the various materials through which the beam passes is shown in figure 22. The simulation results show that the mean energy of protons entering the cell samples is about 7.92 MeV with an energy spread of about 0.17 MeV. The total energy deposited within the cell layer was calculated to be 1.32 GeV (9.15×10^{-6} Gy) for 7247 particles.

To compare to the idealised 15 MeV beam, a 15 MeV beam with an energy spread of 2%, which is the maximum energy spread specified for the radiobiology studies, filtered from the beam derived from the EPOCH simulations was generated. The energy distribution of this beam is shown in figure 23 as it enters and as it leaves the cell layer. The mean energy at the entrance to the cell layer is 7.63 ± 0.20 MeV and the total energy deposited within the cell layer was $\sim$ 1.39 MeV (9.63×10^{-6} Gy) for 7247 particles. Scaling this up to the expected maximum number of protons per pulse of 10^9 gives a maximum dose per pulse of about 1.33 Gy for 15 MeV protons.

A 12 MeV beam with an energy spread of 2% filtered from the beam derived from the EPOCH simulation

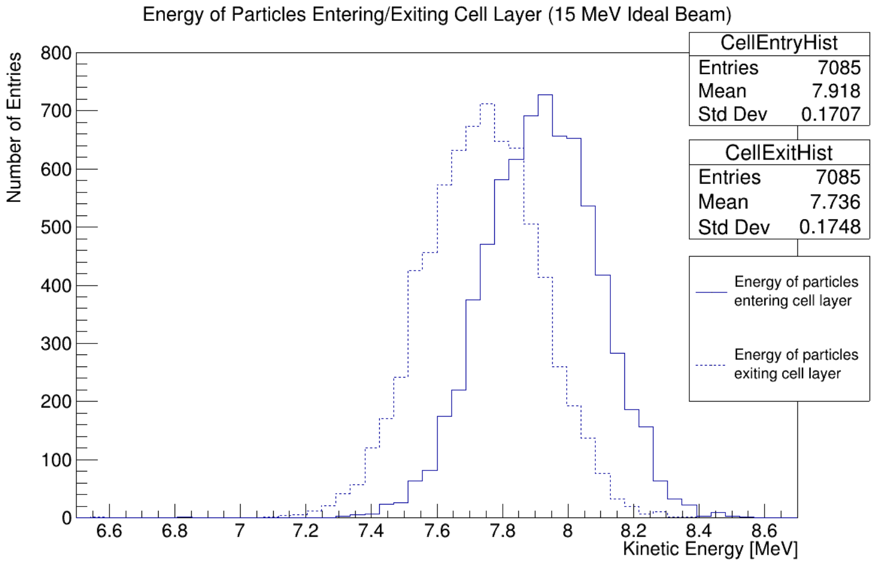

Figure 22: Simulation results of the energy distribution of particles entering and exiting the cell layer for an idealised 15 MeV beam.

was also tracked through the end station and the resulting energy distribution at the cell layer is shown in figure 24. Compared to the 15 MeV case, a very small fraction of the protons survived to exit the cell layer, which is due to the Bragg peak being located just before the cell sample with a mean energy at the entrance of the cell sample layer being approximately 0.95 ± 0.49 MeV. The total energy deposited in the cell layer was 1.39 MeV (9.63×10^{-6} Gy) for 1866 particles. Scaling this to 10^9 protons gives a maximum dose per pulse of about 5.16 Gy for 12 MeV protons.

2.4.3 Technical challenges and R&D programme

The beam transport and delivery to the low-energy in-vitro end station does not require major technological R&D beyond the development of the Gabor lens. However, there are a number of areas in which further study is required to improve the design of LhARA and to evaluate its expected performance. Some of these areas require input from experiment. For example, understanding shot-to-shot variations in the flux from the laser-driven source requires measurements of particle spectra and will be dependent on the stability of the target and, to a lesser extent, on the stability of the laser.

The accuracy of the simulation will be improved with the inclusion of the electromagnetic fields of the Gabor lens. In the R&D programme, a finite-element analysis of the Gabor lens design will be performed to produce an electromagnetic field map of the lens. The field map will also be used to investigate the efficiency of the energy selection section and for optimisation of the collimator. The simulation results presented above are based on the equivalent-solenoid model of the Gabor lens. These results demonstrate that the LhARA lattice can be implemented using solenoids should the Gabor lens R&D programme fail to deliver a lens that meets the requirements of LhARA.

As part of the facility-design effort, the use of octupoles, collimators and RF cavities will be developed and the beam-abort line will be designed. It is anticipated that the cavity performance required for LhARA is well within the present state of the art. Bunching and manipulation of the longitudinal phase space will be studied using BDSIM and GPT. The requirements for diagnostics also needs to be studied.

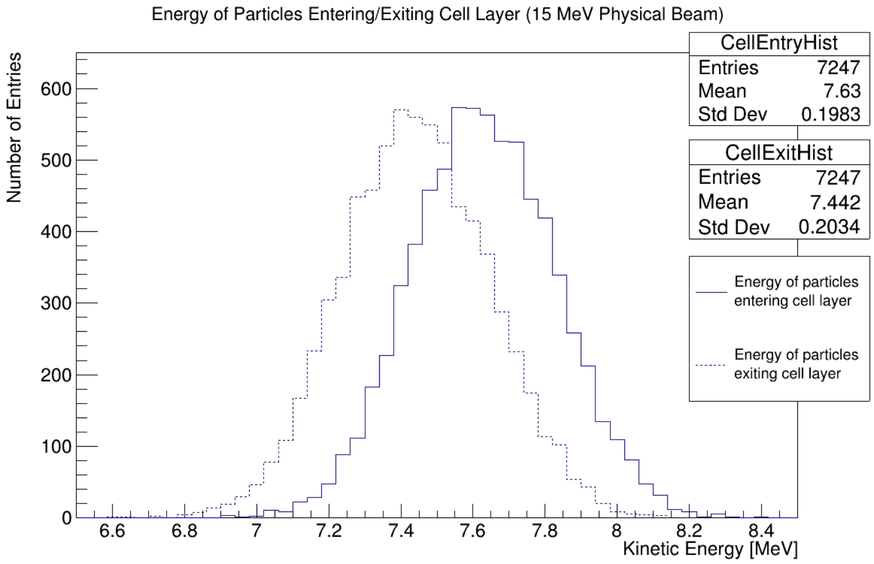

Figure 23: Simulation results of the energy distribution of particles entering and exiting the cell layer for a physical 15 MeV beam.

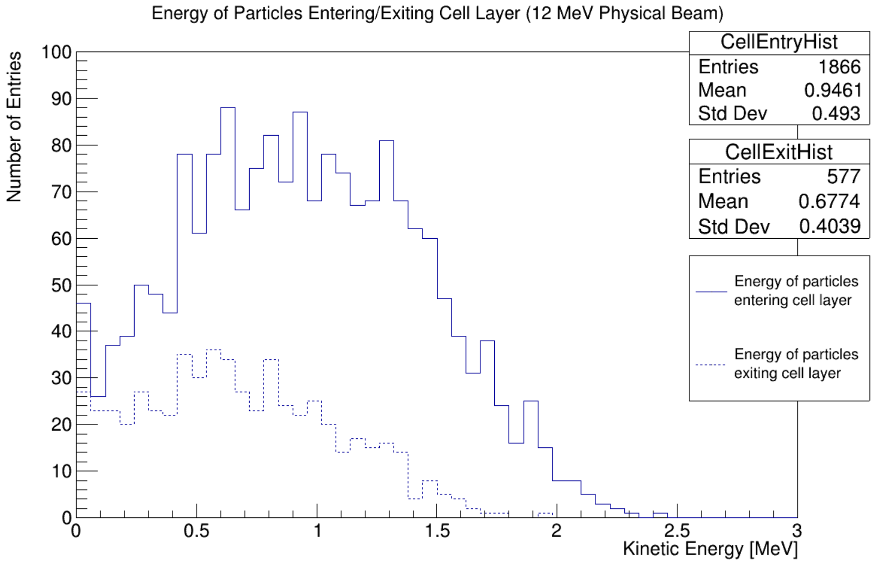

Figure 24: Simulation results of the energy distribution of particles entering and exiting the cell layer for a physical 12 MeV beam.

The proximity of the switching dipole to other magnetic elements yields the possibility of overlapping fields, particularly when ramping down to deliver beam to the low-energy end station. Although the bunch repetition rate of 10 Hz should provide enough time for the field to ramp down, this will be investigated in the design of the switching dipole. The position of the switching dipole will be optimised to ensure that it does not impact beam transport in the remainder of the beam line. Similarly, the ramp down time of the first vertical dipole will be investigated in order to safely abort the beam.

2.5 Post-acceleration and beam delivery to the in-vitro and in-vivo end stations

A Fixed field field alternating gradient accelerator (FFA), based on the spiral scaling principle [111–114], will be used for LhARA in Stage 2. This will provide post acceleration of the ion beams in order to obtain energies greater than the 15 MeV protons and 4 MeV/u (C^{6+}) ions delivered by the laser. FFAs have many advantages for both medical and radiobiological applications such as: capability to deliver high and variable dose; rapid cycling with repetition rates ranging from 10 Hz to 100 Hz or beyond; and the ability to deliver various beam energies without the use of energy degraders. In terms of size, an FFA is relatively compact due to the use of combined function magnets, which lowers the overall cost compared to conventional accelerators capable of delivering variable energy beams such as synchrotrons. Extraction can be both simple and efficient, with the possibility to use multiple extraction ports. Furthermore, FFAs can accelerate multiple ion species, which is very important for radiobiological experiments and typically very difficult to achieve with cyclotrons.

A typical FFA is able to increase the beam momentum by a factor of three, though a greater factor is achievable. For LhARA, this translates to a maximum proton-beam energy of 127 MeV from an injected beam of 15 MeV. For carbon ions (C^{6+}) with the same rigidity, a maximum energy of approximately 33.4 MeV/u can be produced.

The energy at injection into the FFA determines the beam energy at extraction. The injection energy will be changed by varying the focusing strengths in the Stage 1 beam line from the capture section through to the extraction line and the FFA ring. This will allow the appropriate energy slice from the broad energy spectrum produced at the laser-driven source to be captured and transported to the FFA. The FFA will then accelerate the beam, acting as a three-fold momentum multiplier. This scheme simplifies the injection and extraction systems since their geometry and location can be kept constant.

To provide the capability to perform cell irradiation using protons with a kinetic energy of 15–127 MeV and carbon ions, a second in-vitro end station is included in the design of LhARA. The extraction line from the FFA leads to a 90° vertical arc to send the beam to the high energy in-vitro end station. If the first dipole of the arc is not energised, beam will be sent to the in-vivo end station. The extraction line of the FFA includes a switching dipole that will send the beam to the high energy beam dump if it is not energised. The detailed design of the high energy abort line will be done as part of the facility design in the R&D programme, including radiation calculations to ensure that dumping the beam will not cause stray radiation in the end stations.

2.5.1 Injection line

In order to inject the beam into the FFA ring, the optics of the Stage 1 beam line needs to be modified to reduce the Twiss beta function propagating through the injection line. One solution consists of keeping the first two Gabor lenses in the capture section at the same focusing strength as in Stage 1 and to reduce the focusing strength of the third lens. This will change the position of the focal point used for energy selection. Therefore the position of the collimator will need to be moved downstream from its position in Stage 1 and requiring a dedicated collimation system for Stage 2. The shift in position will be relatively small and the collimator will

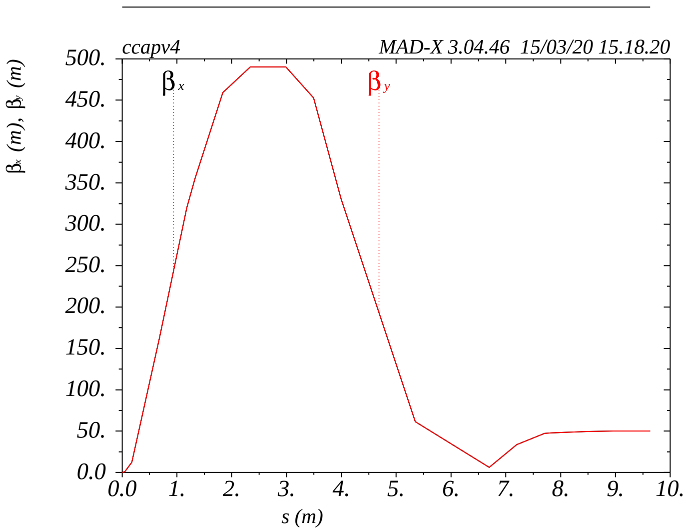

Figure 25: Twiss β_x and β_y functions for the modified Stage 1 to allow injection of the beam into the FFA. S goes from the laser target to the entrance of the switching dipole at the start of the injection line.

still be located in the drift between the third and fourth Gabor lenses. The position of the second RF cavity will also need to be changed to between the second octupole and the switching dipole. The focusing strength of the fourth Gabor lens must be increased close to its limit, while the strength of the fifth lens must to be reduced. This lattice can also be achieved using normal conducting solenoids of the same length and equivalent focusing strength, though the solenoid corresponding to the fourth Gabor lens would be close to the magnetic field saturation limit. The optics of this modified Stage 1 lattice is shown in figure 25.

The beam is diverted by a switching dipole into the injection line, which transports the beam to the injection septum magnet. In the injection line, the beam is carefully matched in both transverse planes and to the dispersion dictated by the periodic conditions in the FFA cell. As is natural for horizontal FFA machines, the beam is injected from the inside of the ring, which requires the injection line to cross one of the straight sections between the FFA magnets. Another option would be to use a vertical chicane to avoid crossing the beam pipe of the ring. This would introduce vertical dispersion that would need to be corrected and would have the additional complication that the Stage 1 beam line, the injection line, and the median plane of the FFA ring would not be in the same horizontal plane.

The in-vivo beam line of Stage 2 is aligned parallel to the capture and matching sections of Stage 1. This choice reduces the footprint of the LhARA facility but places an additional constraint on the design of the FFA. As a result the geometry of the injection line is complicated and requires the use of six bending magnets, each with the same parameters, in addition to the switching dipole and the injection septum. The injection line also requires the use of ten quadrupoles, 10 cm in length. The Twiss beta functions from the input of the switching dipole to the output of the injection septum are shown in figure 26 and the dispersion is shown in figure 27. The presence of dispersion in the injection line allows a collimator to be installed for momentum selection before injection. The collimator will be placed between the fourth and fifth ‘regular’ dipoles, where dispersion is large and the horizontal betatron function is relatively small. The layout of the injection line from the switching dipole to the injection septum together with the FFA ring, some of its subsystems and the first part of the extraction line are shown in figure 28.

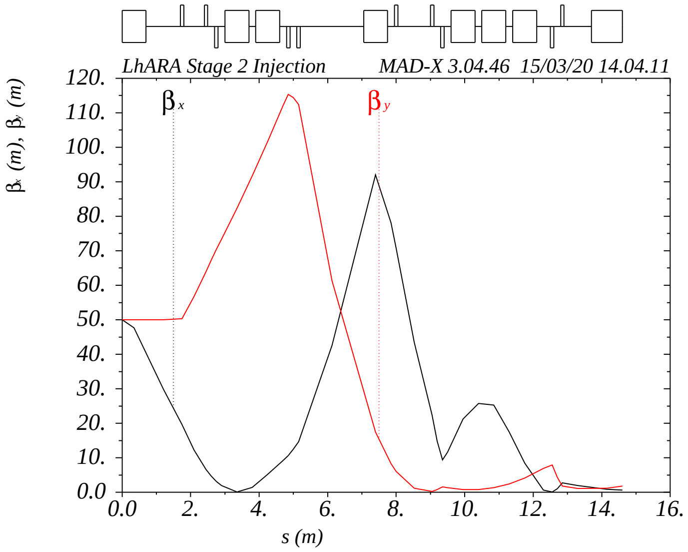

Figure 26: Twiss β_x and β_y functions in the Stage 2 injection line from the entrance of the switching dipole until the end of the injection septum.

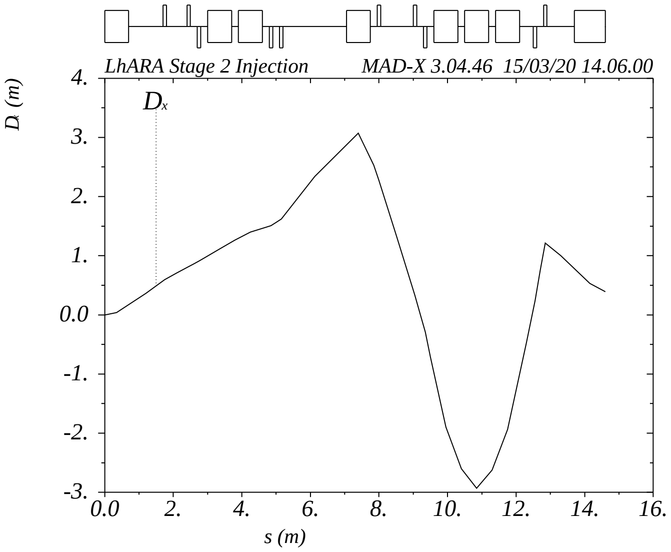

Figure 27: Dispersion function in the Stage 2 injection line from the entrance of the switching dipole until the end of the injection septum.

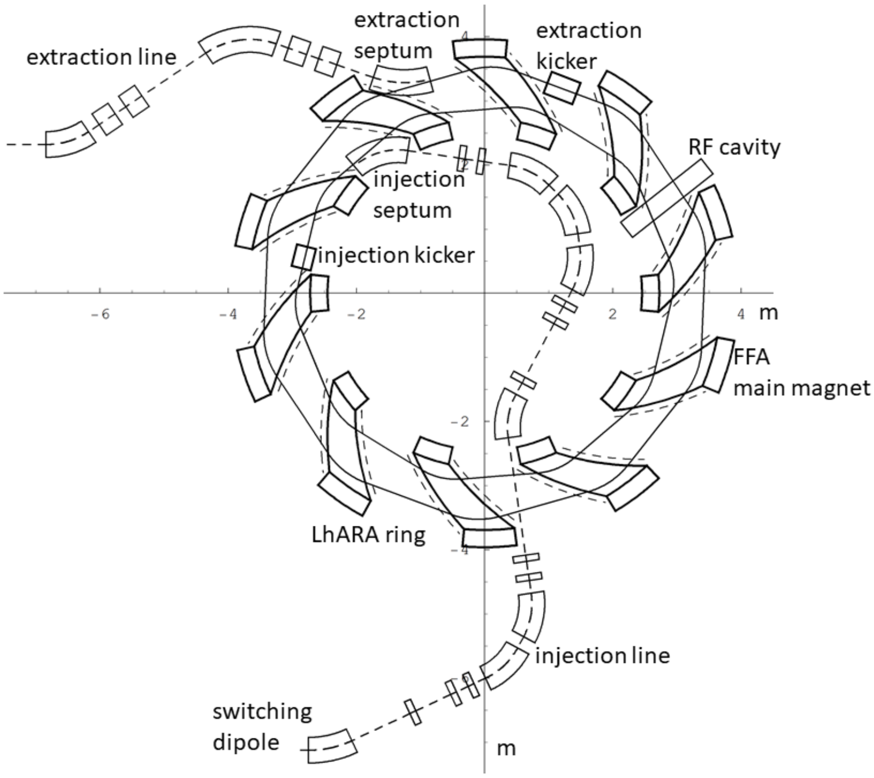

Figure 28: The layout of the injection line from the switching dipole to the injection septum together with the FFA ring, some of its subsystems and the first part of the extraction line.

As soon as the design of the FFA magnet is available and its fringe field extent is understood, all parts of the injection line and injection system located close to FFA magnets can be accurately simulated, taking field leakage into account. This will be considered as a part of the R&D programme. In addition, further optimisation of the optics will be performed and an alternative solution using a vertical chicane to inject the beam inside the FFA ring will be studied.

2.5.2 FFA ring

A scaling spiral FFA ring has been designed for post acceleration in Stage 2. The spiral scaling principle defines the field profile in the median plane using the following equation:

$$B_y = B_0 \left[\frac{R}{R_0}\right]^k F\left(\theta - \ln\left[\frac{R}{R_0}\right]\tan\zeta\right) \; ;$$

where B_0 is the magnetic field at radius R_0, k is the field index, ζ correspond to the spiral angle and F is the so called flutter function. This field law defines a zero-chromaticity condition, which means the working point of the machine is independent of energy up to field errors and alignment imperfections and avoids crossing resonances that would reduce the beam quality and may lead to beam loss. The ring consists of ten symmetric cells each containing a single combined-function spiral magnet. The choice of the cell number is a compromise between the size of the orbit excursion, which dictates the radial extent of the magnet, and the length of the straight section to allow for injection and extraction. Each of the magnets provides bending, horizontal focusing, and vertical defocusing, while the field at the magnet edges contributes to both horizontal and vertical focusing. These effects allow a stable beam to be obtained in both transverse phase spaces using only a single magnet per

Table 4: Summary of the main design parameters of the FFA ring for LhARA post-accelerator at the Stage 2.

Parameter	units	value
Number of cells		10
k		5.33
Spiral angle	degrees	48.7
R_{inj}	m	2.92
R_{ext}	m	3.48
R_{max}	m	4
B_{ext}	T	1.405
Orbit excursion	m	0.56
Straight section length at injection	m	1.2
Straight section length at extraction	m	1.43
Magnet packing factor		0.34
Magnet opening angle	degrees	12.24
Magnet gap at injection (full)	cm	4.7
Max $B\rho_{inj}$	Tm	0.562
Max $B\rho_{ext}$	Tm	1.685
Ring tunes		(2.83, 1.22)
γ_T		2.516
RF frequency	MHz	1.46-6.48
h		1,2 or 4
RF voltage	kV	8 (for 2 cavities)

cell without requiring a negative bend as is necessary for radial FFA machines, which significantly reduces the machine size. Table 4 presents a summary of the main design parameters of the FFA ring for LhARA.

The betatron functions and dispersion in one lattice cell at injection are shown in figure 29, while the working point of the machine against the main resonance lines is shown on the tune diagram presented in figure 30. Tracking studies were performed using a step-wise tracking code using Runge-Kutta integration and assuming an ideal scaling law in the median plane with fringe fields specified using Enge functions to define the magnetic field, as shown in figure 31. This tracking code [115] uses a 1 mm integration step size and off the median plane extrapolation of up to sixth order. The dynamical acceptance for 100 turns, shown in figure 32 and figure 33 for the horizontal and vertical planes respectively, are significantly larger than the beam emittance even using the most pessimistic assumption. These results confirm that a good machine working point has been chosen.

A full aperture, fast injection of the beam will be performed using a magnetic septum, installed on internal side of the ring, followed by a kicker magnet situated in a consecutive lattice cell, as shown in figure 28. The specifications of the injection system are dictated by the parameters of the beam at injection, which are summarised for the nominal proton beam in table 5. The beam at injection has a relatively small emittance and short bunch length, which limits the intensity accepted by the ring due to the space-charge effect. If the beam emittance before injection is larger by a factor of 1.7 with respect to the nominal value, then an intensity of about 10^9 protons would be accepted by the ring at the space charge limit. Fast extraction of the beam over the full aperture will be performed using a kicker magnet followed by a magnetic septum installed in a consecutive lattice cell close to the extraction orbit. This will bend the beam outside of the ring as shown in figure 28. Table 6 summarises the selected parameters of the injection and extraction elements.

Acceleration of the beam to 127 MeV will be done using an RF system operating at a harmonic number

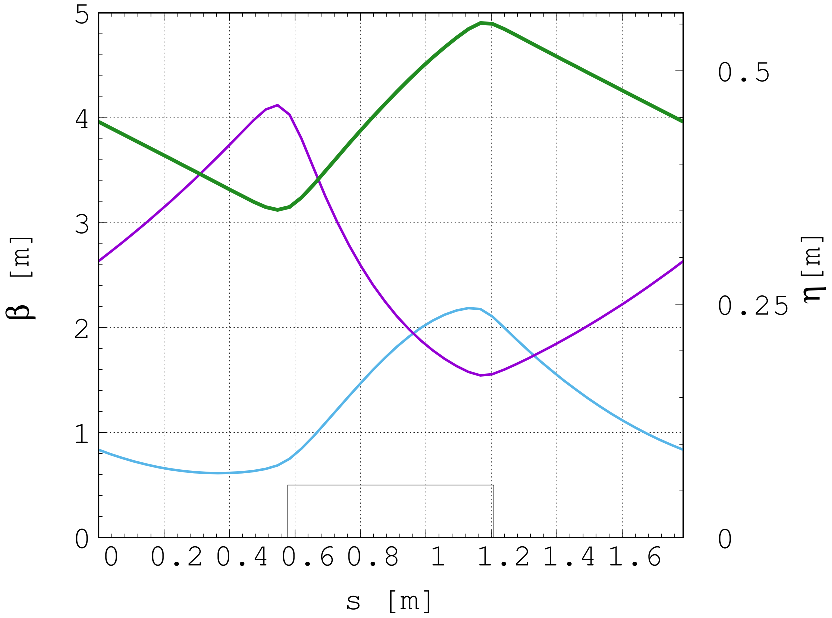

Figure 29: Twiss β_h (blue), β_v (purple) functions and dispersion (green) in one lattice cell of the FFA ring.

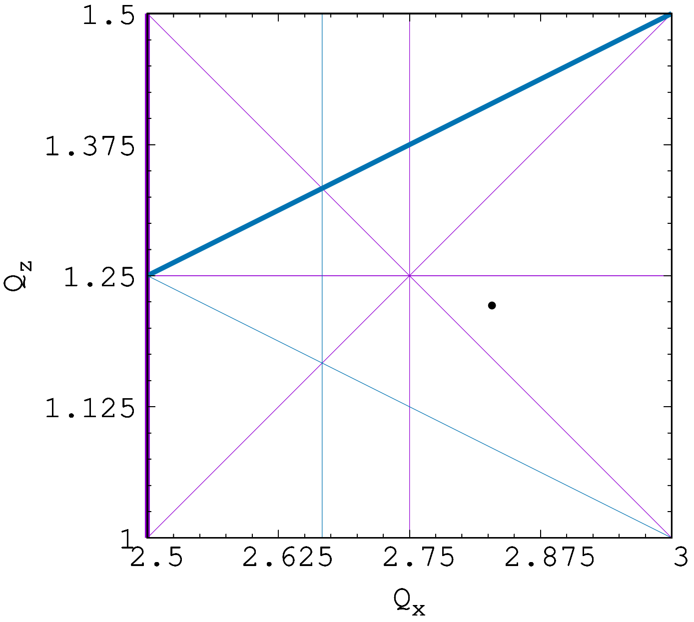

Figure 30: The working point of the FFA ring at (2.83, 1.22) on the tune diagram.

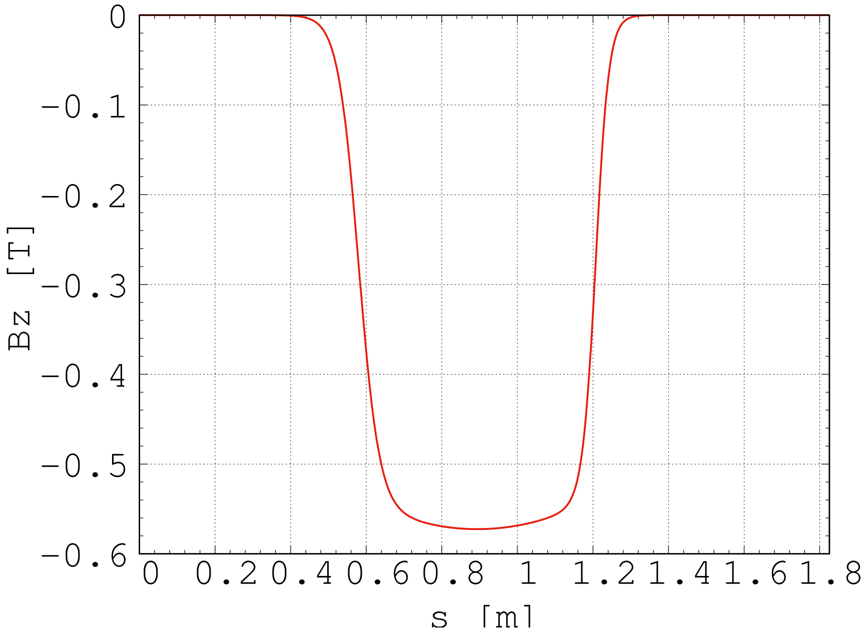

Figure 31: The magnetic field in one lattice cell on the median plane at injection.

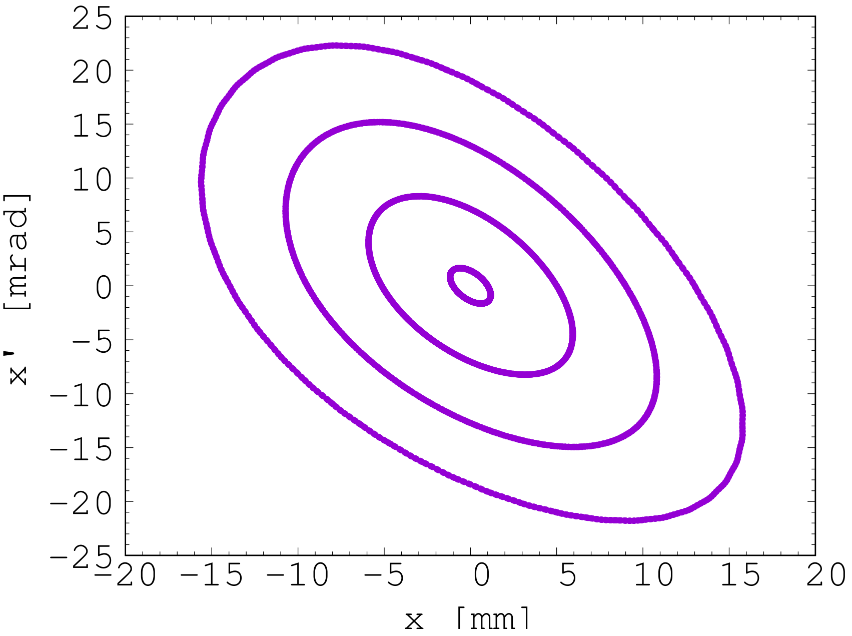

Figure 32: The results of the horizontal dynamical acceptance study in the FFA ring. A 1 mm offset is assumed in the vertical plane.

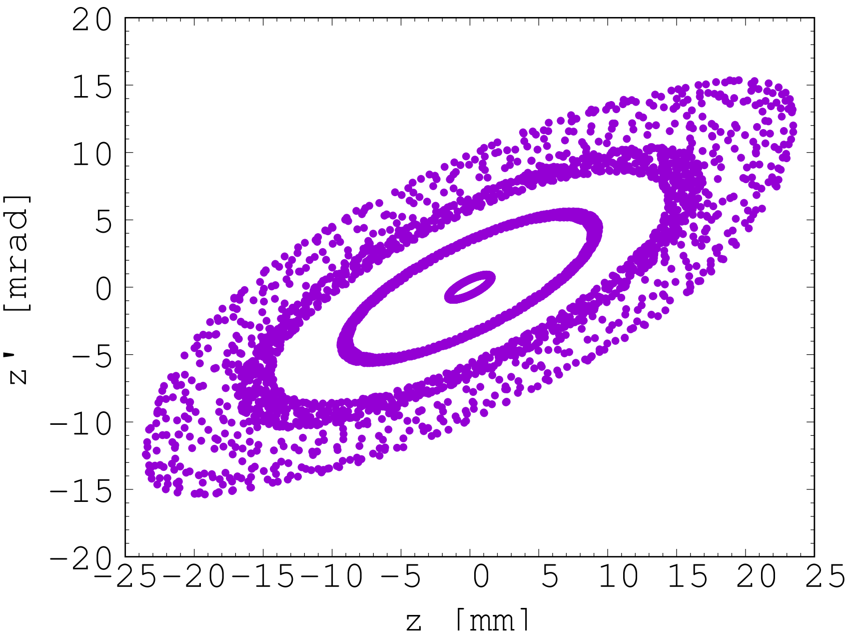

Figure 33: The results of the vertical dynamical acceptance study in the FFA ring. A 1 mm offset is assumed in the horizontal plane.

Table 5: Summary of the main parameters for the proton beam at the injection to the FFA ring. These parameters correspond to the nominal (maximum) acceleration mode of operation.

Parameter	unit	value
Beam energy	MeV	15
Total relative energy spread		±0.7%
Nominal physical RMS emittance (both planes)	π m rad	4.1×10^{-7}
Incoherent space charge tune shift		-0.2
Bunching factor		0.05
Total bunch length	ns	17.5
Beam intensity		5.7×10^{8}

Table 6: Summary of estimated parameters for the injection/extraction systems of the FFA ring.

Parameter	unit	value
Injection septum:		
nominal magnetic field	T	0.53
magnetic length	m	0.9
deflection angle	degrees	48.7
thickness	cm	1
full gap	cm	3
pulsing rate	Hz	10
Extraction septum:		
nominal magnetic field	T	1.12
magnetic length	m	0.9
deflection angle	degrees	34.38
thickness	cm	1
full gap	cm	2
pulsing rate	Hz	10
Injection kicker:		
magnetic length	m	0.42
magnetic field at the flat top	T	0.05
deflection angle	mrad	37.4
fall time	ns	320
flat top duration	ns	25
full gap	cm	3
Extraction kicker:		
magnetic length	m	0.65
magnetic field at the flat top	T	0.05
deflection angle	mrad	19.3
rise time	ns	110
flat top duration	ns	40
full gap	cm	2

$h = 1$ with an RF frequency range from 2.89 MHz to 6.48 MHz. The RF voltage required for 10 Hz operation corresponds to only 0.5 kV, however the energy acceptance at injection would be limited to $\pm 0.1\%$ so 8 kV is required to increase the energy acceptance to $\pm 0.7\%$, which is achievable with just two cavities [116].

Normal conducting spiral scaling FFA magnets, similar to the ones needed for LhARA, have been constructed successfully [114, 117] using two different techniques. The scaling field requirement was achieved either by distributing coils along the surface of a flat pole or by using a conventional gap-shaping technique to achieve the required field profile specified by the field index parameter k. The first method allows k to be tuned by applying different currents in each coil. For the LhARA FFA, we would envisage using a variation of the coil dominated design recently proposed at RAL in R&D studies for ISIS upgrade. In this design the nominal k is achieved using a flat pole surface and a distribution of windings along the pole with a single current flowing and the tunability of k can be achieved using up to three additional winding layers that can be powered independently. This reduces the number of independent power supplies needed, while providing the necessary tunability. The fringe field extent across the radius of the magnet needs to be carefully controlled by a field clamp in order to achieve zero chromaticity. An active clamp, in which additional windings are placed around one end of the magnet, may be used to control the flutter function to control independently the vertical tune of the FFA ring. In addition, since the magnetic field of the FFA ring needs to be adjusted to provide variable energy operation, a laminated design may be required in order to reduce the time for the field to change. The magnet gap of 4.7 cm given in table 4 is estimated assuming the flat pole design of the magnet. The details of the design will be addressed in as part of the R&D programme.

2.5.3 Extraction Line

To design the extraction line from the FFA it was assumed that the emittance of the 127 MeV beam at extraction will be determined by the nominal emittance of the 15 MeV beam at injection, which is $0.41\,\pi$ mm mrad. Acceleration in the FFA ring shrinks the emittance by a factor of three due to the adiabatic damping effect. In this scenario, the normalised emittance is assumed to be conserved from the start of the injection line to the end of the extraction septum. This defines the physical emittance at extraction to be $0.137\,\pi$ mm mrad (RMS).

In another scenario, the normalised emittance at injection is pessimistically assumed to be larger by a factor of 10, which means the physical emittance of the beam at 127 MeV will then be $1.37\,\pi$ mm mrad. Thus a particular Twiss beta value will give different beam sizes since the emittance is different in the two scenarios. This factor for the emittance growth was purposely chosen to be pessimistic in order to take into account the possible under-estimate of the space-charge effect in the GPT simulations and to make allowance for the fact that space-charge simulations in the injection line and the FFA ring have not been done.

A beam energy of 40 MeV was chosen for comparison with the maximum energy of 127 MeV as this has a smaller penetration depth of 15 mm in water compared to 120 mm for a 127 MeV beam. Table 7 gives the Twiss beta value for different beam sizes for 40 MeV and 127 MeV protons for the two scenarios assuming a Gaussian beam distribution. For variable energy operation in LhARA, the injection energy will be varied and the ring will always accelerate by a factor of three in momentum. This means the adiabatic damping factor will be the same and therefore the beam emittance for 40 MeV is the same as 127 MeV. This is valid assuming the optics and physical apertures that define the beam are approximately the same for all energies. However space charge will result in an energy-dependent effect on the emittance of the beam.

The first part of the extraction line takes the beam coming out of the extraction septum of the FFA, which has the optics parameters given in table 8. The beam then passes through two bending dipoles, that have differing lengths, and four quadrupoles, each of length 0.3 m, which brings the beam line parallel to the low-energy beam line and ensures that dispersion is closed. Closing the dispersion is critical as off-momentum particles will follow trajectories different to those followed by particles with the design momentum, which will

Table 7: Beam emittance values and target β values for different beam sizes for 40 MeV and 127 MeV beams. The beam size is taken to be four times the sigma of the transverse beam distribution.

	40 MeV protons (Nominal)	127 MeV protons (Nominal)	127 MeV protons (Pessimistic)
RMS Emittance (ϵ_x, ϵ_y) [π mm mrad]	0.137	0.137	1.37
β [m] for a 1 mm spot size	0.46	0.46	0.039
β [m] for a 10 mm spot size	46	46	4.5
β [m] for a 30 mm spot size	410	410	40

Table 8: Beam parameters at the exit of the extraction septum of the FFA used as input to the extraction line.

β_x [m]	β_y [m]	α_x	α_y	D_x [m]	Dp_x
1.0928	2.1003	0.6923	-0.9297	0.5506	-0.1813

significantly impact the size and shape of the beam downstream. The length of the extraction line up to this point is 6.55 m.

The second part of the extraction line consists of four quadrupoles each of length 0.3 m which transports the beam to the first dipole of the vertical arc beam line that serves the high-energy in-vitro end station. These quadrupoles are used to match the beam to the required beam size and produce a round beam. The last four quadrupoles are flexible enough that different $\beta_{x,y}$ values can be matched. However, it is not able to match the smallest target value of $\beta_{x,y} = 0.039$. Figure 34 shows the Twiss beta functions for five quadrupole settings that can match beams with $\beta_{x,y} = 410$ m in magenta, $\beta_{x,y} = 46$ m in red, $\beta_{x,y} = 40$ m in green, $\beta_{x,y} = 4.5$ m in black and $\beta_{x,y} = 0.46$ m in blue. The length of this part of the extraction line is 6.2 m, bringing the total length of the extraction line to 12.75 m.

2.5.4 High energy in-vitro beam line

The high energy in-vitro beam line transports the beam from the exit of the extraction line and delivers it to the high energy in-vitro end station. The 90° vertical bend is a scaled version of the low energy vertical arc and consists of two bending dipole magnets and six quadrupole magnets. To accommodate higher beam energies, the lengths of the magnets were scaled in order to ensure that peak magnetic fields were below the saturation limits of normal conducting magnets. The bending dipole magnet lengths were increased to 1.2 m each and the quadrupole lengths were tripled to 0.3 m each. The overall length of the arc then becomes 6 m, compared to 4.6 m for the low energy in-vitro arc. This difference in arc length means the high energy in-vitro arc is about 0.9 m taller than the low-energy arc. This height difference can easily be accommodated by having a longer drift after the low-energy arc.

The arc has been designed to fulfil the following criteria for the beam optics:

- $\beta_{x,y,\text{in}} = \beta_{x,y,\text{out}}$;
- $\alpha_{x,y,\text{in}} = \alpha_{x,y,\text{out}} = 0$;
- $D_{x,y,\text{in}} = D_{x,y,\text{out}} = 0$;
- $Dp_{x,y,\text{in}} = Dp_{x,y,\text{out}} = 0$;
- $\Delta\mu_x = n \cdot \pi$, where n is an integer; and
- $\Delta\mu_y = m \cdot \pi$, where m is an integer.

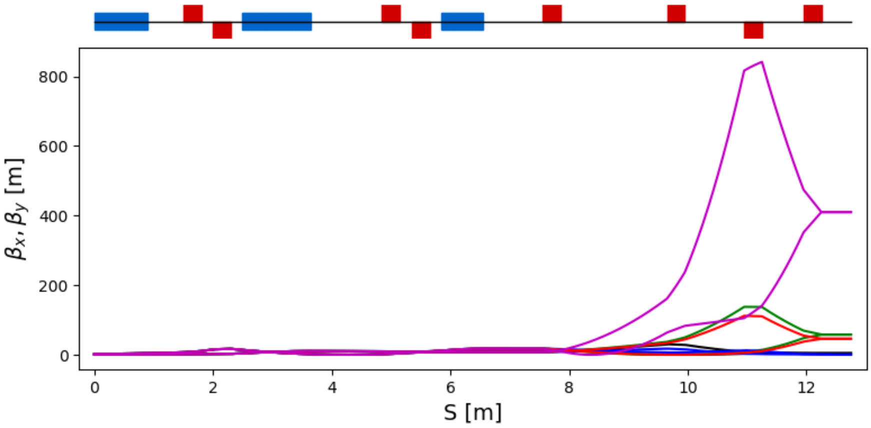

Figure 34: β_x and β_y functions for the full range of extraction beamline matching to $\beta_{x,y}$ = 410 m (magenta), $\beta_{x,y} = 46$ m (red), $\beta_{x,y} = 40$ m (green), $\beta_{x,y} = 4.5$ m (black) and $\beta_{x,y} = 0.46$ m (blue).

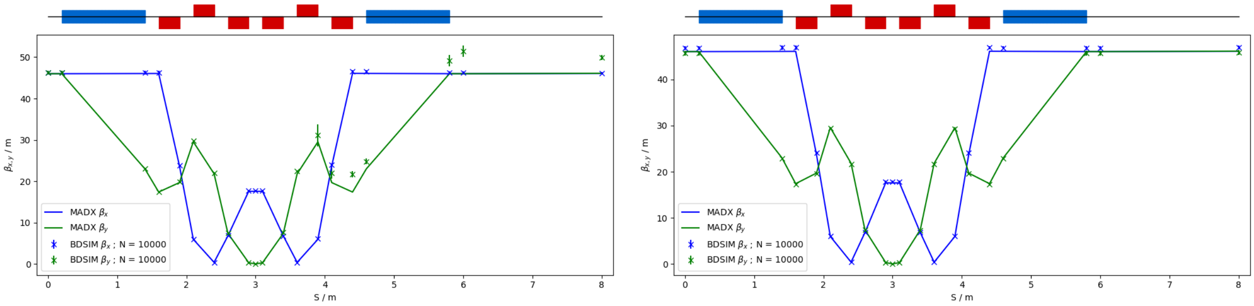

Figure 35: Comparison of MAD-X and BDSIM simulation of 40 MeV (left) and nominal 127 MeV (right) proton beam passing through the high energy in-vitro arc simulated with 10^4 particles (in BDSIM).

The quadrupole strengths for the scaled high-energy in-vitro arc that meet these criteria were obtained using MAD-X and tracking simulations using BDSIM show good agreement, see figure 35. The input beam distribution was assumed to be Gaussian and based on the Twiss parameters coming out of the extraction line and provided in table 9 which gives a beam size of about 10 mm.

GPT was used to investigate the effects of space charge and the beam size plotted as a function of length along the arc is given in figure 36. The GPT simulations used 10000 macro particles to represent a total bunch charge of 1×10^9. Space charge has a noticeable impact on the beam size for the 40 MeV and 127 MeV nominal emittance proton beams. It is expected, however, that the effects of space charge can be compensated to obtain the desired beam size in the matching section before entering the arc by modifying the quadrupoles in the arc.

GPT simulations of the pessimistic emittance 127 MeV proton beam through the high-energy in-vitro arc gives the results seen in figure 37. It can be observed that for $\beta_{x,y} = 4.5$ m entering the arc, there is a discrep-

Table 9: Beam parameters at the end of the extraction line used to design the high energy in-vitro arc and the in-vivo beam line.

β_x [m]	β_y [m]	α_x	α_y	D_x [m]	Dp_x
46	46	0	0	0	0

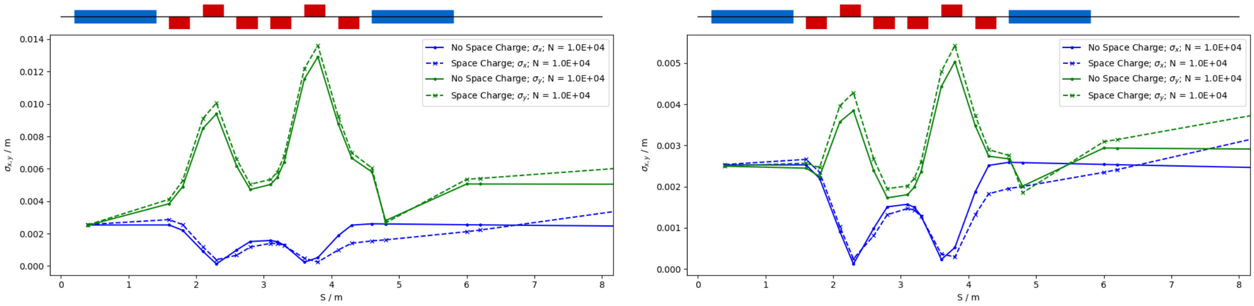

Figure 36: GPT simulation investigating the effects of space charge for a 40 MeV (left) and a 127 MeV (right) nominal emittance proton beam passing through the high energy in-vitro arc simulated with 10^4 macro particles. The solid lines are simulations without space charge and dashed lines with space charge.

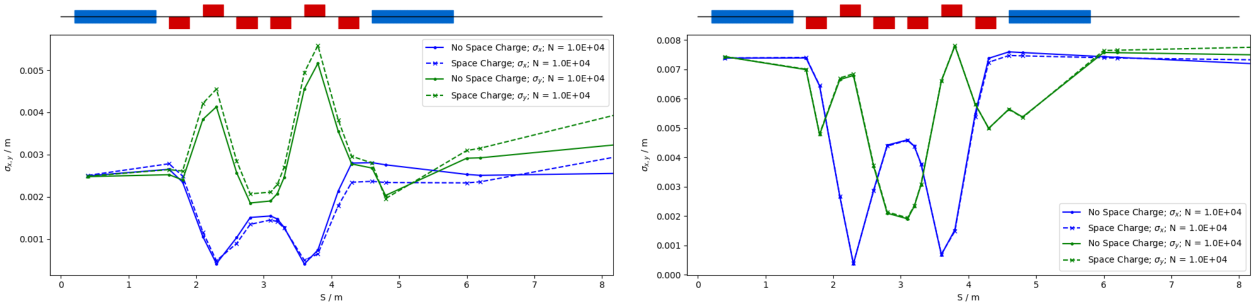

Figure 37: GPT simulation investigating the effects of space charge for a pessimistic 127 MeV beam distribution passing through the high energy in-vitro arc simulated with 10^4 macro particles. The beam distribution is generated with an initial $\beta_{x,y} = 4.5$ m (left) and $\beta_{x,y} = 40$ m (right). The solid lines are simulations without space charge and dashed lines with space charge.

ancy in the beam size exiting the arc due to space-charge effects similar to that seen for the nominal emittance beams. However, the larger beam size of $\beta_{x,y} = 40$ m shows a smaller discrepancy in the beam size due to space charge.

BDSIM was used to track the beam, without space-charge effects, from the start of the extraction line to before the vacuum window of the end station for a nominal emittance 127 MeV proton beam. The resulting evolution of the RMS beam size as a function of position along the beam line is shown in figure 38. It should be noted that these results are for $\beta_{x,y} = 46$ m at the input of the arc whereas the extraction line can provide a matched beam for the various Twiss beta values as shown in figure 34. Thus the beam size in the end station can be adjusted.

To investigate the range in water of the 127 MeV beam, a simulation with BDSIM was done from the start of the high-energy in-vitro arc through to the end station. For the purposes of the simulation, a similar design to the low-energy end station was used but with the air gap increased from 5 mm to 5 cm and a water phantom was placed at the end of the air gap instead of a cell culture plate. The water phantom used in the simulation was based upon the PTC T41023 Water Phantom. The simulation results given in figure 39 shows the Bragg peak for a monoenergetic 127 MeV proton beam is located at a depth of 16.9 cm, which is 10.9 cm into the water. A target volume was defined around the region of the Bragg peak from 16 cm to 17 cm with a diameter of 3 cm, which is equal to the size of the beam. The energy deposited within the target volume was found to be 231 GeV, which gives a dose of 5.2×10^{-6} Gy, or 0.58 Gy when scaled up to 10^9 protons.

For comparison, a 33.4 MeV/u carbon ion beam was also simulated through an end station design similar to the low-energy in-vitro end station, but with the cells replaced with water and the range of the carbon ions can

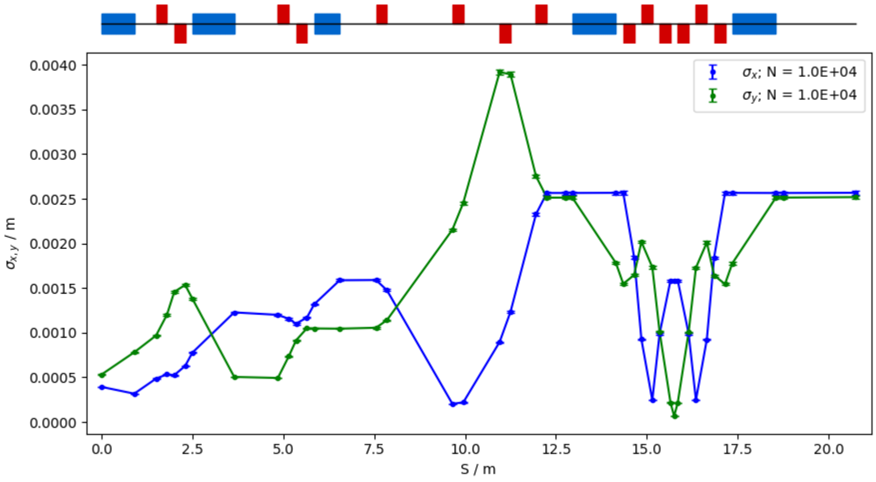

Figure 38: BDSIM simulation for a nominal 127 MeV proton beam from the start of the extraction line to the in-vitro end station where the extraction line quadrupoles are set to provide a matched beam with $\beta_{x,y} = 46$ m at the beginning of the arc. The plot shows the evolution of RMS beam size (in x and y) as a function of position along the beam line.

be seen in figure 40. The range in water for carbon ions is significantly less with a range of 3.3 mm. As before, studying the Bragg peak region at a depth in the end station between 9.5 mm and 10.5 mm gives an integrated deposited energy of 1258 GeV, which gives a dose of 2.85×10^{-5} Gy and a corresponding dose of 5.24 Gy for 10^9 carbon ions.

2.5.5 in-vivo beam line

If the first dipole of the high-energy in-vitro arc is not energised then beam is sent to the in-vivo end station. From the end of the extraction line, 7.7 m of drift is necessary to clear the first bending dipole of the in-vitro arc, to provide space for the five RF cavities needed for longitudinal phase-space manipulation and to allow space for diagnostic devices. Following this drift is a further 6.6 m of beam line that includes four quadrupoles, each of length 0.4 m, which are used to perform the final focusing adjustments of the beam delivered to the in-vivo end station. A final 1.5 m drift at the end is reserved for scanning magnets to be installed to perform spot scanning and to penetrate the shielding of the in-vivo end station. In total the in-vivo beam line is 15.6 m in length.

The optics are required to match the input beam parameters, given in table 9, to the exit conditions given in table 7. The design required a compromise between competing requirements of: flexibility to match to various values of $\beta_{x,y}$; minimising the number of magnetic elements in the beam line; and minimising the overall length of the beam line. Quadrupole settings were obtained using MAD-X, where additional care was given to avoid small $\beta_{x,y}$ values throughout the beam line to try to limit both space charge and kinematic effects.

The design is relatively flexible in matching various $\beta_{x,y}$ values, but is not able to match the smallest target value of $\beta_{x,y} = 0.039$ m. Figure 41 shows five separate settings for the four quadrupoles matching to $\beta_{x,y} = 410$ m in magenta, $\beta_{x,y} = 46$ m in red, $\beta_{x,y} = 40$ m in green, $\beta_{x,y} = 4.5$ m in black and $\beta_{x,y} = 0.46$ m in blue. With the exception of the settings for $\beta_{x,y} = 410$ m, which has a minimum of about 0.08 m, the other settings all have a minimum $\beta_{x,y}$ above 0.2 m.

To verify that the optics design could provide the required beam sizes, simulations were performed with

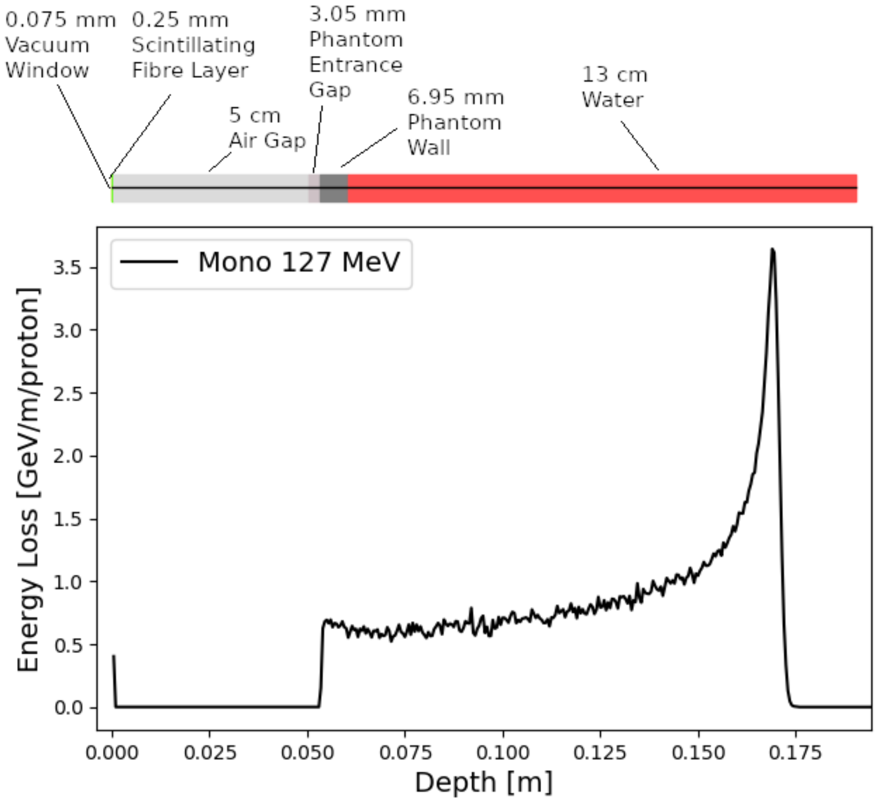

Figure 39: Simulation of the expected range in a water phantom for a 127 MeV proton beam.

BDSIM using an input Gaussian beam generated with the assumptions given in tables 7 and 9. Figure 42 shows the results of the simulation for a 40 MeV proton beam matched in order to obtain a beam size of about 1 mm, 10 mm and 30 mm. The simulations were repeated using GPT in order to investigate the effects of space charge, see figure 43. It can be seen that the effect of space charge for 40 MeV is non-negligible and causes discrepancies in the evolution of the beam size. However, it is expected that adjustments to the quadrupoles can be made to compensate for this effect in order to obtain the required beam size, though the 1 mm beam size case is clearly the most challenging.

Simulations for a nominal emittance 127 MeV beam shows overall agreement of Twiss beta between BDSIM and MAD-X, presented in figure 44. The quadrupoles have been matched to give $\beta_{x,y} = 0.46$ m, $\beta_{x,y} = 46$ m and $\beta_{x,y} = 410$ m. The simulations were repeated in GPT, see figure 45, and the results show that the effect of space charge causes some discrepancy in the resulting beam size. As in the case for the 40 MeV beam, adjusting the quadrupoles could compensate for the effects of space charge. The beam profile and phase-space plots at the end station from the GPT simulations with space charge are presented in figure 46.

In contrast, simulating the pessimistic 127 MeV proton beam in GPT shows space-charge effects have less of an impact on the beam size, as shown in figure 47. The quadrupoles were matched to give $\beta_{x,y} = 4.5$ m and $\beta_{x,y} = 40$ m.

Although for the larger beam sizes it is possible to obtain a parallel beam coming out of the last quadrupole, for the smaller beam sizes the beam needs to be focused as it comes out of the last quadrupole. This will have repercussions for the scanning magnets which will be located downstream of the last quadrupole and this requires further investigation.

BDSIM was used to simulate a 127 MeV proton beam, without space charge, from the start of the extraction line to the end of the in-vivo beam line with settings matched to $\beta_{x,y} = 0.46$ m. Figure 48 shows that the

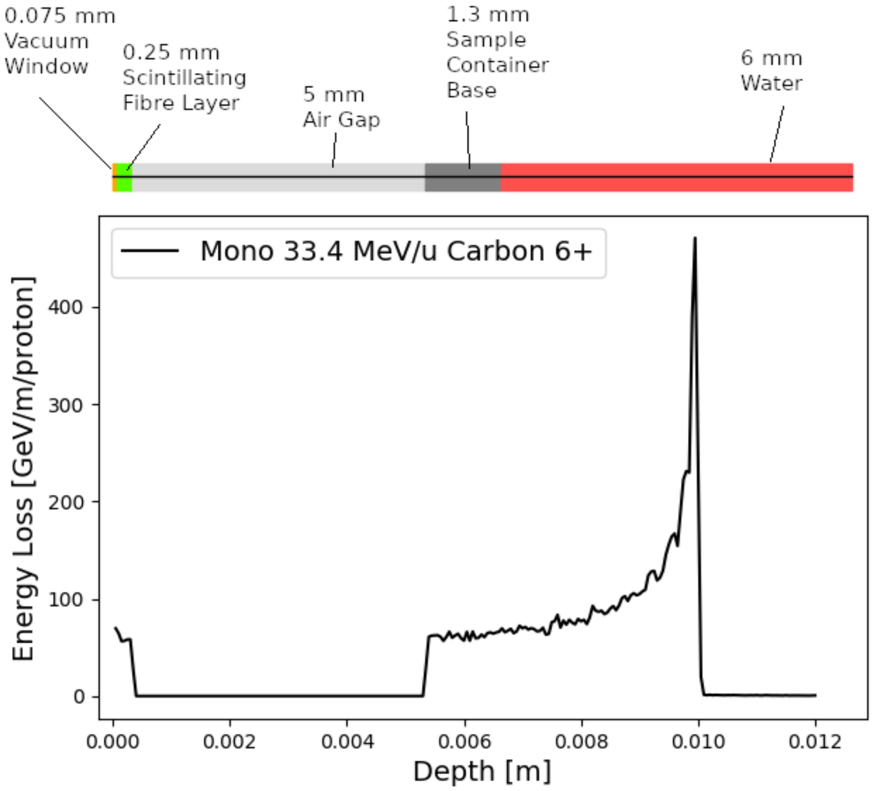

Figure 40: Simulation of the expected range in water for a 33.4 MeV/u carbon beam.

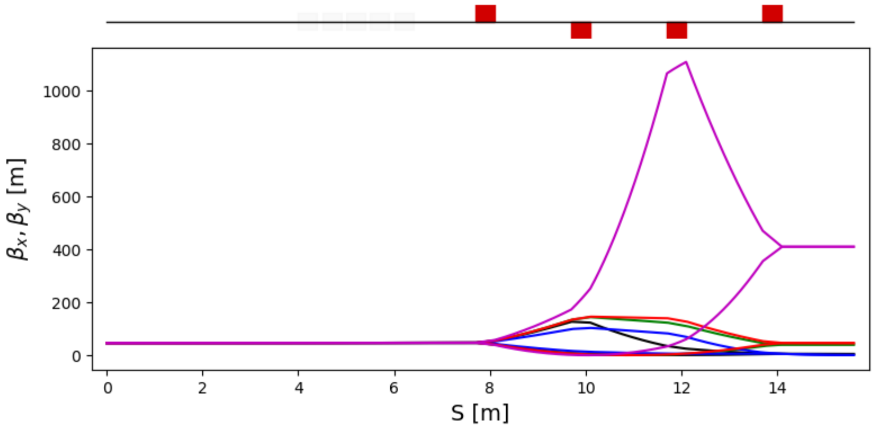

Figure 41: β_x and β_y functions for the in-vivo beam line matching from initial $\beta_{x,y} = 46\,\mathrm{m}$ to $\beta_{x,y} = 410\,\mathrm{m}$ (magenta), $\beta_{x,y} = 46\,\mathrm{m}$ (red), $\beta_{x,y} = 40\,\mathrm{m}$ (green), $\beta_{x,y} = 4.5\,\mathrm{m}$ (black) and $\beta_{x,y} = 0.46\,\mathrm{m}$ (blue).

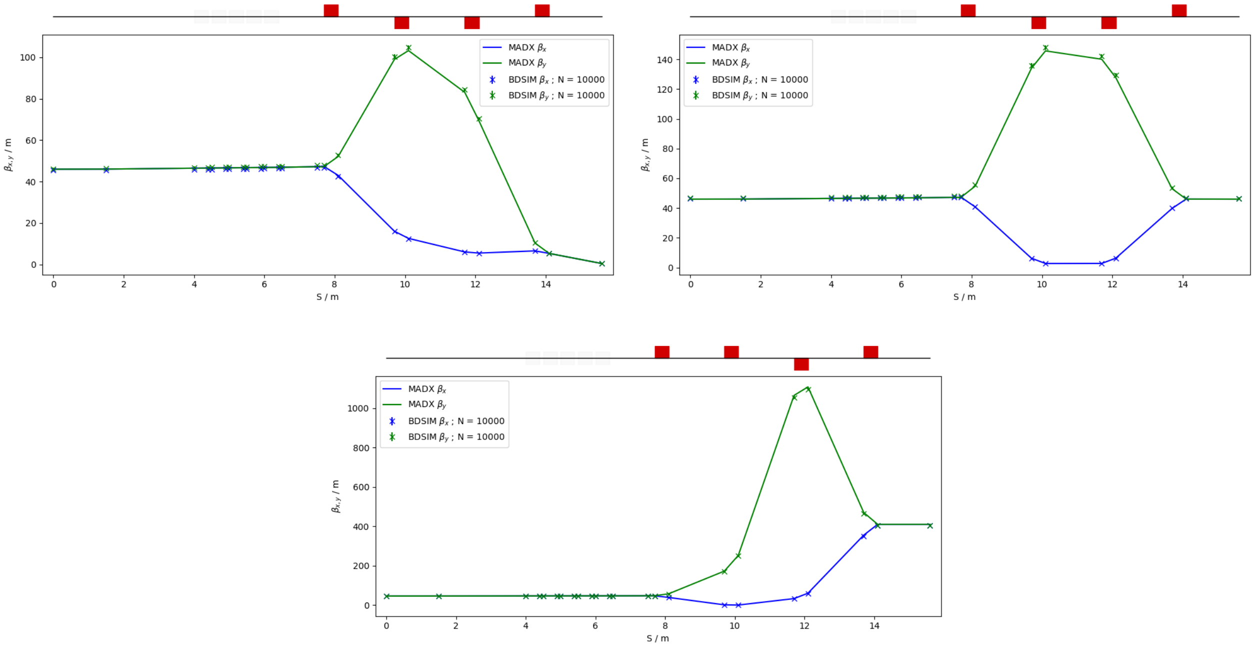

Figure 42: MAD-X and BDSIM comparison simulations of the in-vivo beamline for a 40 MeV proton beam with quadrupoles matched to $\beta_{x,y} = 0.46$ m (upper left), $\beta_{x,y} = 46$ m (upper right) and $\beta_{x,y} = 410$ m (bottom) for 10^4 particles.

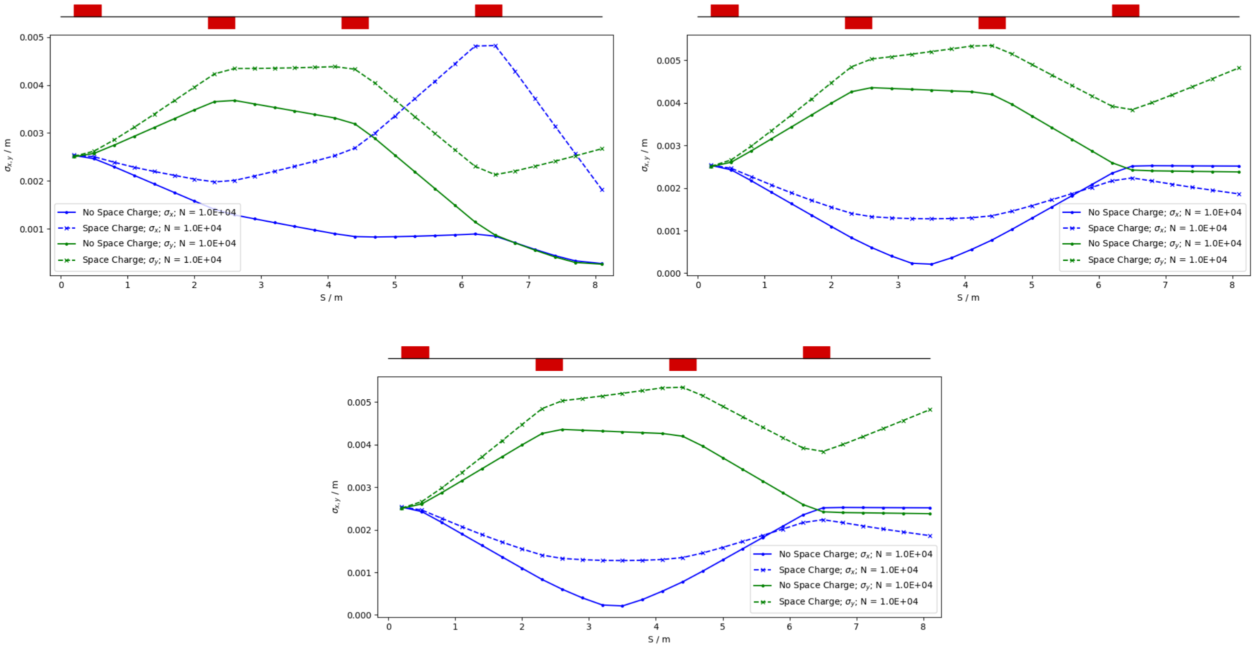

Figure 43: GPT simulations of the in-vivo beamline for a 40 MeV proton beam with quadrupoles matched to $\beta_{x,y} = 0.46$ m (upper left), $\beta_{x,y} = 46$ m (upper right) and $\beta_{x,y} = 410$ m (bottom) for 10^4 macro particles to investigate the effects of space charge. The solid line is for no space charge and the dashed line is when space charge is turned on.

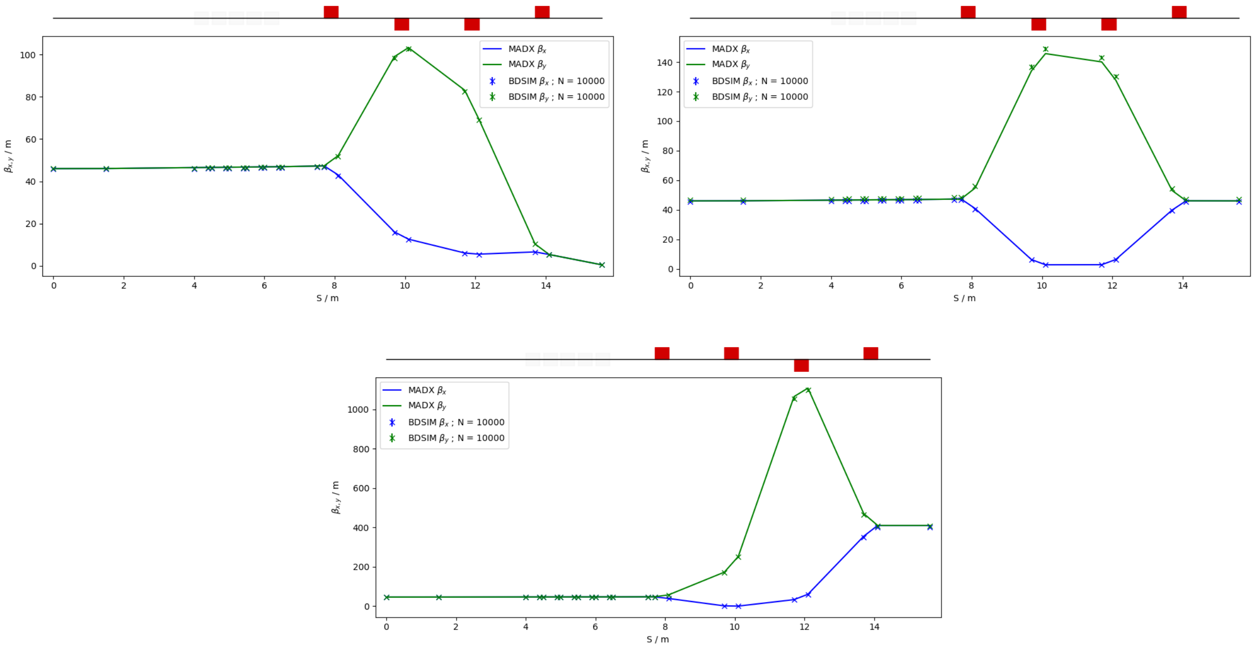

Figure 44: MAD-X and BDSIM simulations of the in-vivo beamline for a nominal 127 MeV proton beam with quadrupoles matched to $\beta_{x,y} = 0.46\,\mathrm{m}$ (upper left), $\beta_{x,y} = 46\,\mathrm{m}$ (upper right) and $\beta_{x,y} = 410\,\mathrm{m}$ (bottom) for 10^4 particles.

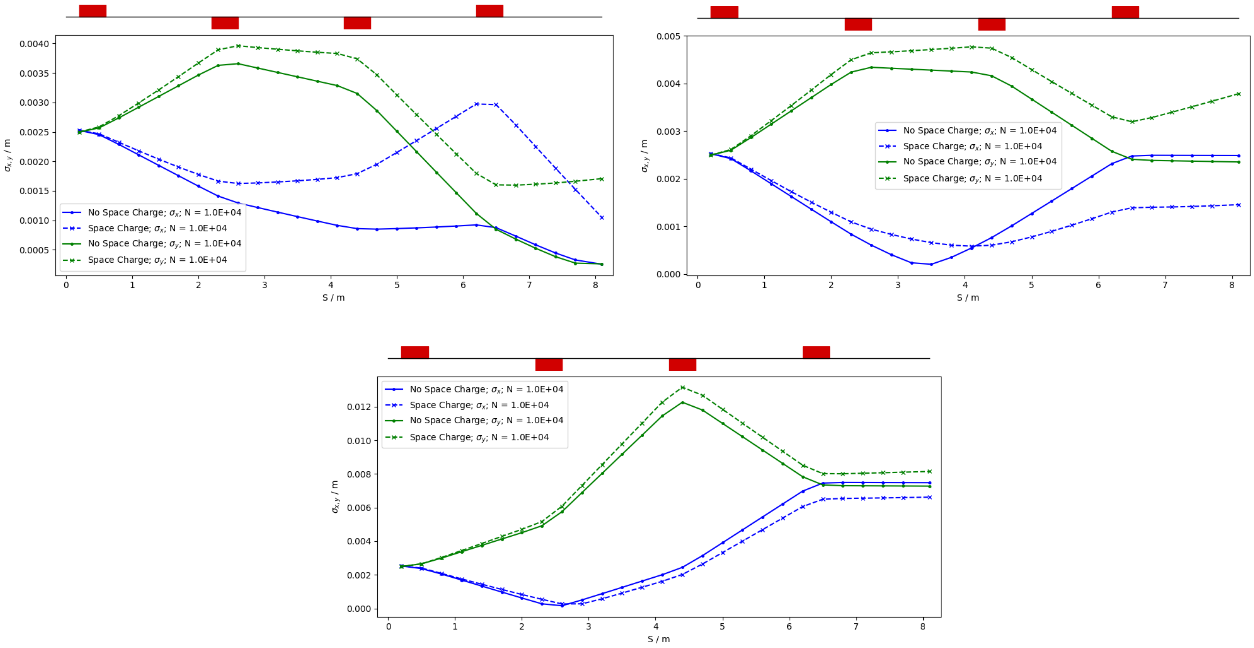

Figure 45: GPT simulations of the in-vivo beamline for a nominal 127 MeV proton beam with quadrupoles matched to $\beta_{x,y} = 0.46\,\mathrm{m}$ (upper left), $\beta_{x,y} = 46\,\mathrm{m}$ (upper right) and $\beta_{x,y} = 410\,\mathrm{m}$ (bottom) for 10^4 macro particles to investigate the effects of space charge. The solid line is when space charge is turned off, the dashed line when space charge is turned on.

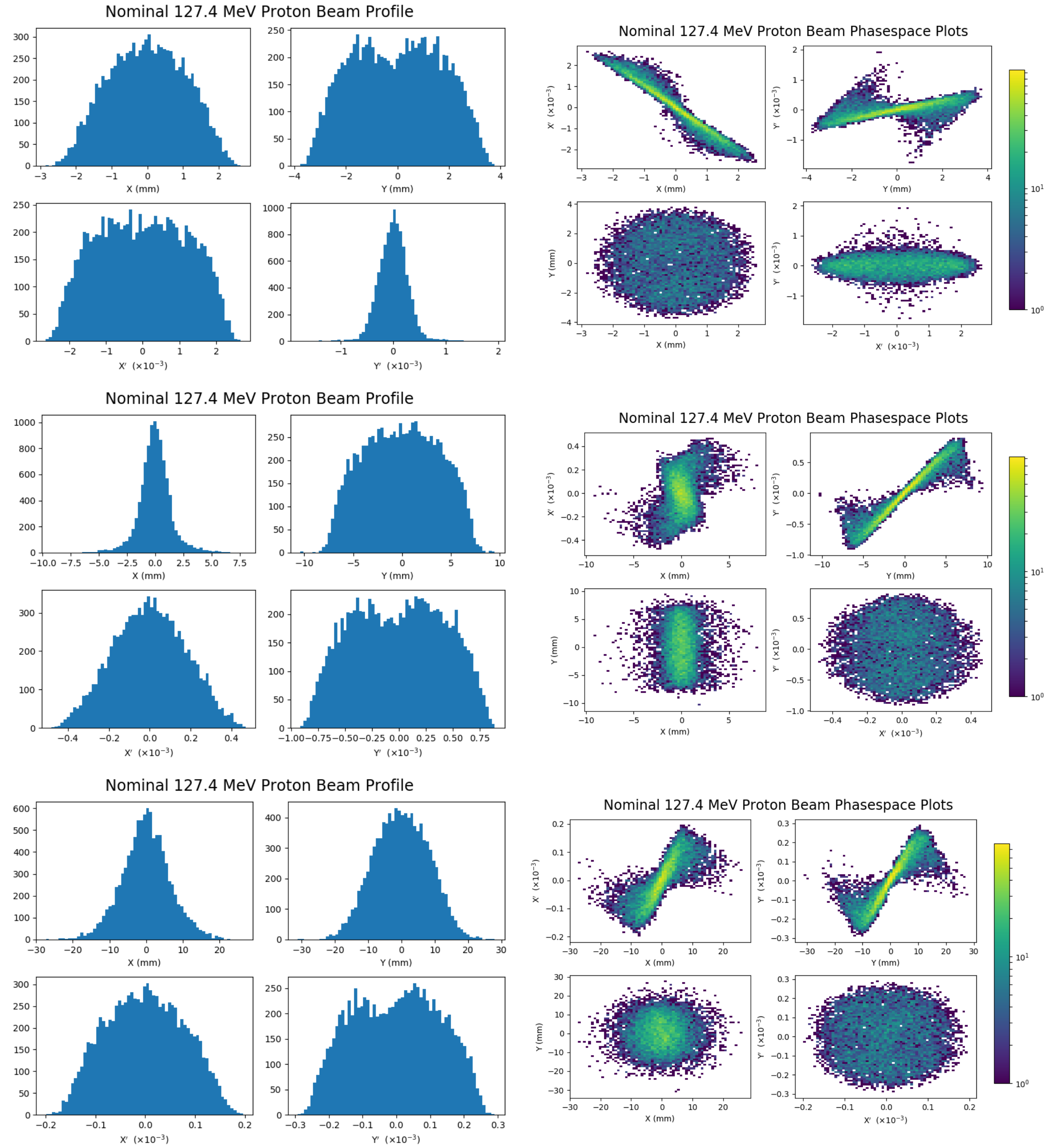
Nominal 127.4 MeV Proton Beam Profile

Nominal 127.4 MeV Proton Beam Phasespace Plots

Nominal 127.4 MeV Proton Beam Profile

Nominal 127.4 MeV Proton Beam Phasespace Plots

Nominal 127.4 MeV Proton Beam Profile

Nominal 127.4 MeV Proton Beam Phasespace Plots

Figure 46: Beam profile and phase space plots in the end station for the nominal emittance 127 MeV proton beam from GPT simulations with space charge on. The top plots are for quadrupole settings matched to $\beta_{x,y} = 0.46\,\text{m}$, the middle plots are matched to $\beta_{x,y} = 46\,\text{m}$ and the bottom plots are matched to $\beta_{x,y} = 410\,\text{m}$ for 10^4 macro particles.

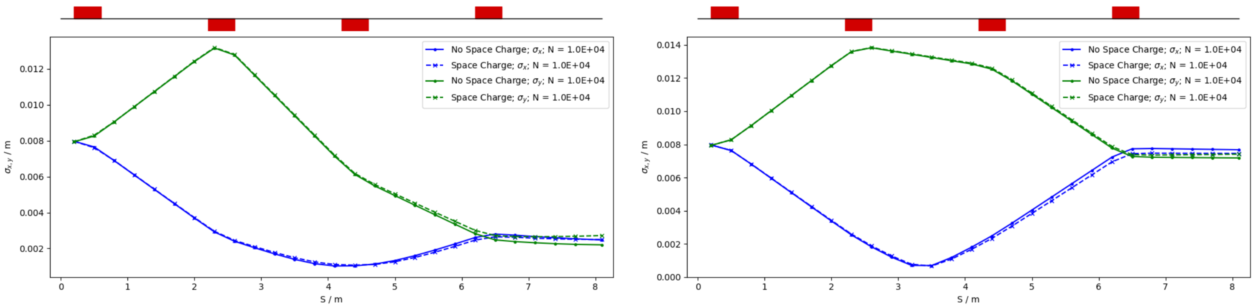

Figure 47: GPT simulations of the in-vivo beamline for a pessimistic assumption for the 127 MeV proton beam with quadrupoles matched to $\beta_{x,y} = 4.5$ m (left) and $\beta_{x,y} = 40$ m (right) for 10^4 particles to investigate the effects of space charge. The solid line is when space charge is turned off, the dashed line when space charge is turned on.

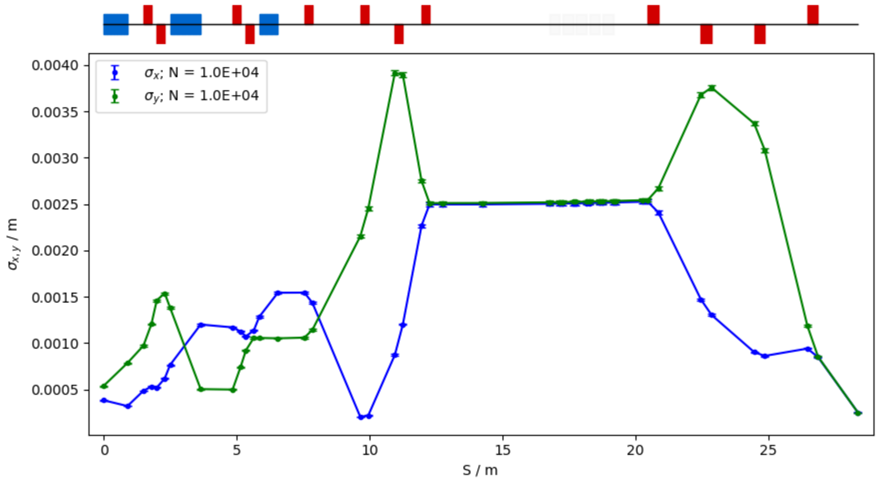

Figure 48: RMS beam size as a function of position along the beam line for a 127 MeV proton beam starting at the extraction line going through to the end of the in-vivo beam line. The final four quadrupoles are matched in order to obtain $\beta_{x,y}$ = 0.46 m.

required beam size can be achieved using the matched quadrupole settings, with the option to fine tune the quadrupole settings to optimise the beam size and shape.

2.5.6 Technical challenges and R&D programme

The R&D effort needed to realise the FFA post-accelerator is related to the spiral FFA magnet design and the FFA RF system. The magnetic field needs to satisfy the scaling law dictated by the zero-chromaticity condition and be tunable in order to alter the machine working point, which is needed for variable energy operation. The choice of technology for realising the magnet will determine whether a prototype magnet needs to be constructed. If the novel technology based on a flat pole surface with a distribution of windings and a single current flow is chosen, the construction of a proof-of-principle prototype will be necessary. The engineering design of the FFA magnet will dictate the extent of the fringe fields and the field leakage into the straight sections. This will influence the design of the injection line, the injection and extraction systems and the positioning of the RF cavities in the ring.

The other fundamental element of the FFA machine is the RF system. The parameters of the LhARA FFA ring and the requirements of the RF system leads to a choice of technology based on magnetic alloy loaded RF cavities [116, 118], to obtain the necessary RF frequency swing. Although such cavities exist and are being operated in a number of machines, they are not commercially available, in particular with the size constraints of the LhARA ring. The R&D task will require transferring the expertise in this technology to the UK, which will be beneficial for LhARA and potentially useful for other applications such as the ISIS upgrade at RAL.

The challenge of providing beams of various sizes, particularly the smallest beam size, to the high-energy in-vitro end station and the in-vivo end station will also require further study.

2.6 Instrumentation

It is convenient to divide the beam-line instrumentation into three parts: that required for the laser system; that required for the low-energy Stage 1 beam line; and that required for the FFA and the high-energy Stage 2 beam line. In addition to the instruments for the beam line itself, instruments for dosimetry in the end stations are required.

The beam characterisation techniques detailed in the following sections are considered primarily for proton beams. For ion beams the non-disruptive beam-line instrumentation can be adapted, depending on the bunch charge. Instrumentation that intercepts the beam will be destructive in the case of low ion-beam energy. Some alternative ideas on ion-beam instrumentation can be found in [119].

Instrumentation for monitoring of the systems, for example for the RF system and for the controls and monitoring system, will also be required. Such instrumentation is not expected to require specific development but will be included in the technical specifications of the relevant systems.

2.6.1 Laser system

It is proposed to use a Ti:Sapphire laser with a wavelength of 800 nm and delivering near 1 J of energy in 30 fs pulses, with a repetition rate of 10 Hz [120]. It is expected that the laser will be supplied as a turn-key unit from a suitable industrial vendor. The laser focal spot will be characterised using a camera-based system and high speed wavefront measurements. The techniques to be used are well understood and it is intended to buy the necessary equipment from commercial vendors.

2.6.2 Beam diagnostics for the low energy beam

Beam position and size measurements are necessary at the low-energy in-vitro end station. For the Stage 1 beam, the maximum energy of the protons depends on the power of the laser and is therefore directly related to the cost of the laser system. A compromise solution has been proposed, which allows irradiation of cell layers grown on the bottom of standard plastic culture containers. It is essential to have a means of characterising the beam at the end station. While Gafchromic film is capable of providing integrated beam dosimetry, a shot-by-shot characterisation using a very thin detector with a fast response is needed. A device known as the SciWire has been proposed [121], in which 2 planes of $250\,\mu$m square-section scintillating optical fibres, with the fibre directions in two planes orthogonal to each other, are mounted immediately on the air side of the mylar window. The arrangement of the scintillating fibres for a SciWire layer is shown in figure 49. Detection of the scintillation light from the SciWire fibres may be by CMOS cameras, or using photodiodes. If the instrumentation is sufficiently fast, it could be used to derive feedback signals for beam line steering. By placing several of these layers together, the energy-intensity profile of the beam can be measured from the

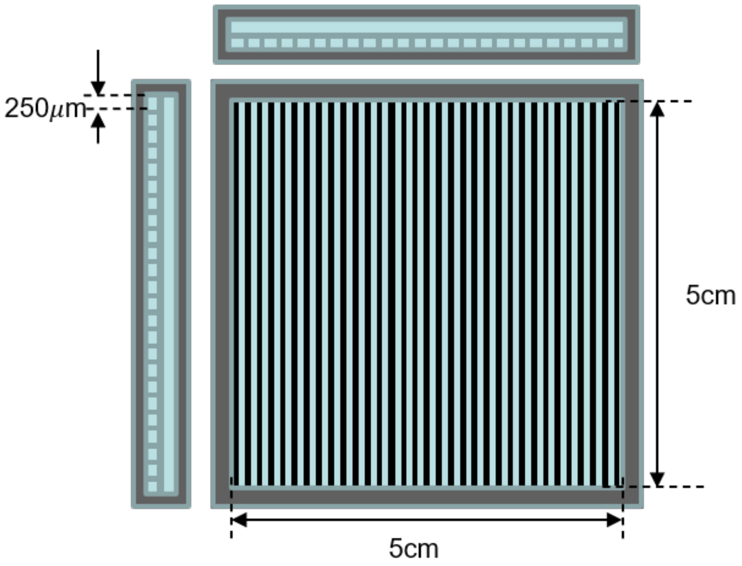

Figure 49: Arrangement of the 250 μm square cross-section fibres that make a layer of the SciWire detector. A layer consists of two planes of fibres orthogonal to each other.

penetration depth of the particles. This is a destructive measurement but can be useful as a diagnostic during the commissioning of the Stage 1 beam line and during operation.

Figure 21 shows the physical layout of the end station, with the beam passing through a single plane of scintillating fibres and impinging on the base of the cell culture container. The positions of the Bragg peaks are also shown for three different energies, namely 10 MeV, 12 MeV and 15 MeV. It can be seen that a beam energy of at least 12 MeV is necessary to be able to position the Bragg peak close to the cell layer. Since the Stage 1 design of LhARA will deliver a beam with a peak energy of 15 MeV, this may allow more than a single SciWire plane to be used, providing a 2D intensity profile.

An additional technology which might be evaluated is the use of monitors consisting of metal electrodes on very thin ceramic substrates, as reported in [122] and manufactured in industry [123]. This might provide an intensity profile measurement with very little disruption to the beam.

2.6.3 Beam diagnostics for the high energy beam

For the FFA and subsequent high-energy beam lines, existing facilities will be used as examples to provide the specification of the diagnostic systems needed for commissioning and during operation. It is expected that conventional beam instrumentation, such as beam-position monitors and beam-current transformers, will be sufficient in the transfer line to the in-vivo end station and the high-energy in-vitro end station, though the location of these devices and their performance with very high bunch intensities and short pulse widths needs to be investigated.

The design of the FFA for LhARA is based on the RACCAM project [124] and uses magnets with a large aperture in the horizontal plane. Such magnets require custom solutions to provide beam position measurements though similar measurements have been made at other facilities that utilise scaling FFA magnets with similarly large apertures, such as the Kyoto University Institute for Integrated Radiation and Nuclear Science (KURNS). The development of specialised diagnostics will be part of the R&D programme. The large aperture is challenging from the point of view of pickup design, with KURNS making use of multiple pickup electrodes spaced across the width of the vacuum chamber. The short, high current bunches are challenging for the electronics design.

The proton therapy facility at PSI uses a 250 MeV cyclotron, followed by transfer lines to the treatment rooms [125]. The extracted beam from the cyclotron is reduced to the desired energy by a carbon-wedge degrader, which is tuned in real time to give the desired depth of the Bragg peak in tissue. Space for instrumentation in a cyclotron is very limited, and the RF fields inside the machine are problematic. One probe is available, inserted radially and with 2 interchangeable heads. One head measures total beam current and the other used a scintillating screen and CCD camera to look at the beam profile and position. A kicker magnet is provided to dump the beam if requested by the patient safety system (PaSS). For initial setup of the cyclotron, test foils were placed in the beam [126]. This requires breaking the vacuum but can still be useful for initial alignment.

Beam current and profile are measured using ionisation chambers on the beam lines. These exist in different types, with full-area electrodes being used as a beam current measuring device and segmented electrodes being used to measure the profile. If an ionisation chamber is sufficiently low mass and the beam energy high enough, then it can be left in the beam permanently. Thicker chambers are mounted on pneumatic actuators so they can be withdrawn from the beam when not in use. Indeed, the movable chambers at PSI are made deliberately thick enough to cause enough disruption to the beam current, so that the PaSS system is triggered if a monitor is inadvertently left in the beam as treatment commences. If a monitor is to be in the beam permanently, it is best to place it at a point where the transverse beam size is small and the dispersion is large, to minimise the effects of scattering. Insertable monitors are separated from the vacuum by 35 μm thick Ti windows. The Position and Halo Monitor is an ionisation chamber with an open bore, which is mounted in a modified vacuum bellows such that it intercepts the beam halo, to provide a measurement of beam position and transverse dimensions. Halo monitors should be placed where the beam size is large. For very high beam currents, ionisation chambers may saturate and so secondary emission monitors (SEM) are used. These are made from thin parallel wires placed in the beam and the secondary emission current induced in the wires gives a beam profile. Beam position can be measured if 2 orthogonal planes of wires are used. At the PSI facility, a SEM is placed at the output of the cyclotron to monitor the beam injected into the beam lines. A destructive measurement of beam profile can be made using a fluorescent screen, viewed by a video camera positioned so as to be protected from radiation damage. Once again the screen is mounted on an actuator so it can be withdrawn when not in use. Beam loss monitors are usually placed downstream of bending magnets to detect beam instabilities and trigger the PaSS system in case of problems. In the straight sections multi-layer Faraday cups (MLFC) are provided, which can be inserted into the beam as a destructive measurement. A Faraday cup gives an absolute beam current measurement and a MLFC gives, in addition, the position of the Bragg peak (in copper). This can then be used to predict the position of the Bragg peak (in water) at the output of the beam line, or correlated with measurements on a water phantom. The MLFCs at PSI are made from sheets of copper 0.1 mm or 0.2 mm thick, separated by 75 micron Kapton insulators. The DAQ needs to be able to store calibration data etc. and apply corrections in real time. It is necessary to be able to find the beam centre from a profile, even when the profile may be non-Gaussian and possibly asymmetric. Custom electronics with wide dynamic range is used where needed and FPGAs can be used to perform fast fitting and pattern recognition of beam profiles.

In the prototype FFA EMMA at Daresbury Laboratory [127], the bunch executes up to 10 turns during acceleration with a spiral path that sweeps out half the pickup aperture (48 mm diameter). For accelerator tune measurements, a beam may be circulated continuously, at constant energy. EMMA is made up of 42 F-D cells, equipped with a total of 81 BPMs. A BPM consists of a button electrode pickup, 2 front-end modules close to the beam line and a VME module containing the ADCs. In the VME module, memory to store the pickup data for up to 4000 turns is provided. Research towards a US neutrino factory was geared towards an FFA [128] and in this case the instrumentation proposed is based on a system with one high-resolution 4-button BPM per quadrupole magnet. There are in addition 20 straight sections where beam-line instruments can be added and the instruments planned were: optical transition radiation (OTR) foils, phase probes for beam-RF comparison, a wall-current monitor and wire scanners. The extraction line will be equipped with a dispersive region for momentum measurement, a pepper-pot emittance monitor and a transverse deflection cavity with fluorescent screen for bunch shape measurements. An integrating current toroid or a Faraday cup was specified to provide beam charge measurements.

A suite of instruments for LhARA might include a system of BPMs to give position information throughout both Stage 1 and Stage 2 beam lines. Where these would be fitted and the geometry of the pickup blocks needs to be the subject of study and coordination with the accelerator designers. LhARA presents challenges which are different to those in the examples given here, particularly with respect to the large aperture of the FFA and the high intensity and short bunch structure of the beam. The response of beam pickups would need to be simulated and/or measured, due to the unusual geometry. Beam profiles could be measured by SEM grids on both Stage 1 and Stage 2 beam lines but these should be on pneumatic actuators for at Stage 1, to avoid scattering. Both the Stage 1 and Stage 2 beam lines might be fitted with MLFCs for a definitive measurement of beam current and the Bragg peak position (in copper). The MLFCs are a destructive measurement so would be mounted on pneumatic actuators, but backed up with integrating current transformers for normal running. Beam loss monitors would be placed next to bending magnets, as necessary.

2.6.4 Dose calibration for high-intensity beams

The development of appropriate approaches to dosimetry is a key challenge to be faced for the low-energy proton beams typically obtained with laser-target acceleration systems [129]. Dosimetric characterisation of the proton beam and the dose absorbed by biological samples will be achieved using a range of techniques. The aim is to develop online beam measurements, which will be calibrated against Nuclear track detectors (NTDs) and/or Gafchromic films (also termed radiochromic films, RCF). NTDs and RCFs will therefore be used as the standard for measuring the dose in the end stations and as a reference for other techniques such as the SmartPhantom.

The nuclear track detectors and Gafchromic films will first be optimised for the specific characteristics of the laser-driven proton beam. This will include correction and calibration factors due to the quenching of the detector response caused by the ionisation clustering of the low energy proton beam and the impact of high dose rate on the detector response. Detector characterisation will be carried out in conventional, well characterised, proton and photon beams.

2.6.4.1 Dosimetry of low energy laser-driven protons with nuclear track detectors

Nuclear track detectors (NTDs), such as CR39 plastic [130], and fluorescent nuclear track detectors (FNTDs), such as Al2O3:C,Mg crystals [131], can provide information on the fluence of the proton beam. It is then possible to estimate the dose rate and uniformity from the fluence. Moreover, following calibration with reference beams, it is possible to extract information about the energy distribution of the incident beam. Both detectors are biocompatible and a cell monolayer can be cultured on them. Used in combination with light or fluorescent microscopy, track detectors can provide very accurate information about the energy, location within the cell and number of proton traversals for each cell, making it a powerful tool for radiobiological investigations.

After exposure, CR39 detectors are developed by etching the plastic in a strong alkali solution, which etches preferentially along tracks where the polymer has been traversed by ionising particles. The etch rate is proportional to the ionisation density, yielding information on the energy of the incident particle. The tracks are measured using standard light microscopy.

FNTD crystals contain colour centres, which are capable of trapping secondary electrons from incident ionising particles. The electrons can be de-excited using light of a suitable wavelength, resulting in fluorescence near 750 nm. Confocal laser scanning microscopy can thereby be used to study particle or ion tracks. The strength of the fluorescence signal has been shown to correlate with Linear Energy Transfer (LET) along the track, which is itself an important quantity for characterising biological effects.

2.6.4.2 Dosimetry of low energy laser-driven protons with Gafchromic films

Gafchromic film can be used to make dosimetric measurements of low energy ion beams. The film provides high spatial resolution and stacking the film can provide information on the energy distribution of the incident beam. This enables the reconstruction of a detailed dose and LET map in the cell plane. For LhARA, a customised, unlaminated EBT3 film will be used, which is made with a protective layer on one side only. This means that, on the other side, the active layer can be directly exposed to radiation. The absence of a dead layer in front of it is a key requirement for low energy protons, which are characterised by very short range. Gafchromic films consist of a single or double layer of radiation-sensitive organic microcrystal monomers, on a thin polyester base with a transparent coating layer. Due to polymerisation of monomers by ionising radiation, the active layer colour becomes darker. Dose measurements are made by measuring through the optical density of the film using a scanner and visible light. The overall spatial resolution is mainly dominated by the resolution used in the scanner. To obtain a good compromise between pixel fluctuations and resolution, typically a resolution of 100-200 μm is used.

In the literature, it has been reported that there is a significant dose under-response in some Gafchromic film types, with increasing LET in the vicinity of the Bragg peak, see [132], [133] and [134]. This effect has been attributed to a saturation of the polymerisation process. As part of the R&D programme this effect will be characterised carefully in order to correct for it in dosimetric measurements.

2.6.5 Online dose monitoring

In order to verify the dose delivered to the sample, and measure any shot–to–shot variations, it is essential to be able to perform a measurement of the dose delivered in each shot while samples are being irradiated.W e therefore intend to develop custom instrumentation capable of measuring the dose from single shots, with NTDs and RCFs only being used for calibration purposes. For the low energy beam the possibility of using a SciWire layer for online dose measurements will be investigated in the R&D programme. In the current design, one plane of the SciWire is included, which would provide a 1D intensity profile. Using a SciWire layer, which adds another 250 μm of plastic in the path of the beam, would provide a 2D intensity profile and if the energy spread of the beam is sufficiently small, then the dose profile at the cell layer can be reliably calculated from this.

For the high energy proton beam, it is possible to sample energy deposition as a function of depth to determine the location of the Bragg peak and calculate the energy deposited in the sample. This concept is being developed for the SmartPhantom [135]. The SmartPhantom is a water phantom which is instrumented with scintillating fibres, in order to infer the dose distribution with distance through the phantom. A diagram of the arrangement is shown in Figure 50.

The detection elements of the SmartPhantom are based on 250 μm diameter polystyrene scintillating fibres. Each fibre station consist of 2 planes of fibres, in which the fibre directions are orthogonal. A beam's-eye view is shown in Figure 50 (left), showing how the 2 orthogonal planes of fibres cover the area to be irradiated. The outer green rectangle represents the water tank, the inner green rectangle the maximum beam size. The

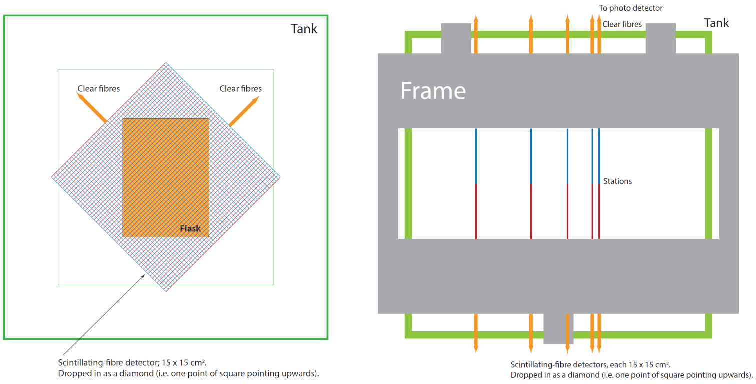

Figure 50: Arrangement of the SmartPhantom.

central shaded area covers the largest size sample flask for irradiations. A diagram of the assembled phantom from above is shown in Figure 50 (right), in which the 5 fibre stations are shown, mounted on a support frame (shown in grey) and inserted from above into the water tank (green rectangle). The beam is incident from the left in this view. The first prototype scintillating fibre planes for the SmartPhantom have been constructed, with experience having been gained in the fibre winding and gluing techniques.

Other approaches to online dosimetry include proton tomography, as researched by the PRaVDA collaboration, who have built a prototype silicon tracker for proton tomography [136]. Burker et al. [137] are developing a similar detector system to PRaVDA, in this case for ion tomography.

In proton radiotherapy, secondary neutrons from the proton interaction can lead to unwanted dose in healthy tissue. Gioscio et al. [138] have built a prototype 250 μm scintillating plastic fibre tracker with a SPAD array (fabricated by LFoundry), in order to monitor secondary neutron tracks.

2.6.6 Fast feedback controls and monitoring

For radiobiological studies, delivering precise quantities of dose and ensuring dose uniformity is very important. To smear out effects due to shot–to–shot variations, it is preferable to deliver the desired dose to a sample in many shots. It is then possible to compensate for such effects by adjusting the accelerator. However, since the accelerator will operate at 10 Hz, such a system would have to determine the dose delivered to the sample and then make the necessary adjustments to the accelerator within 0.1 s.

Taking again the example of the PROSCAN facility at PSI [125], the requirements of such a system can be investigated. Analogue signals from beam instruments need to be digitised and fed back to the machine control system (MCS). For example, the BPM currents (current signals from ionisation chambers here) are fed to a LogIV unit, which contains a logarithmic transimpedance amplifier and ADC. The LogIV unit then outputs digitised signals which are accessible via the VME backplane. The digitised signals are read by a VPC digital back end electronics module, which contains 2 FPGAs. The System FPGA runs the firmware common to all VPC applications, such as the high speed VMEbus interface to the MCS. The User FPGA runs the firmware which implements the local storage and processing algorithms. RAM is provided to store lookup tables (for example for linearising pickup signals) and instrument waveforms for readout via the MCS. The User FPGA is used to calculate quantities derived from raw pickup data, such as total beam current, beam vertical position, beam horizontal position, beam sizes, etc. Limits can be set on parameters which can be used in an interlock system, via fast optical data links. BPM data is sampled at 5kHz and fed back to the MCS for applying beam corrections.

Since LhARA is a unique facility the specific requirements and technologies needed to deliver a fast feedback and control system may be somewhat different, therefore the development of a fast feedback and control system will be part of the R&D programme.

2.6.7 Technical challenges and R&D programme

Several technical challenges have been highlighted that will be addressed in the R&D programme. The general instrumentation needs of LhARA will also be addressed with input from beam instrumentation experts, beam controls experts and the accelerator designers to ensure the solutions eventually chosen are optimal. In particular it is necessary to understand where commercially available solutions can be used and where custom solutions are needed, preference being given to commercially available solutions wherever practical.

The areas to be investigated in the R&D programme are outlined in the following subsections.

2.6.7.1 Online dosimetry and dose profile

This includes the development of the SmartPhantom concept to provide online dose measurements in the high-energy end stations and the development of the SciWire concept and thin ceramic monitors for dose profile measurements in the low energy in vitro end station.

2.6.7.2 Absolute dosimetry at ultra-high dose rates

This will focus on the measurement and characterisation of nonlinear response of film detectors at high dose rates and investigate the ability to use films for calibrating the online dose monitors.

2.6.7.3 Low energy beam diagnostics

The SciWire concept and the use of thin ceramic films for online beam intensity profile measurements and offline energy profile measurements will be developed. The application of conventional diagnostics for non-destructive beam-current and beam-position measurement will be investigated as well as destructive (high accuracy) beam current measurements using conventional technologies, such as multi-layer Faraday cups, for calibrating the non-destructive measurements. Destructive emittance measurements using conventional technology such as slit-grid/slit scanners or pepper-pot emittance monitors will be studied.

2.6.7.4 Fast feedback and controls

Initially the R&D for the fast feedback system will focus on Stage 1 and will be dependent on specifics of the low-energy beam instrumentation and online dose measurement. The accelerator response and tuning capabilities will need to be studied as well as development of an automated system for tuning the beam. This would require online simulation of the beam transport and material interactions in the end station. This could be done using a Monte Carlo simulation of the LhARA beam line that would run on firmware. This can then be extended to include the Stage 2 accelerator components.

2.6.7.5 High energy beam diagnostics

This will mainly focus on developing a beam position measurement device for the FFA. The application of conventional diagnostics for beam current, position and profile measurement in the transfer lines will be investigated including the ability to measure bunch length, which is important in the transfer line to the in vivo end station. Emittance measurements using conventional technology will also be investigated.

2.7 Software and computing

Software and computing is needed throughout the LhARA programme for simulation; controls and monitoring; data acquisition; and offline processing. A number of simulation activities that are required during the R&D programme will require access to existing high-throughput computing (HTC) farms, high-performance computing (HPC) farms and dedicated servers. Smaller computing platforms and stand-alone machines will be needed for the experimental activities, some of which may be shared by a number of activities. Other resources, such as software licenses, will also be managed as a shared resource.

During the design studies, detailed design and, later, in the operational phase, various components of the facility will need to be simulated. Some of the main types of simulation that would need to be performed are:

- Particle tracking of the beam line;
- Particle interactions with materials for dose estimation and radiation shielding design;
- Finite element analysis of electromagnetic fields and mechanical properties such as stress, thermal expansion, etc.);
- Space charge simulation; and
- Plasma simulation of the interaction of the laser with the target.

Particle tracking and dose estimation simulations are better suited to HTC farms whereas the other simulations would benefit from the use of HPC farms. Software not compatible with an HPC farm would need to be installed on a dedicated stand-alone server such as an Intel Xeon server with 192 Gb RAM and 40 cores.

In operation the LhARA facility will generate data from its various accelerator and instrumentation components which must be integrated into a global data acquisition system to provide a common interface and to allow synchronisation of data and communication across systems. After acquiring the data, common processing will be required, for example to calibrate the data and to pack it in a common container for storage. There are a number of accelerator and instrumentation components being studied in the R&D programme and as part of this experimental work, specific interfaces to the global data acquisition system can be developed.

A controls and monitoring system will need to be developed to run the LhARA facility. This will include a user interface that will provide controls for the various components of LhARA and display monitoring information about the state of the components, the state of the personnel protection system and information about the operational environment. The controls and monitoring system will therefore need to interface to a variety of equipment, with some devices requiring low-level communication and specific interface hardware.

2.7.1 Technical challenges and R&D programme

While there are no major technical challenges foreseen for the software and computing needs of LhARA, specific computing platforms will need to be developed, primarily for data acquisition and for controls and monitoring. The details mentioned above outlines the requirements of the various components of LhARA and the computing resources and capabilities needed. In addition to the hardware resources required, staff will be needed to develop the systems, provide technical support and to manage this activity.

The R&D programme includes the development of the data acquisition system and the controls and monitoring system to be used for running the LhARA facility. The development of the global data acquisition system will include the hardware and software needed to process and store data from the various components of LhARA though interfacing to specific systems will be done as part of the development of that system. Similarly, the controls and monitoring system will provide a high-level interface to the various components of LhARA though low-level control will be done as part of the development of that component.

2.8 Biological end stations

Our ambition is that LhARA serves a systematic programme of radiobiology through which the microbiological effect of different ion species on cellular biology can be determined and a detailed, quantitative understanding of the underlying mechanisms can be developed. In order to achieve this, high-end and fully equipped in-vitro and in-vivo end stations will be housed within the LhARA facility that address the radiobiological research requirements.

2.8.1 In-vitro end stations

Beam to the in-vitro end stations will be delivered vertically. These beams will be used for the irradiation of 2D monolayer and 3D cells systems (spheroids and patient-derived organoids) in culture. One of the end stations will have a beam line capable of delivering up to 15 MeV protons, whereas the second end station will house a beam delivering 15–127 MeV protons and up to 33 MeV/u carbon ions. The vertical nature of the beam allows the cell culture dishes and other vessels to be kept flat, which is important for both the health of the cells but also to optimise throughput of multiple irradiations.

The beam line within the end-stations will be housed within sealed units/chambers which will be directly sourced with the appropriate gases (carbon dioxide and nitrogen), allowing for the cells within plates/dishes to be incubated for a short time in stable conditions prior to and during irradiation. This will also enable the chamber to act, where necessary, as a hypoxia unit used to mimic the micro-environment of solid tumours where the oxygen concentrations of which can be significantly lower (from 0.1–5%) than the surrounding normal tissues. The high dose rate, “FLASH”, has been heavily linked with oxygen depletion, so the ability to house cells in specific oxygen concentrations will allow further investigation of the underlying biological mechanisms and identification of optimal delivery conditions into this radiotherapy modality for normal tissue sparing and local tumour control. Furthermore, the sealed units will contain robotics to enable simple movement of the numerous cell culture plates/dishes housed within to be placed in front and away from the beam line (see section 2.8.3). Having two separate end stations, along with the associated multiple workspaces, will increase the productivity of the research when multiple groups/researchers are using the in vitro end stations.

The in-vitro end stations will be housed within a research laboratory equipped with the up-to-date and state-of-the-art facilities required for developing successful and productive radiobiology research programmes. These facilities will be used to carry out exhaustive investigations into various biological end-points in both normal and tumour cell models, and which will be developed based on our experience of having established an in-vitro radiobiology laboratory at the Clatterbridge Cancer Centre that has been used successfully to enhance radiobiology research using protons beams [42, 139]. Therefore, not only will the laboratories allow RBE measurements through routine clonogenic assays, but will expand significantly on the examination of more complex biological end-points (e.g. senescence, autophagy, inflammation and angiogenesis). The research laboratory will include all the vital equipment and machinery for bench top science, sample processing and analysis, such as refrigerated centrifuges and microscopes (e.g. light and fluorescent microscopy), along with the equipment required for contaminant-free cell culture (e.g. humidified CO2 cell culture incubators, Class II biological safety cabinets), and for the storage of biological samples and specimens (e.g. $-20°$C/$-80°$C freezers and fridges). There will also be a robotic workstation which will be used for the handling and processing (e.g. harvesting, counting and plating of cells into multi-well plates) of large sample numbers post-irradiation, which will particularly assist in high-throughput screening experiments (e.g. drug-radiation combinations, siRNA/CRISPR-Cas9 screens).

Two specific pieces of equipment important to the radiobiology research programme are a hypoxia chamber and an X-ray irradiator. As mentioned above, the hypoxia chamber will allow cells in culture to be incubated in different oxygen concentrations mimicking those particularly of solid tumours, but this unit will be separate from the in vitro end-stations to allow processing of cells post-irradiation but also the analysis of biological end-points requiring long term incubation in a hypoxic environment. The X-ray irradiator is central because it will allow direct comparisons between the cellular response (e.g. relative biological effectiveness; RBE) to conventional X-ray irradiation, and proton and carbon ions delivered by the accelerator. Finally, an ultra-pure water system will provide the laboratory with highly purified and distilled water which is crucial for highly sensitive and precise biochemical assays and experiments.

The ability to perform biological research in vitro to the highest degree of quality and having the facilities to use a myriad of techniques and experiments yielding data on numerous biological end-points is imperative to the discovery and understanding of the cellular response to the various types of particle irradiation provided by the LhARA beam. Furthering our knowledge of the underlying biological mechanisms, but also the impact of dose delivery and combinatorial treatments, through in vitro research will allow particle beam therapy to be translated into future effective patient treatment.

2.8.2 In-vivo end station

The in-vivo end station will be housed on the basement floor and will be served with protons with energies of up to 127 MeV and carbon ions with energies up to 33 MeV/u. These beams will be capable of penetrating deeper into tissues allowing the irradiation of whole animals. The ability to perform in-vivo preclinical studies is vital for the future effective translation of the research into human cancer patients where optimum treatment strategies and reduction of side-effects can be defined. The in-vivo end station will allow the irradiation of a number of small-animal models (e.g. xenograft mouse/rat models) which can further promote an examination of particular ions on the appropriate biological end-points (e.g. tumour growth). The end station will contain a small-animal handling area which will allow for the anaesthetisation of animals (e.g. mice) prior to irradiation. To enable the irradiation of small target volumes with a high level of precision and accuracy, an image guidance system (e.g. computed tomography) will be available. The animals will subsequently be placed in temperature-controlled holder tubes enabling the correct positioning of the relevant irradiation area in front of the beam line. There will be allowance for measurements using Gafchromic film and other diagnostics as the beam enters the end station, enabling accurate dosimetry. The beam size is sufficient to give flexibility in the different irradiation conditions, in particular through passive scattering, pencil beam scanning, and micro beams illumination (via collimation), to be investigated at both conventional and FLASH dose rates. It is envisaged that the animals post-irradiation will be then taken off site at a nearby animal-holding facility for a follow-up period where biological measurements (e.g. tumour growth or normal tissue responses) will be conducted.

2.8.3 Development of radiobiological capability

Automated sample processing via robotics is essential to the radiobiology programme in order to promote the processing of large sample sizes, as well as the use of high throughput screens. Separate from the robotic workstation present in the research laboratory, robotics will be housed within the sealed chambers in the in-vitro end stations, and will be developed to accommodate a range of different formats (e.g. multi-well cell culture plates, and dishes). The robots will be programmed to enable movement of the plates/dishes to precisely position the cells in front of the beam line for irradiation, before then moving them to an appropriate area within the chamber for incubation. This would reduce manual handling time, but also significantly speed up the irradiation times of samples within individual plates/dishes (or areas within the multi-well plates), and ultimately the amount of biological results and data that can be generated in a single irradiation session.

Another area that would be useful to explore is the comparison of the results of cell irradiations with simulation data. Several codes exist that predict DNA damage patterns by simulating micro-track structures. The possibility of studying this with LhARA will be investigated.

2.9 Staging considerations

The configuration of LhARA, in which the beam from the laser-driven source is transported directly to the low-energy in-vitro end station and accelerated to serve both the high-energy in-vitro end station and the in-vivo end station, makes it natural to propose that the LhARA be constructed in two stages. The facility will be sited either in an existing building or a new, purpose-built, building. The principle components of Stage 1 include:

- The laser and target;
- The proton and ion capture, matching and energy selection sections;
- The 90° bend that takes the beam to the low-energy end station; and
- The low-energy in-vitro end station.

The installation and commissioning of these components will be coordinated so as to maximise the scientific output of LhARA. Thus, prior to the completion of the construction of Stage 1, the goal will be to achieve the following scientific milestones:

- First demonstration of the capture of a laser-driven ion beam using a Gabor lens system;
- Demonstration of the energy selection capabilities of a Gabor lens system;
- Irradiation of cells with a laser-driven ion beam.

Stage 2 will then incorporate:

- The injection line to the FFA;
- The FFA;
- The extraction line from the FFA and the transfer line to the in vivo end station;
- The high energy in vitro arc;
- The high energy in vitro end station; and
- the in vivo end station.

Staging LhARA in this way will allow the performance of the laser and capture system to be optimised whilst at the same time delivering an in-vitro radiobiology programme using 15 MeV protons and maximising scientific output throughout the construction of both stages. This would require the capability to deliver beam to the low-energy in-vitro end station during installation and commissioning of Stage 2, which would require additional shielding and personnel protection. The options for staging and the impact on the scientific programme will be studied as part of the conceptual design.

The design of LhARA includes the capability to manipulate the longitudinal phase-space of the beam. This would allow the study of radiobiological effects with bunches that have a very short spread in time or allow the reduction of the energy spread of the bunch. Space has been allocated in the Stage 1 beam line and in the transfer line to the in-vivo end station to incorporate the RF cavities needed for this. The potential for manipulating the longitudinal phase space and the design of the RF cavities will be studied in the R&D programme. There are

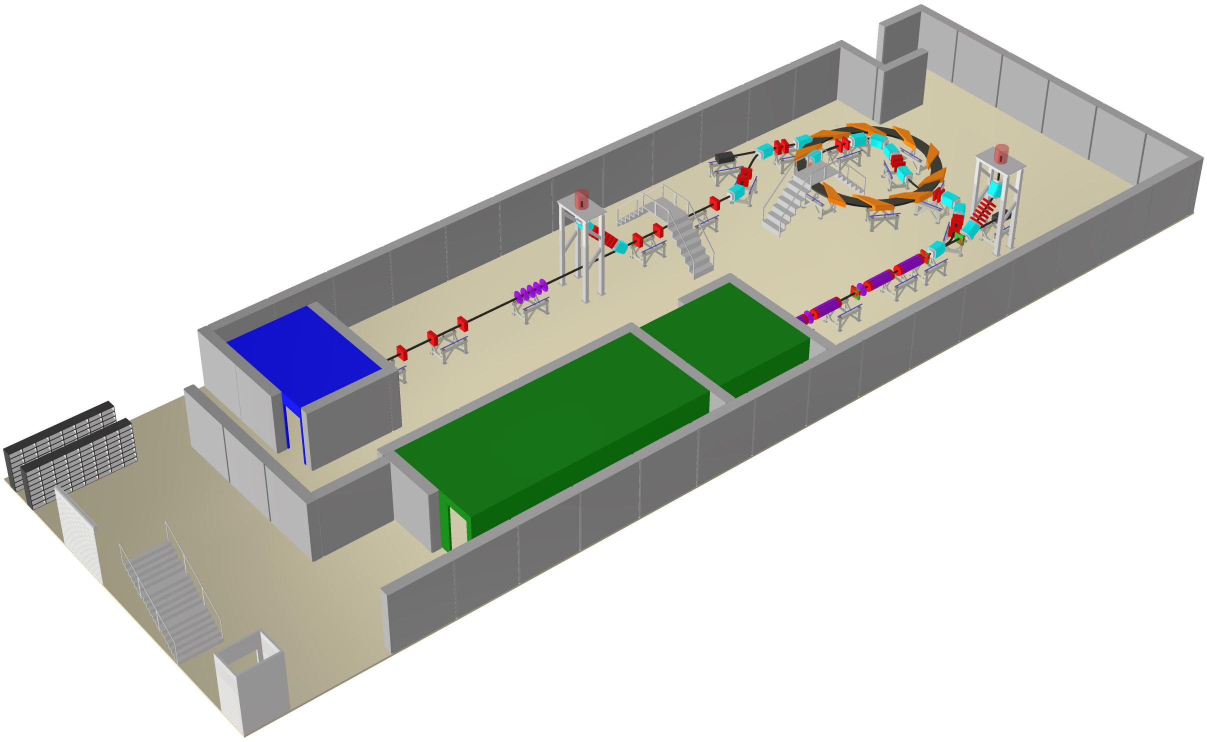

Figure 51: Isometric view of the accelerator level.

other beam configurations that may be of interest, such as micro beams, and the possibility of delivering such beams with LhARA will be investigated in the R&D programme.

3 Infrastructure and integration

3.1 Facility layout

The LhARA facility will encompass two floors of roughly 52 m length and 18 m width. The ground floor will contain the laser, accelerator, in-vivo end station and required support equipment and facilities, see figures 51 and 52. The first floor will house the laboratory area and the two in-vitro end stations, see Figure 53. The location of this facility is expected to be at an STFC National Laboratory or equivalent research institute. Depending on the available locations, an existing building or a new construction will be used.

The entire facility will require radiation protection in the form of concrete shielding, which will delineate the facility into three principal areas: a radiation controlled access area, a laser controlled access area, and a laboratory limited access area. The radiation controlled access area will contain the laser target (not including the laser source), Stage 1 and Stage 2 of the accelerator and all end stations. The laser controlled access area will contain only the laser source. Both controlled access areas will restrict machine operation while being accessed. The laboratory limited access area will contain all laboratory facilities and will not restrict machine operation while in use. Access to the radiation controlled areas is provided through interlocked labyrinth passages for personnel access and a removable interlocked shielding wall for equipment installation. The end stations include beam housings around the irradiation areas, which provides additional shielding to lower the background radiation during experimentation.

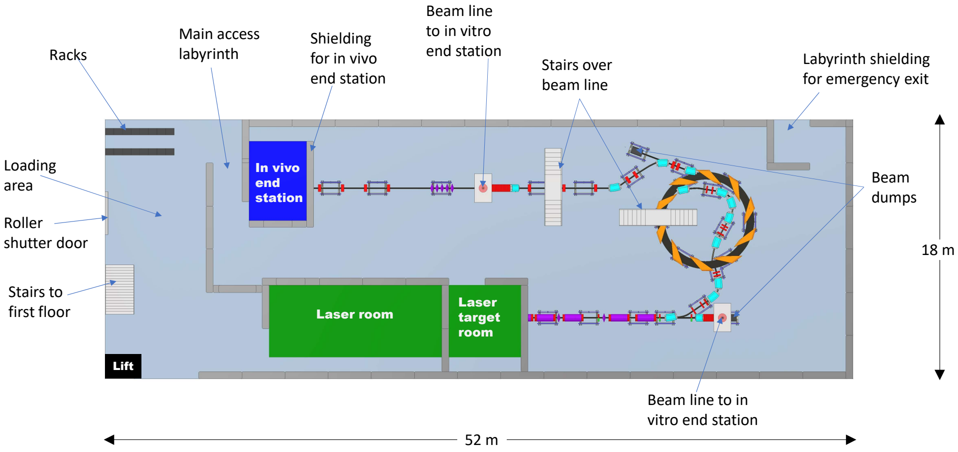

Figure 52: Top-down view of the floor layout of the accelerator level.

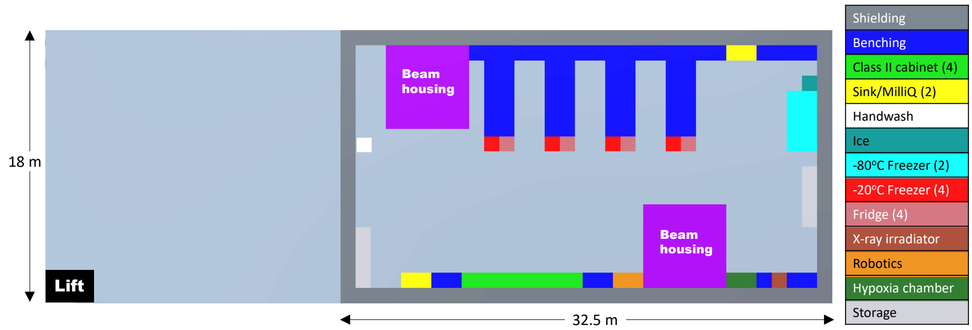

Figure 53: Top-down view of the floor layout of the in-vitro end stations level.

3.1.1 Laser rooms

The laser will occupy two rooms: a 12 m by 5 m room housing the laser system and a 5 m by 5 m room housing the laser target. There will be a shuttered pass-through between the rooms.

3.1.2 Stage 1 and Stage 2 accelerator

The ground floor will contain both Stage 1 and Stage 2 of the accelerator and encompasses approximately 24 m by 18 m. It contains floor space for manipulation and maintenance of equipment. Bridges are provided for access to the edges of the accelerator and inside the FFA ring.

3.1.3 End stations

There will be three end stations: two in-vitro and one in-vivo. The first in-vitro station is placed at the end of Stage 1 of the accelerator and is accessed via the first-floor laboratory. The second in-vitro station is placed at the extraction point of the FFA ring in Stage 2 of the accelerator and is accessed via the first-floor laboratory. The in-vivo station is placed at the end of Stage 2 and is accessed via the ground floor.

3.1.4 Support equipment

Initial provisions have been made in the layout for the location of support equipment, such as power supplies and control systems. They are to be located outside of the radiation controlled access area due to the sensitivity of the electronic equipment. Space will also be made available for plant systems, such as water, electrical and air handling.

3.2 Safety

It is assumed that LhARA will be built at an STFC National Laboratory or equivalent research institute which has an established safety-management system and culture in place. At STFC a comprehensive set of Safety Codes has been developed to cover the hazards associated with working in such an environment. STFC Safety Codes applicable to the construction and operation of LhARA include:

- SC6 – Risk management;
- SC13 – Construction (design and management);
- SC16 – Biological safety;
- SC22 – Working with lasers;
- SC23 – Working with time-varying electromagnetic fields;
- SC29 – Management of ionising radiation at work; and
- SC34 – Electrical safety.

In practice at STFC these codes are backed-up by the knowledge, skills and experience of staff and by appointed responsible persons such as Radiation Protection Advisors, Laser Responsible Officers, and Authorising Engineers. For a laser/accelerator facility such as LhARA adherence to these codes will typically involve a process of hazard identification, risk assessment and mitigation including (but not limited to) appropriate shielding, an independently verified and audited Personnel Protection System (PPS), a full commissioning plan, written operating instructions, training, and signage.

Although not strictly a safety system, consideration must also be given to a Machine Protection System (MPS) to ensure equipment is protected from damage caused by exceeding normal operating parameters.

3.2.1 Laser safety

STFC operates many high-power lasers and has lasers with operating parameters comparable to those for LhARA. In particular, Gemini [140] Target Area 2 operates at just below the energy conditions (0.5 J, 5 Hz, 30 fs) and Target Area 3 above (15 J, 0.3 Hz, 30 fs). Though lower repetition rates, the safety considerations on these facilities are the same and STFC is well equipped to mitigate and control the associated hazards and risks. Any challenges associated with the higher repetition rates (such as target debris and coating) are already being investigated as part of EPAC (Extreme Photonics and Applications Centre) [141] , a much higher energy 10 Hz laser facility.

3.2.2 Accelerator safety

The ISIS [142] [143] and ASTeC [144] departments in STFC have extensive experience in the operation of a variety of accelerator facilities and test stands. The most directly comparable to LhARA is the Front End Test Stand (FETS) [145] , which is currently undergoing commissioning at Rutherford Appleton Laboratory. The FETS operating parameters (H^- ions, 3 MeV, 60 mA, 2 ms, 50 Hz) exceed LhARA in beam power, but at lower energy. The safety considerations for FETS are therefore similar to those for LhARA, and this in combination with experience of running the much higher power ISIS Neutron and Muon Facility, gives confidence that STFC is well equipped to mitigate and control the expected accelerator hazards and risks for the LhARA facility.

3.2.3 End stations

Any administration of chemicals or drugs to the cells will be performed in Class II biological safety cabinets that are situated in the main research laboratory. If necessary, plates and dishes will be sealed prior to irradiation in the end-stations to avoid both exposure to the end-user and release to the surrounding environment.

Radiation protection in the end station will follow the same protocols as the rest of the accelerator ensuring adequate shielding and personnel protection.

3.2.4 Radiation

For a facility such as LhARA radiation safety is a primary concern. Regulation 8 of the Ionising Radiations Regulations 2017 (IRR17) [146] requires STFC to undertake a radiation risk assessment before commencing a new work activity involving ionising radiation. A radiation risk assessment will be considered suitable and sufficient if it addresses the requirements of paragraph 70 and 71 of the IRR17 Approved Code of Practice. Particular matters to be considered under paragraph 70 are the nature of the sources/hazard, radiation dose rates, likelihood and levels of contamination, relevant dosimetry, engineering controls and design features, planned systems of work, suitable PPE, access restriction arrangements, reasonably foreseeable accidents and incidents, consequences of failure of control measures and steps taken to prevent or limit the consequences of accidents. For paragraph 71 consideration must be given to actions to achieve ALARP, engineering control measures, PPE requirements, dose constraint requirements, measures for pregnant women and nursing mothers, investigation levels, maintenance and testing schedules for control measures, contingency plans, training, designation of areas, access restriction, classification of works, management responsibilities and performance monitoring.

3.3 R&D plan

The infrastructure and integration of the LhARA facility will require R&D in four key areas: risk analysis (project risks), risk assessments (safety risks), radiation simulations, and controls development.

Development of the risk analysis will cover all aspects of the facility, not just technical risks. Project management risks, such as funding and resource availability, must be considered fully to ensure timely delivery of a fully functioning facility. These risks will be scored based on an assigned impact and probability, controls will be put in place, and then the risks will be re-evaluated based on the effect of the controls, with the goal to minimise all risks to an acceptable level.

Using a similar methodology, a safety-risk assessment will be performed to describe and control all potential safety risks in the facility. The safety-risk assessment will, to a reasonable degree, identify all pieces of equipment that require safety mitigations and identify control measures to be put in place. The risks will be scored in the same way as the project risks, based on impact and probability. Control measures will be developed as needed, with the first choice will always be to avoid the risk; other solutions, such as engineering controls, signage, training, and PPE will be considered only after avoidance has been ruled out.

Coupled closely with the safety-risk assessment, there will be an additional effort to develop radiation simulations to characterise the radiation hazards in and around the LhARA facility. Current estimates of shielding have been made on best practice principles and in comparison to similar facilities, but a full analysis and simulation of the facility will allow the shielding to be optimised and the ensure its placement is correct.

The last area to require R&D will be the control systems. It is expected that the facility will use the Experimental Physics and Industrial Control System (EPICS). The logic and organisation of this system can begin to be developed during the R&D phase, which will enable the accelerator design to progress with a full understanding of what types of controls and instrumentation will be possible.

References

[1] T. W. H. Organisation, “Cancer,”. `https://www.who.int/news-room/fact-sheets/detail/cancer`.

[2] F. Bray, J. Ferlay, I. Soerjomataram, R. L. Siegel, L. A. Torre, and A. Jemal, “Global cancer statistics 2018: GLOBOCAN estimates of incidence and mortality worldwide for 36 cancers in 185 countries,” *CA: A Cancer Journal for Clinicians* **68** (nov, 2018) 394–424.

[3] C. Fitzmaurice, T. F. Akinyemiju, F. H. Al Lami, T. Alam, R. Alizadeh-Navaei, C. Allen, U. Alsharif, N. Alvis-Guzman, E. Amini, B. O. Anderson, O. Aremu, A. Artaman, S. W. Asgedom, R. Assadi, T. M. Atey, L. Avila-Burgos, A. Awasthi, H. O. Ba Saleem, A. Barac, J. R. Bennett, I. M. Bensenor, N. Bhakta, H. Brenner, L. Cahuana-Hurtado, C. A. Castañeda-Orjuela, F. Catalá-López, J.-Y. J. Choi, D. J. Christopher, S.-C. Chung, M. P. Curado, L. Dandona, R. Dandona, J. das Neves, S. Dey, S. D. Dharmaratne, D. T. Doku, T. R. Driscoll, M. Dubey, H. Ebrahimi, D. Edessa, Z. El-Khatib, A. Y. Endries, F. Fischer, L. M. Force, K. J. Foreman, S. W. Gebrehiwot, S. V. Gopalani, G. Grosso, R. Gupta, B. Gyawali, R. R. Hamadeh, S. Hamidi, J. Harvey, H. Y. Hassen, R. J. Hay, S. I. Hay, B. Heibati, M. K. Hiluf, N. Horita, H. D. Hosgood, O. S. Ilesanmi, K. Innos, F. Islami, M. B. Jakovljevic, S. C. Johnson, J. B. Jonas, A. Kasaeian, T. D. Kassa, Y. S. Khader, E. A. Khan, G. Khan, Y.-H. Khang, M. H. Khosravi, J. Khubchandani, J. A. Kopec, G. A. Kumar, M. Kutz, D. P. Lad, A. Lafranconi, Q. Lan, Y. Legesse, J. Leigh, S. Linn, R. Lunevicius, A. Majeed, R. Malekzadeh, D. C. Malta, L. G. Mantovani, B. J. McMahon, T. Meier, Y. A. Melaku, M. Melku, P. Memiah, W. Mendoza, T. J. Meretoja, H. B. Mezgebe, T. R. Miller, S. Mohammed, A. H. Mokdad, M. Moosazadeh, P. Moraga, S. M. Mousavi, V. Nangia, C. T. Nguyen, V. M. Nong, F. A. Ogbo, A. T. Olagunju, M. PA, E.-K. Park, T. Patel, D. M. Pereira, F. Pishgar, M. J. Postma, F. Pourmalek, M. Qorbani, A. Rafay, S. Rawaf, D. L. Rawaf, G. Roshandel, S. Safiri, H. Salimzadeh, J. R. Sanabria, M. M. Santric Milicevic, B. Sartorius, M. Satpathy, S. G. Sepanlou, K. A. Shackelford, M. A. Shaikh, M. Sharif-Alhoseini, J. She, M.-J. Shin, I. Shiue, M. G. Shrime, A. H. Sinke, M. Sisay, A. Sligar, M. B. Sufiyan, B. L. Sykes, R. Tabarés-Seisdedos, G. A. Tessema, R. Topor-Madry, T. T. Tran, B. X. Tran, K. N. Ukwaja, V. V. Vlassov, S. E. Vollset, E. Weiderpass, H. C. Williams, N. B. Yimer, N. Yonemoto, M. Z. Younis, C. J. L. Murray, M. Naghavi, and M. Naghavi, “Global, Regional, and National Cancer Incidence, Mortality, Years of Life Lost, Years Lived With Disability, and Disability-Adjusted Life-Years for 29 Cancer Groups, 1990 to 2016,” *JAMA Oncology* **4** (nov, 2018) 1553.

[4] R. Atun, D. A. Jaffray, M. B. Barton, F. Bray, M. Baumann, B. Vikram, T. P. Hanna, F. M. Knaul, Y. Lievens, T. Y. M. Lui, M. Milosevic, B. O’Sullivan, D. L. Rodin, E. Rosenblatt, J. V. Dyk, M. L. Yap, E. Zubizarreta, and M. Gospodarowicz, “Expanding global access to radiotherapy,” *The Lancet Oncology* **16** (2015), no. 10, 1153 – 1186.

[5] N. R. Datta, S. Rogers, and S. Bodis, “Challenges and Opportunities to Realize “The 2030 Agenda for Sustainable Development” by the United Nations: Implications for Radiation Therapy Infrastructure in Low- and Middle-Income Countries,” *International Journal of Radiation Oncology*Biology*Physics* **105** (2019), no. 5, 918–933.

[6] “Particle Therapy Co-Operative Group.” `https://www.ptcog.ch/index.php/patient-statistics`.

[7] V. Favaudon, L. Caplier, V. Monceau, F. Pouzoulet, M. Sayarath, C. Fouillade, M.-F. Poupon, I. Brito, P. Hupé, J. Bourhis, J. Hall, J.-J. Fontaine, and M.-C. Vozenin, “Ultrahigh dose-rate FLASH irradiation

increases the differential response between normal and tumor tissue in mice," *Science Translational Medicine* **6** (2014), no. 245, 245ra93–245ra93.

[8] M. C. Vozenin, P. De Fornel, K. Petersson, V. Favaudon, M. Jaccard, J. F. Germond, B. Petit, M. Burki, G. Ferrand, D. Patin, H. Bouchaab, M. Ozsahin, F. Bochud, C. Bailat, P. Devauchelle, and J. Bourhis, "The Advantage of FLASH Radiotherapy Confirmed in Mini–pig and Cat–cancer Patients," *Clin. Cancer Res.* **25** (Jan, 2019) 35–42.

[9] Y. Prezado, G. Jouvion, D. Hardy, A. Patriarca, C. Nauraye, J. Bergs, W. González, C. Guardiola, M. Juchaux, D. Labiod, R. Dendale, L. Jourdain, C. Sebrie, and F. Pouzoulet, "Proton minibeam radiation therapy spares normal rat brain: Long-Term Clinical, Radiological and Histopathological Analysis," *Scientific Reports* **7** (2017), no. 1, 14403.

[10] A. Lühr, C. von Neubeck, J. Pawelke, A. Seidlitz, C. Peitzsch, S. M. Bentzen, T. Bortfeld, J. Debus, E. Deutsch, J. A. Langendijk, J. S. Loeffler, R. Mohan, M. Scholz, B. S. Sørensen, D. C. Weber, M. Baumann, and M. Krause, " "Radiobiology of Proton Therapy": Results of an international expert workshop," *Radiotherapy and Oncology* (Jul, 2018) 56–67.

[11] J. Bin, K. Allinger, W. Assmann, G. Dollinger, G. A. Drexler, A. A. Friedl, D. Habs, P. Hilz, R. Hoerlein, N. Humble, S. Karsch, K. Khrennikov, D. Kiefer, F. Krausz, W. Ma, D. Michalski, M. Molls, S. Raith, S. Reinhardt, B. Röper, T. E. Schmid, T. Tajima, J. Wenz, O. Zlobinskaya, J. Schreiber, and J. J. Wilkens, "A laser-driven nanosecond proton source for radiobiological studies," *Applied Physics Letters* **101** (2012), no. 24, 243701.

[12] M. Durante, "Biophysics Department GSI/FAIR," in *Int. Biophysics Collaboration meeting*. Rome, 20 February, 2020.

[13] M. Durante, P. Indelicato, B. Jonson, V. Koch, K. Langanke, U.-G. Meißner, E. Nappi, T. Nilsson, T. Stöhlker, E. Widmann, and M. Wiescher, "All the fun of the FAIR: fundamental physics at the facility for antiproton and ion research," *Physica Scripta* **94** (Jan, 2019) 033001.

[14] S. Brandenburg, L. Barazzuol, S. Both, R. Coppes, M. van Goethem, B. Jones, and P. van Luijk, "Biomedical research capabilities at KVI-CART," in *Int. Biophysics Collaboration meeting*. Rome, 20 February, 2020.

[15] A. Navin, "GANIL and Int. Biophys. Collab.," in *Int. Biophysics Collaboration meeting*. Rome, 20 February, 2020.

[16] F. Durantel, E. Balanzat, A. Cassimi, F. Chevalier, Y. Ngono-Ravache, T. Madi, J.-C. Poully, J.-M. Ramillon, H. Rothard, F. Ropars, L. Schwob, I. Testard, and Y. Saintigny, "Dosimetry for radiobiology experiments at GANIL," *Nuclear Instruments and Methods in Physics Research Section A: Accelerators, Spectrometers, Detectors and Associated Equipment* **816** (2016) 70 – 77.

[17] C. Vandevoorde, "Nuclear applied physics and biophysics at iThemba LABS," in *Int. Biophysics Collaboration meeting*. Rome, 20 February, 2020.

[18] J. Conradie, P. Celliers, J. Crafford, J. Delsink, J. De Villiers, H. du Plessis, R. Fenemore, D. Fourie, Z. Kormany, Y. Manjoo, *et al.*, "Cyclotrons at iThemba LABS," in *Cyclotrons and their Applications Conf.* 2004.

[19] G. Cuttone, "LNS BioPhysics Facility," in *Int. Biophysics Collaboration meeting*. Rome, 20 February, 2020.

[20] L. Calabretta, A. Calanna, G. Cuttone, G. D'Agostino, D. Rifuggiato, and A. Domenico Russo, "Overview of the future upgrade of the INFN-LNS superconducting cyclotron," *Modern Physics Letters A* **32** (2017), no. 17, 1740009, `https://doi.org/10.1142/S0217732317400090`.

[21] L. Giuffrida and D. Margarone, "Nuclear Applied Physics and Biophysics at ELI-Beamlines," in *Int. Biophysics Collaboration meeting*. Rome, 20 February, 2020.

[22] S. Rossi and M. Pullia, "Nuclear Applied Physics and Biophysics at CNAO," in *Int. Biophysics Collaboration meeting*. Rome, 20 February, 2020.

[23] A. Facoetti, B. Vischioni, M. Ciocca, M. Ferrarini, Y. Furusawa, A. Mairani, Y. Matsumoto, A. Mirandola, S. Molinelli, A. Uzawa, F. G. Vilches, and R. Orecchia, "In vivo radiobiological assessment of the new clinical carbon ion beams at CNAO," *Radiation Protection Dosimetry* **166** (04, 2015) 379–382.

[24] T. Inaniwa, "Nuclear Applied Physics and Biophysics at HIMAC," in *Int. Biophysics Collaboration meeting*. Rome, 20 February, 2020.

[25] D. Bettoni, "Nuclear Applied Physics and Biophysics at SPES," in *Int. Biophysics Collaboration meeting*. Rome, 20 February, 2020.

[26] G. de Angelis *et al.*, "The SPES radioactive ion beam project of LNL: status and perspectives," *EPJ Web of Conferences* **107** (2016) 01001.

[27] A. Bugay and E. Nasanova, "Nuclear Applied Physics and Biophysics at NICA," in *Int. Biophysics Collaboration meeting*. Rome, 20 February, 2020.

[28] E. Syresin *et al.*, "Nuclotron New Beam Channels for Applied Researches," in *Proceedings, 8th International Particle Accelerator Conference (IPAC 2017): Copenhagen, Denmark, May 14-19, 2017*, p. TUPVA114. 2017.

[29] G. Battistoni, "Nuclear Applied Physics and Biophysics at TIFPA-INFN," in *Int. Biophysics Collaboration meeting*. Rome, 20 February, 2020.

[30] F. Tommasino, M. Rovituso, E. Bortoli, C. L. Tessa, G. Petringa, S. Lorentini, E. Verroi, Y. Simeonov, U. Weber, P. Cirrone, M. Schwarz, M. Durante, and E. Scifoni, "A new facility for proton radiobiology at the Trento proton therapy centre: Design and implementation," *Physica Medica* **58** (2019) 99 – 106.

[31] Cancer Research UK, "Worldwide cancer incidence statistics." `https://www.cancerresearchuk.org/health-professional/cancer-statistics/worldwide-cancer/incidence`, Nov, 2018. Accessed: 2019-04-13.

[32] J. S. Loeffler and M. Durante, "Charged particle therapy—optimization, challenges and future directions," *Nature Reviews Clinical Oncology* **10** (2013), no. 7, 411–424.

[33] H. Paganetti and P. van Luijk, "Biological Considerations When Comparing Proton Therapy With Photon Therapy," *Seminars in Radiation Oncology* **23** (2013), no. 2, 77 – 87. Controversies in Proton Therapy.

[34] H. Paganetti, "Relative biological effectiveness (RBE) values for proton beam therapy. Variations as a function of biological endpoint, dose, and linear energy transfer," *Phys. Med. Biol.* **59** (2014), no. 22, R419.

[35] B. Jones, S. J. McMahon, and K. M. Prise, “The Radiobiology of Proton Therapy: Challenges and Opportunities Around Relative Biological Effectiveness,” *Clinical Oncology* **30** (2018), no. 5, 285–292.

[36] G. Giovannini, T. Böhlen, G. Cabal, J. Bauer, T. Tessonnier, K. Frey, J. Debus, A. Mairani, and K. Parodi, “Variable RBE in proton therapy: comparison of different model predictions and their influence on clinical-like scenarios,” *Radiation Oncology* **11** (May, 2016) 68.

[37] A. Lühr, C. von Neubeck, M. Krause, and E. G. C. Troost, “Relative biological effectiveness in proton beam therapy – Current knowledge and future challenges,” *Clinical and Translational Radiation Oncology* **9** (2018) 35–41.

[38] P. Chaudhary, T. I. Marshall, F. M. Perozziello, L. Manti, F. J. Currell, F. Hanton, S. J. McMahon, J. N. Kavanagh, G. A. P. Cirrone, F. Romano, K. M. Prise, and G. Schettino, “Relative Biological Effectiveness Variation Along Monoenergetic and Modulated Bragg Peaks of a 62-MeV Therapeutic Proton Beam: A Preclinical Assessment,” *International Journal of Radiation Oncology • Biology • Physics* **90** (sep, 2014) 27–35.

[39] J. J. Wilkens and U. Oelfke, “A phenomenological model for the relative biological effectiveness in therapeutic proton beams,” *Physics in Medicine and Biology* **49** (jun, 2004) 2811–2825.

[40] C. P. Karger and P. Peschke, “RBE and related modeling in carbon-ion therapy,” *Physics in Medicine & Biology* **63** (dec, 2017) 01TR02.

[41] E. T. Vitti and J. L. Parsons, “The Radiobiological Effects of Proton Beam Therapy: Impact on DNA Damage and Repair,” *Cancers* **11** (2019), no. 7,.

[42] R. J. Carter, C. M. Nickson, J. M. Thompson, A. Kacperek, M. A. Hill, and J. L. Parsons, “Complex DNA Damage Induced by High Linear Energy Transfer Alpha-Particles and Protons Triggers a Specific Cellular DNA Damage Response,” *International Journal of Radiation Oncology*Biology*Physics* **100** (2018), no. 3, 776 – 784.

[43] E. T. Vitti and J. L. Parsons, “The Radiobiological Effects of Proton Beam Therapy: Impact on DNA Damage and Repair,” *Cancers* **11** (Jul, 2019) 946.

[44] V. M. Systems, “FlashForward Consortium,”. `https://www.varian.com/about-varian/research/flashforward-consortium`.

[45] S. Bulanov, T. Esirkepov, V. Khoroshkov, A. Kuznetsov, and F. Pegoraro, “Oncological hadrontherapy with laser ion accelerators,” *Physics Letters A* **299** (2002), no. 2, 240–247.

[46] E. Fourkal, J. S. Li, M. Ding, T. Tajima, and C. M. Ma, “Particle selection for laser-accelerated proton therapy feasibility study,” *Medical Physics* **30** (2003), no. 7, 1660–1670, `https://aapm.onlinelibrary.wiley.com/doi/pdf/10.1118/1.1586268`.

[47] V. Malka, S. Fritzler, E. Lefebvre, E. d’Humières, R. Ferrand, G. Grillon, C. Albaret, S. Meyroneinc, J.-P. Chambaret, A. Antonetti, and D. Hulin, “Practicability of proton therapy using compact laser systems,” *Medical Physics* **31** (2004), no. 6, 1587–1592, `https://aapm.onlinelibrary.wiley.com/doi/pdf/10.1118/1.1747751`.

[48] S. D. Kraft, C. Richter, K. Zeil, M. Baumann, E. Beyreuther, S. Bock, M. Bussmann, T. E. Cowan, Y. Dammene, W. Enghardt, U. Helbig, L. Karsch, T. Kluge, L. Laschinsky, E. Lessmann, J. Metzkes, D. Naumburger, R. Sauerbrey, M. Schürer, M. Sobiella, J. Woithe, U. Schramm, and J. Pawelke,

"Dose–dependent biological damage of tumour cells by laser–accelerated proton beams," *New Journal of Physics* **12** (aug, 2010) 085003.

[49] F. Fiorini, D. Kirby, M. Borghesi, D. Doria, J. C. Jeynes, K. F. Kakolee, S. Kar, S. Kaur, K. J. Kirby, M. J. Merchant, and S. Green, "Dosimetry and spectral analysis of a radiobiological experiment using laser-driven proton beams," *Phys Med Biol* **56** (Nov, 2011) 6969–6982.

[50] D. Doria, K. F. Kakolee, S. Kar, S. K. Litt, F. Fiorini, H. Ahmed, S. Green, J. C. G. Jeynes, J. Kavanagh, D. Kirby, K. J. Kirkby, C. L. Lewis, M. J. Merchant, G. Nersisyan, R. Prasad, K. M. Prise, G. Schettino, M. Zepf, and M. Borghesi, "Biological effectiveness on live cells of laser driven protons at dose rates exceeding 10^9 Gy/s," *AIP Advances* **2** (2012), no. 1, 011209, `https://doi.org/10.1063/1.3699063`.

[51] K. Zeil, M. Baumann, E. Beyreuther, T. Burris-Mog, T. E. Cowan, W. Enghardt, L. Karsch, S. D. Kraft, L. Laschinsky, J. Metzkes, D. Naumburger, M. Oppelt, C. Richter, R. Sauerbrey, M. Schürer, U. Schramm, and J. Pawelke, "Dose–controlled irradiation of cancer cells with laser-accelerated proton pulses," *Applied Physics B* **110** (2013), no. 4, 437–444.

[52] U. Masood, M. Bussmann, T. E. Cowan, W. Enghardt, L. Karsch, F. Kroll, U. Schramm, and J. Pawelke, "A compact solution for ion beam therapy with laser accelerated protons," *Applied Physics B* **117** (2014), no. 1, 41–52.

[53] O. Zlobinskaya, C. Siebenwirth, C. Greubel, V. Hable, R. Hertenberger, N. Humble, S. Reinhardt, D. Michalski, B. Röper, G. Multhoff, G. Dollinger, J. J. Wilkens, and T. E. Schmid, "The Effects of Ultra–High Dose Rate Proton Irradiation on Growth Delay in the Treatment of Human Tumor Xenografts in Nude Mice," *Radiation Research* **181** (2014), no. 2, 177–183.

[54] "A-SAIL Project." `https://www.qub.ac.uk/research-centres/A-SAILProject/`.

[55] G. A. P. Cirrone, D. Margarone, M. Maggiore, A. Anzalone, M. Borghesi, S. B. Jia, S. S. Bulanov, S. Bulanov, M. Carpinelli, S. Cavallaro, M. Cutroneo, G. Cuttone, M. Favetta, S. Gammino, O. Klimo, L. Manti, G. Korn, G. L. Malfa, J. Limpouch, A. Musumarra, I. Petrovic, J. Prokupek, J. Psikal, A. Ristic-Fira, M. Renis, F. P. Romano, F. Romano, G. Schettino, F. Schillaci, V. Scuderi, C. Stancampiano, A. Tramontana, S. Ter-Avetisyan, B. Tomasello, L. Torrisi, S. Tudisco, and A. Velyhan, "ELIMED: a new hadron therapy concept based on laser driven ion beams," in *Laser Acceleration of Electrons, Protons, and Ions II; and Medical Applications of Laser-Generated Beams of Particles II; and Harnessing Relativistic Plasma Waves III*, E. Esarey, C. B. Schroeder, W. P. Leemans, K. W. D. Ledingham, and D. A. Jaroszynski, eds., vol. 8779, pp. 216 – 225, International Society for Optics and Photonics. SPIE, 2013.

[56] S. M. Wiggins, M. Boyd, E. Brunetti, N. M. H. Butler, J. S. Feehan, R. J. Gray, B. Hidding, D. G. Ireland, W. Li, A. Maitrallain, G. G. Manahan, P. McKenna, D. O'Donnell, M. Scheck, M. Shahzad, Z.-M. Sheng, R. Spesyvtsev, G. Vieux, D. P. Watts, G. H. Welsh, R. Wilson, N. Zachariou, and D. A. Jaroszynski, "Application programmes at the Scottish Centre for the Application of Plasma-based Accelerators (SCAPA)," in *Relativistic Plasma Waves and Particle Beams as Coherent and Incoherent Radiation Sources III*, D. A. Jaroszynski and M. Hur, eds., vol. 11036, pp. 93 – 103, International Society for Optics and Photonics. SPIE, 2019.

[57] L. Manti, F. Perozziello, M. Borghesi, G. Candiano, P. Chaudhary, G. Cirrone, D. Doria, D. Gwynne, R. Leanza, K. M. Prise, L. Romagnani, F. Romano, V. Scuderi, and A. Tramontana, "The radiobiology

of laser-driven particle beams: focus on sub-lethal responses of normal human cells," *Journal of Instrumentation* **12** (mar, 2017) C03084–C03084.

[58] F. Romano, F. Schillaci, G. Cirrone, G. Cuttone, V. Scuderi, L. Allegra, A. Amato, A. Amico, G. Candiano, G. D. Luca, G. Gallo, S. Giordanengo, L. F. Guarachi, G. Korn, G. Larosa, R. Leanza, R. Manna, V. Marchese, F. Marchetto, D. Margarone, G. Milluzzo, G. Petringa, J. Pipek, S. Pulvirenti, D. Rizzo, R. Sacchi, S. Salamone, M. Sedita, and A. Vignati, "The ELIMED transport and dosimetry beamline for laser-driven ion beams," *Nuclear Instruments and Methods in Physics Research Section A: Accelerators, Spectrometers, Detectors and Associated Equipment* **829** (2016) 153–158. 2nd European Advanced Accelerator Concepts Workshop – EAAC 2015.

[59] U. Masood, T. E. Cowan, W. Enghardt, K. M. Hofmann, L. Karsch, F. Kroll, U. Schramm, J. J. Wilkens, and J. Pawelke, "A light-weight compact proton gantry design with a novel dose delivery system for broad-energetic laser-accelerated beams," *Physics in Medicine & Biology* **62** (jun, 2017) 5531–5555.

[60] P. Chaudhary, D. Gwynne, D. Doria, L. Romagnani, C. Maiorino, H. Padda, A. Alejo, N. Booth, D. Carroll, S. Kar, P. McKenna, G. Schettino, M. Borghesi, and K. M. Prise, "Effectiveness of laser accelerated ultra high dose rate protons in DNA DSB damage induction under hypoxic conditions," in *44th EPS Conference on Plasma Physics, EPS 2017*, vol. 44F, p. P1.217. European Physical Society (EPS), January, 2017.

[61] D. Margarone, G. A. P. Cirrone, G. Cuttone, A. Amico, L. Andò, M. Borghesi, S. S. Bulanov, S. V. Bulanov, D. Chatain, A. Fajstavr, L. Giuffrida, F. Grepl, S. Kar, J. Krasa, D. Kramer, G. Larosa, R. Leanza, T. Levato, M. Maggiore, L. Manti, G. Milluzzo, B. Odlozilik, V. Olsovcova, J.-P. Perin, J. Pipek, J. Psikal, G. Petringa, J. Ridky, F. Romano, B. Rus, A. Russo, F. Schillaci, V. Scuderi, A. Velyhan, R. Versaci, T. Wiste, M. Zakova, and G. Korn, "ELIMAIA: A Laser–Driven Ion Accelerator for Multidisciplinary Applications," *Quantum Beam Science* **2** (2018), no. 2,.

[62] S. D. Kraft, C. Richter, K. Zeil, M. Baumann, E. Beyreuther, S. Bock, M. Bussmann, T. E. Cowan, Y. Dammene, W. Enghardt, U. Helbig, L. Karsch, T. Kluge, L. Laschinsky, E. Lessmann, J. Metzkes, D. Naumburger, R. Sauerbrey, M. Schürer, M. Sobiella, J. Woithe, U. Schramm, and J. Pawelke, "Dose-dependent biological damage of tumour cells by laser-accelerated proton beams," *New Journal of Physics* **12** (aug, 2010) 85003.

[63] A. Yogo, T. Maeda, T. Hori, H. Sakaki, K. Ogura, M. Nishiuchi, A. Sagisaka, H. Kiriyama, H. Okada, S. Kanazawa, T. Shimomura, Y. Nakai, M. Tanoue, F. Sasao, P. R. Bolton, M. Murakami, T. Nomura, S. Kawanishi, and K. Kondo, "Measurement of relative biological effectiveness of protons in human cancer cells using a laser-driven quasimonoenergetic proton beamline," *Applied Physics Letters* **98** (2011), no. 5, 053701.

[64] J. Bin, K. Allinger, W. Assmann, G. Dollinger, G. A. Drexler, A. A. Friedl, D. Habs, P. Hilz, R. Hoerlein, N. Humble, S. Karsch, K. Khrennikov, D. Kiefer, F. Krausz, W. Ma, D. Michalski, M. Molls, S. Raith, S. Reinhardt, B. Röper, T. E. Schmid, T. Tajima, J. Wenz, O. Zlobinskaya, J. Schreiber, and J. J. Wilkens, "A laser-driven nanosecond proton source for radiobiological studies," *Applied Physics Letters* **101** (2012), no. 24, 243701.

[65] D. Doria, K. F. Kakolee, S. Kar, S. K. Litt, F. Fiorini, H. Ahmed, S. Green, J. C. G. Jeynes, J. Kavanagh, D. Kirby, K. J. Kirkby, C. L. Lewis, M. J. Merchant, G. Nersisyan, R. Prasad, K. M. Prise, G. Schettino, M. Zepf, and M. Borghesi, "Biological effectiveness on live cells of laser driven protons at dose rates exceeding $109 Gy/s$," *AIP Advances* **2** (2012), no. 1, 011209.

[66] K. Zeil, M. Baumann, E. Beyreuther, T. Burris-Mog, T. E. Cowan, W. Enghardt, L. Karsch, S. D. Kraft, L. Laschinsky, J. Metzkes, D. Naumburger, M. Oppelt, C. Richter, R. Sauerbrey, M. Schürer, U. Schramm, and J. Pawelke, "Dose-controlled irradiation of cancer cells with laser-accelerated proton pulses," *Applied Physics B* **110** (2013), no. 4, 437–444.

[67] L. Pommarel, B. Vauzour, F. Mégnin-Chanet, E. Bayart, O. Delmas, F. Goudjil, C. Nauraye, V. Letellier, F. Pouzoulet, F. Schillaci, F. Romano, V. Scuderi, G. A. Cirrone, E. Deutsch, A. Flacco, and V. Malka, "Spectral and spatial shaping of a laser-produced ion beam for radiation-biology experiments," *Physical Review Accelerators and Beams* **20** (2017), no. 3, 1–10.

[68] L. Manti, F. M. Perozziello, M. Borghesi, G. Candiano, P. Chaudhary, G. A. Cirrone, D. Doria, D. Gwynne, R. Leanza, K. M. Prise, L. Romagnani, F. Romano, V. Scuderi, and A. Tramontana, "The radiobiology of laser-driven particle beams: Focus on sub-lethal responses of normal human cells," *Journal of Instrumentation* **12** (2017), no. 3,.

[69] F. Osmic, M. Feurstein, A. Gyorgy, A. Kerschbaum, M. Repovz, S. Schwarz, W. Neustadt, and G. Burtin, "Overview of the Beam diagnostics in the Medaustron Accelerator:Design choices and test Beam commissioning," *Conf. Proc.* **C1205201** (May, 2012) MOPPR002. 3 p.

[70] E. L. Clark, K. Krushelnick, J. R. Davies, M. Zepf, M. Tatarakis, F. N. Beg, A. Machacek, P. A. Norreys, M. I. K. Santala, I. Watts, and A. E. Dangor, "Measurements of Energetic Proton Transport through Magnetized Plasma from Intense Laser Interactions with Solids," *Phys. Rev. Lett.* **84** (Jan, 2000) 670–673.

[71] R. A. Snavely, M. H. Key, S. P. Hatchett, T. E. Cowan, M. Roth, T. W. Phillips, M. A. Stoyer, E. A. Henry, T. C. Sangster, M. S. Singh, S. C. Wilks, A. MacKinnon, A. Offenberger, D. M. Pennington, K. Yasuike, A. B. Langdon, B. F. Lasinski, J. Johnson, M. D. Perry, and E. M. Campbell, "Intense High-Energy Proton Beams from Petawatt-Laser Irradiation of Solids," *Phys. Rev. Lett.* **85** (Oct, 2000) 2945–2948.

[72] H. Daido, M. Nishiuchi, and A. S. Pirozhkov, "Review of laser-driven ion sources and their applications," *Reports on Progress in Physics* **75** (apr, 2012) 56401.

[73] C. Scullion, D. Doria, L. Romagnani, A. Sgattoni, K. Naughton, D. R. Symes, P. McKenna, A. MacChi, M. Zepf, S. Kar, and M. Borghesi, "Polarization Dependence of Bulk Ion Acceleration from Ultrathin Foils Irradiated by High-Intensity Ultrashort Laser Pulses," *Physical Review Letters* **119** (2017), no. 5, 1–6.

[74] D. Margarone, A. Velyhan, J. Dostal, J. Ullschmied, J. P. Perin, D. Chatain, S. Garcia, P. Bonnay, T. Pisarczyk, R. Dudzak, M. Rosinski, J. Krasa, L. Giuffrida, J. Prokupek, V. Scuderi, J. Psikal, M. Kucharik, M. De Marco, J. Cikhardt, E. Krousky, Z. Kalinowska, T. Chodukowski, G. A. P. Cirrone, and G. Korn, "Proton Acceleration Driven by a Nanosecond Laser from a Cryogenic Thin Solid-Hydrogen Ribbon," *Phys. Rev. X* **6** (Nov, 2016) 041030.

[75] M. Gauthier, C. B. Curry, S. Göde, F.-E. Brack, J. B. Kim, M. J. MacDonald, J. Metzkes, L. Obst, M. Rehwald, C. Rödel, H.-P. Schlenvoigt, W. Schumaker, U. Schramm, K. Zeil, and S. H. Glenzer, "High repetition rate, multi-MeV proton source from cryogenic hydrogen jets," *Applied Physics Letters* **111** (2017), no. 11, 114102, `https://doi.org/10.1063/1.4990487`.

[76] L. Obst, S. Göde, M. Rehwald, F.-E. Brack, J. Branco, S. Bock, M. Bussmann, T. E. Cowan, C. B. Curry, F. Fiuza, M. Gauthier, R. Gebhardt, U. Helbig, A. Huebl, U. Hübner, A. Irman, L. Kazak, J. B.

Kim, T. Kluge, S. Kraft, M. Loeser, J. Metzkes, R. Mishra, C. Rödel, H.-P. Schlenvoigt, M. Siebold, J. Tiggesbäumker, S. Wolter, T. Ziegler, U. Schramm, S. H. Glenzer, and K. Zeil, "Efficient laser-driven proton acceleration from cylindrical and planar cryogenic hydrogen jets," *Scientific Reports* **7** (2017), no. 1, 10248.

[77] J. T. Morrison, S. Feister, K. D. Frische, D. R. Austin, G. K. Ngirmang, N. R. Murphy, C. Orban, E. A. Chowdhury, and W. M. Roquemore, "MeV proton acceleration at kHz repetition rate from ultra-intense laser liquid interaction," *New Journal of Physics* **20** (feb, 2018) 22001.

[78] M. Noaman-ul Haq, H. Ahmed, T. Sokollik, L. Yu, Z. Liu, X. Yuan, F. Yuan, M. Mirzaie, X. Ge, L. Chen, and J. Zhang, "Statistical analysis of laser driven protons using a high-repetition-rate tape drive target system," *Phys. Rev. Accel. Beams* **20** (Apr, 2017) 041301.

[79] B. Aurand, S. Grieser, T. Toncian, E. Aktan, M. Cerchez, L. Lessmann, R. Prasad, A. Khoukaz, and O. Willi, "A multihertz, kiloelectronvolt pulsed proton source from a laser irradiated continuous hydrogen cluster target," *Physics of Plasmas* **26** (2019), no. 7, 073102.

[80] M. J. V. Streeter, S. J. D. Dann, J. D. E. Scott, C. D. Baird, C. D. Murphy, S. Eardley, R. A. Smith, S. Rozario, J.-N. Gruse, S. P. D. Mangles, *et al.*, "Temporal feedback control of high-intensity laser pulses to optimize ultrafast heating of atomic clusters," *Applied Physics Letters* **112** (Jun, 2018) 244101.

[81] S. J. D. Dann, C. D. Baird, N. Bourgeois, O. Chekhlov, S. Eardley, C. D. Gregory, J.-N. Gruse, J. Hah, D. Hazra, S. J. Hawkes, C. J. Hooker, K. Krushelnick, S. P. D. Mangles, V. A. Marshall, C. D. Murphy, Z. Najmudin, J. A. Nees, J. Osterhoff, B. Parry, P. Pourmoussavi, S. V. Rahul, P. P. Rajeev, S. Rozario, J. D. E. Scott, R. A. Smith, E. Springate, Y. Tang, S. Tata, A. G. R. Thomas, C. Thornton, D. R. Symes, and M. J. V. Streeter, "Laser wakefield acceleration with active feedback at 5 Hz," *Phys. Rev. Accel. Beams* **22** (Apr, 2019) 041303.

[82] J. Kirschner, M. Mutný, N. Hiller, R. Ischebeck, and A. Krause, "Adaptive and Safe Bayesian Optimization in High Dimensions via One-Dimensional Subspaces," 2019.

[83] D. GABOR, "A Space-Charge Lens for the Focusing of Ion Beams," *Nature* **160** (1947), no. 4055, 89–90.

[84] J. Pozimski and M. Aslaninejad, "Gabor lenses for capture and energy selection of laser driven ion beams in cancer treatment," *Laser and Particle Beams* **31** (2013), no. 4, 723—-733.

[85] R. C. Thompson, "PENNING TRAPS," in *Trapped Charged Particles*, Advanced Textbooks in Physics, pp. 1–33. WORLD SCIENTIFIC (EUROPE), sep, 2015.

[86] J. S. deGrassie and J. H. Malmberg, "Waves and transport in the pure electron plasma," *The Physics of Fluids* **23** (1980), no. 1, 63–81.

[87] J. H. Malmberg, C. F. Driscoll, B. Beck, D. L. Eggleston, J. Fajans, K. Fine, X. P. Huang, and A. W. Hyatt, "Experiments with pure electron plasmas," *AIP Conference Proceedings* **175** (1988), no. 1, 28–74.

[88] D. L. Eggleston, "Confinement of test particles in a Malmberg–Penning trap with a biased axial wire," *Physics of Plasmas* **4** (1997), no. 5, 1196–1200.

[89] M. Amoretti, G. Bettega, F. Cavaliere, M. Cavenago, F. De Luca, R. Pozzoli, and M. Romé, "Cylindrical Penning trap for the study of electron plasmas," *Review of Scientific Instruments* **74** (2003), no. 9, 3991–3997.

[90] J. Fajans and A. Schmidt, "Malmberg–Penning and Minimum-B trap compatibility: the advantages of higher-order multipole traps," *Nuclear Instruments and Methods in Physics Research Section A: Accelerators, Spectrometers, Detectors and Associated Equipment* **521** (2004), no. 2, 318–325.

[91] A. W. Chao, K. H. Mess, M. Tigner, and F. Zimmermann, *Handbook of accelerator physics and engineering; 2nd ed.*, p. 185. World Scientific, Singapore, 2013.

[92] J. Pozimski and O. Meusel, "Space charge lenses for particle beams," *Review of Scientific Instruments* **76** (2005), no. 6, 063308.

[93] P. A. Posocco, M. Merchant, J. Pozimski, and Y. Xia, "First Test of The Imperial College Gabor (Plasma) Lens prototype at the Surrey Ion Beam centre," in *Proceedings, 7th International Particle Accelerator Conference (IPAC 2016): Busan, Korea, May 8-13, 2016*, p. TUPMY024. 2016.

[94] "VSim for Plasma." `https://www.txcorp.com/vsim`.

[95] "Computer Simulation Technology - Studio Suite." `https://www.3ds.com/products-services/simulia/products/cst-studio-suite/`.

[96] V. Belan, V. Butenko, B. Ivanov, V. Kiselev, A. Kitsenko, A. Linnik, I. Onishchenko, V. Prishchepov, and A. Yegorov, "Plasma lens with a current density depended on external magnetic field," *Problems of Atomic Science and Technology Series: Plasma Physics* **3,4** (1999), no. 3,4, 233–235.

[97] O. Meusel, M. Droba, B. Glaeser, and K. Schulte, "Experimental studies of stable confined electron clouds using Gabor lenses," in *Proceedings of Joint INFN-CERN-EuCARD-AccNet Workshop on Electron-Cloud Effects*, p. 286. European Organization for Nuclear Research (CERN), 2013.

[98] K. Schulte, M. Droba, O. Meusel, U. Ratzinger, A. Adonin, R. Berezov, R. Hollinger, and J. Pfister, "Gabor Lens Performance Studies at the GSI High Current Test Injector," in *Proceedings, 4th International Particle Accelerator Conference (IPAC): Shanghai, May 12-17*, p. THPWO021. 2013.

[99] B. Autin, C. Carli, T. D'Amico, O. Gröbner, M. Martini, and E. Wildner, "BeamOptics: A program for analytical beam optics," Tech. Rep. CERN–98-06, European Organization for Nuclear Research (CERN), 1998. `http://inis.iaea.org/search/search.aspx?orig_q=RN:30052986`.

[100] H. Grote and F. Schmidt, "MAD-X: An upgrade from MAD8," *Conf. Proc. C* **030512** (2003) 3497.

[101] L. J. Nevay *et al.*, "BDSIM: An accelerator tracking code with particle-matter interactions," *Computer Physics Communications* (2020) 107200.

[102] **GEANT4** Collaboration, S. Agostinelli *et al.*, "GEANT4: A Simulation toolkit," *Nucl. Instrum. Meth.* **A506** (2003) 250–303.

[103] I. Antcheva, M. Ballintijn, B. Bellenot, M. Biskup, R. Brun, N. Buncic, P. Canal, D. Casadei, O. Couet, V. Fine, L. Franco, G. Ganis, A. Gheata, D. G. Maline, M. Goto, J. Iwaszkiewicz, A. Kreshuk, D. M. Segura, R. Maunder, L. Moneta, A. Naumann, E. Offermann, V. Onuchin, S. Panacek, F. Rademakers, P. Russo, and M. Tadel, "ROOT — A C++ framework for petabyte data storage, statistical analysis and visualization," *Computer Physics Communications* **180** (2009), no. 12, 2499 – 2512.

[104] M. J. De Loos and S. B. Van der Geer, "General Particle Tracer: A New 3D Code for Accelerator and Beamline Design,".

[105] J. Pasternak *et al.*, "Design of LhARA - Laser Hybrid Accelerator For Radiobiological Applications," *Proceedings of IPAC2019* (2019).

[106] N. Tsoupas *et al.*, "Uniform Beam Distributions Using Octupoles," *Proceedings of PAC 1991* (1991) 1695–1697.

[107] E. Urakabe *et al.*, "Beam-Profile Control Using an Octupole Magnet," *Jpn. J. Appl. Phys.* **38** (1999) 6145–6149.

[108] T. Amin, R. Barlow, S. Ghithan, G. Royb, and S. Schuhb, "Formation of a uniform ion beam using octupole magnets for BioLEIR facility at CERN," *JINST* **13** (2018) P04016.

[109] T. D. Arber, K. Bennett, C. S. Brady, A. Lawrence-Douglas, M. G. Ramsay, N. J. Sircombe, P. Gillies, R. G. Evans, H. Schmitz, A. R. Bell, and C. P. Ridgers, "Contemporary particle-in-cell approach to laser-plasma modelling," *Plasma Physics and Controlled Fusion* **57** (2015), no. 11, 113001.

[110] NIST, *NIST Standard Reference Database 124.* National Institute of Standards and Technology, 2017.

[111] D. Krest, L. Laslett, L. W. Jones, K. Symon, and K. Terwilliger, "Fixed field alternating gradient particle accelerators," Tech. Rep. MURA-109, MURA-DWK-KRS-LJL-LWJ-KMT-3, Midwestern Universities Research Association (MURA), 1956.

[112] K. R. Symon, D. W. Kerst, L. W. Jones, L. J. Laslett, and K. M. Terwilliger, "Fixed-Field Alternating-Gradient Particle Accelerators," *Phys. Rev.* **103** (Sep, 1956) 1837–1859.

[113] J. Fourrier, F. Martinache, F. Meot, and J. Pasternak, "Spiral FFAG lattice design tools. Application to 6-D tracking in a proton-therapy class lattice," *Nucl. Instrum. Meth.* **A589** (2008) 133–142.

[114] M. Tanigaki, Y. Mori, M. Inoue, K. Mishima, S. Shiroya, Y. Ishi, and S. Fukumoto, "PRESENT STATUS OF THE FFAG ACCELERATORS IN KURRI FOR ADS STUDY," in *EPAC 2006 - Contributions to the Proceedings.* 2006.

[115] J. B. Lagrange, R. B. Appleby, J. M. Garland, J. Pasternak, and S. Tygier, "Racetrack FFAG muon decay ring for nuSTORM with triplet focusing," *JINST* **13** (2018), no. 09, P09013, `1806.02172`.

[116] Y. Yonemura, H. Arima, N. Ikeda, K. Ishibashi, K. Maehata, T. Noro, T. Okai, K. Sagara, N. Shigyo, Y. Uozumi, G. Wakabayashi, H. Ishikawa, and Kyushu, "Status of center for accelerator and beam applied science of Kyushu University," *EPAC 2008 - Contributions to the Proceedings* (01, 2008).

[117] T. Planche, J. Fourrier, J. L. Lancelot, F. Meot, D. Neuveglise, and J. Pasternak, "Design of a prototype gap shaping spiral dipole for a variable energy protontherapy FFAG," *Nucl. Instrum. Meth.* **A604** (2009) 435–442.

[118] C. Ohmori, F. Méot, and J. Pasternak, "RF System for RACCAM FFAG," in *Particle accelerator. Proceedings, 23rd Conference, PAC'09, Vancouver, Canada, May 4-8, 2009*, p. TU5PFP026. 2010.

[119] C. Brenner and J. Green, "Ion diagnostics for laser-driven ion beam experiments at CLF," *Low energy ion beam diagnostics workshop, Imperial College* (2019).

[120] O. Ettlinger, "Private communication,".

[121] A. Kurup, "Diagnostics for LhARA," *Low energy ion beam diagnostics workshop, Imperial College* (2019).

[122] A. Howard, “The SERENITY Read-Out Board,” *Low energy ion beam diagnostics workshop, Imperial College* (2019).

[123] “Silson.” `http://www.silson.com`.

[124] F. Meot, “RACCAM: An example of spiral sector scaling FFA technology,” *Brookhaven National Laboratory BNL-211536-2019-NEWS* (2019).

[125] R. Doelling, “Diagnostics of the PROSCAN proton therapy beamlines,” *DIPAC, Mainz* (2003).

[126] A. Geisler, “Commissioning of the ACCEL 250MeV proton cyclotron,” *18th International Conference on Cyclotrons and their Applications* (2007).

[127] A. Kalinin, “Diagnostic system commissioning of the EMMA NS-FFAG facility at Daresbury Laboratory,” *IPAC 10, Kyoto* (2010).

[128] S. Koscielniak, “Electron model of linear-field FFAG,” *PAC 05 Knoxville* (2005).

[129] G. Schettino, “Private communication,”.

[130] A. Fews, “High resolution alpha particle spectroscopy using CR39 plastic track detector,” *Nuclear Instruments and Methods* **197** (1982) 517 – 529.

[131] S. Greilich, “Quantitative read-out of Al2O3:C,Mg-based fluorescent nuclear track detectors using a commercial confocal microscope.,”.

[132] A. Piermattei, “Radiochromic film dosimetry of a low energy proton beam,” *Medical Physics* **27** (2000) 1655.

[133] D. Kirby, “LET dependence of GafChromic films and an ion chamber in low-energy proton dosimetry,” *Physics in Medicine and Biology* **55** (2010) 417.

[134] F. Fiorini, “Under-response correction for EBT3 films in the presence of proton spread out Bragg peaks,” *Medical Physics* **30** (2014) 454.

[135] G. Barber, “Outline design and cost estimate for the SmartPhantom,” *Unpublished note* (2018).

[136] “PRaVDA.” `http://www.pravda.uk.com/index.php/78-pgeneral/71-phone`.

[137] A. Burker, “Imaging with ion beams at MedAustron,” *Vienna Conference on Instrumentation* (2018).

[138] E. Gioscio, “Development of a novel neutron tracker for the characterisation of secondary neutrons emitted in Particle Therapy,” *Vienna Conference on Instrumentation* (2018).

[139] R. J. Carter, C. M. Nickson, J. M. Thompson, A. Kacperek, M. A. Hill, and J. L. Parsons, “Characterisation of Deubiquitylating Enzymes in the Cellular Response to High-LET Ionizing Radiation and Complex DNA Damage,” *International Journal of Radiation Oncology*Biology*Physics* **104** (2019), no. 3, 656 – 665.

[140] STFC, “The Astra Gemini Facility.” `https://www.clf.stfc.ac.uk/Pages/The-Astra-Gemini-Facility.aspx`.

[141] STFC, “Introducing The Extreme Photonics Applications Centre.” `https://www.clf.stfc.ac.uk/Pages/EPAC-introduction-page.aspx`.

[142] STFC, “ISIS Neutron and Muon Source.” `https://stfc.ukri.org/research/our-science-facilities/isis-neutron-and-muon-source/`.

[143] J. W. G. Thomason, “The ISIS Spallation Neutron and Muon Source – the first thirty-three years,” *NIM A* **917** (2019) 61–67.

[144] STFC, “Accelerator Science and Technology Centre.” `https://stfc.ukri.org/about-us/where-we-work/daresbury-laboratory/accelerator-science-and-technology-centre/`.

[145] A. Letchford *et al.*, “Status of the RAL Front End Test Stand,” in *IPAC*. 2015.

[146] HSE, *Work with ionising radiation - Ionising Radiations Regulations 2017*. Crown, 2018.

A Project plan

The project plan for LhARA, see figure 54, includes:

- A programme of radiobiology;
- A programme for technology transfer, patient and public involvement, and outreach;
- A five-year R&D programme to address the technical challenges outlined in section 2;
- The schedule for constructing Stage 1 and Stage 2;
- Allocation for a project office; and
- Milestones for the Gateway process.

The radiobiology programme will commence at the start of the LhARA programme and continue through to the end. Work will be done at existing facilities prior to completing construction of LhARA Stage 1, building on existing collaborations and forging new ones. This will help develop techniques for LhARA and at the same time generate scientific output. The staff needed to deliver this are: a work package manager; one PDRA; and one PG student.

The programme of technology transfer for systems, near clinical aspects, and outreach is important to: translate the scientific output generated by LhARA into techniques and devices that can be applied in a clinical environment; involve patient and public participation right from the outset; and to communicate this to various audiences. This approach will help LhARA have a positive impact on clinical radiotherapy as early as possible. To achieve this one coordinator at 20% and one PDRA is needed.

The technical aspects of the five year R&D programme have been detailed in the various subsections on technical challenges within section 2. The staff required to complete the R&D programme include:

- **Facility design:** one work package manager; two engineers; one PDRA; and one PG student. Some this effort will also cover the work needed for Stage 1 R&D, such as performance evaluation and design of the vertical bend.
- **Stage 1 R&D:** three work package managers.
  - *Gabor lens:* two PDRAs; engineering support; and three PG students.
  - *Laser:* one engineer at 30%; one PDRA; and one PG student.
  - *Investigation of space charge:* one PG student.
- **Stage 2 R&D:** two work package managers.
  - *FFA:* one magnet engineer at 50%; one RF engineer at 50%; two PDRAs; and three PG students.
  - *Injection, extraction and performance evaluation:* one PDRA.
  - *Longitudinal phase space and performance evaluation:* one PDRA; one PG student.
  - *Final beam preparation and performance evaluation:* one PG student.
- **End Stations:** work package manager, PDRA, and one PG student. The staff working on the radiobiology programme will also contribute to this at the 50% level.
- **Instrumentation:** one work package manager; two PDRAs; and three PG students.
- **Software and computing:** one work package manager; one technician; one PDRA; and one PG student.

Important milestones in the project plan are:

1. Gateway 0 – strategic assessment;
2. Gateway 1 – business justification;
3. Gateway 2 – delivery strategy;
4. Capture technology choice made;
5. Gateway 3 – investment decision;
6. Completion of Stage 1 construction; and
7. Completion of Stage 2 construction.

The principal ldeliverables of the LhARA project are the:

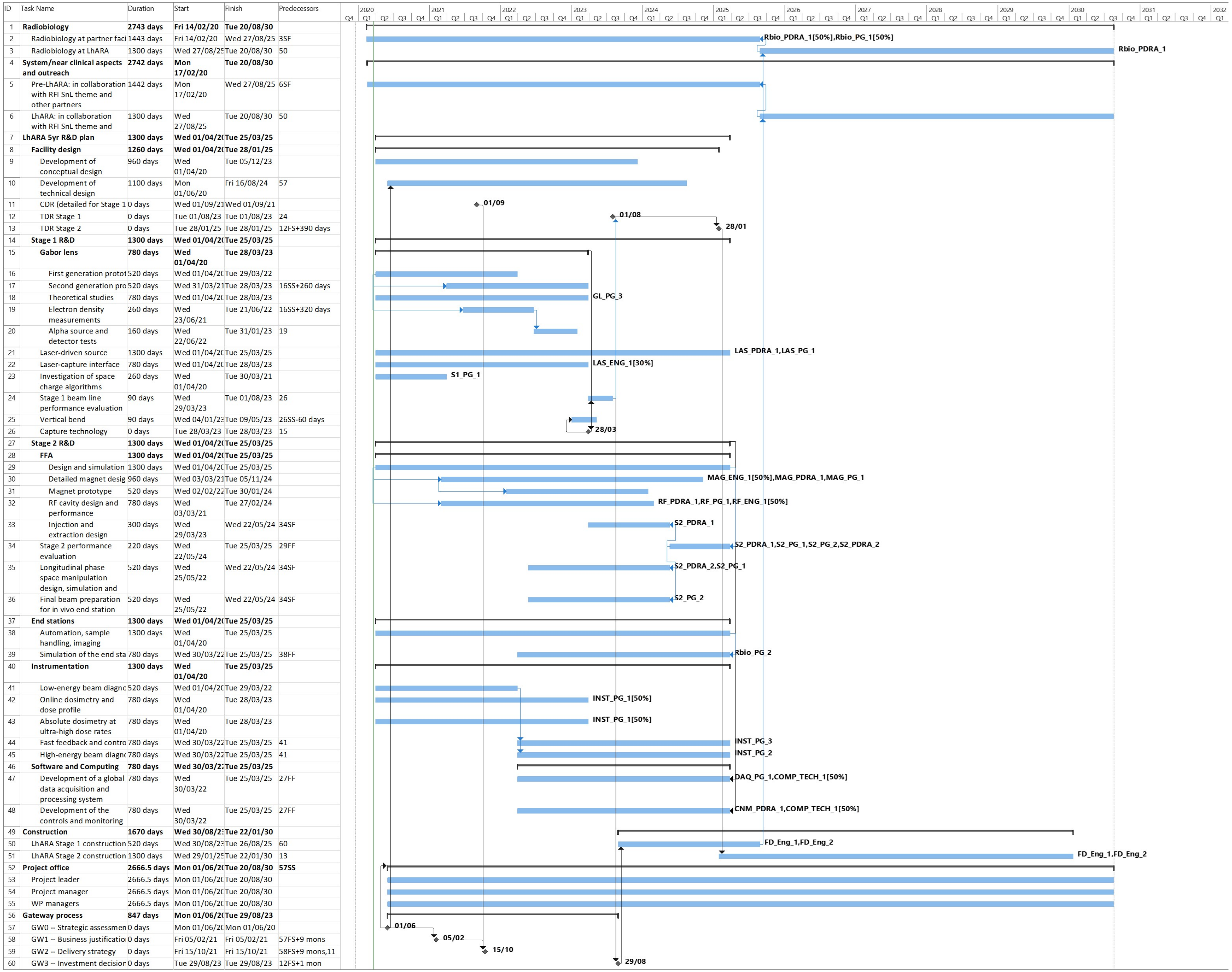

ID	Task Name	Duration	Start	Finish	Predecessors
1	**Radiobiology**	**2743 days**	**Fri 14/02/20**	**Tue 20/08/30**	
2	Radiobiology at partner faci	1443 days	Fri 14/02/20	Wed 27/08/25	3SF
3	Radiobiology at LhARA	1300 days	Wed 27/08/2	Tue 20/08/30	50
4	**System/near clinical aspects and outreach**	**2742 days**	**Mon 17/02/20**	**Tue 20/08/30**	
5	Pre-LhARA: in collaboration with RFI SnL theme and other partners	1442 days	Mon 17/02/20	Wed 27/08/25	6SF
6	LhARA: in collaboration with RFI SnL theme and	1300 days	Wed 27/08/25	Tue 20/08/30	50
7	**LhARA 5yr R&D plan**	**1300 days**	**Wed 01/04/2**	**Tue 25/03/25**	
8	**Facility design**	**1260 days**	**Wed 01/04/2**	**Tue 28/01/25**	
9	Development of conceptual design	960 days	Wed 01/04/20	Tue 05/12/23	
10	Development of technical design	1100 days	Mon 01/06/20	Fri 16/08/24	57
11	CDR (detailed for Stage 1	0 days	Wed 01/09/21	Wed 01/09/21	
12	TDR Stage 1	0 days	Tue 01/08/23	Tue 01/08/23	24
13	TDR Stage 2	0 days	Tue 28/01/25	Tue 28/01/25	12FS+390 days
14	**Stage 1 R&D**	**1300 days**	**Wed 01/04/2**	**Tue 25/03/25**	
15	**Gabor lens**	**780 days**	**Wed 01/04/20**	**Tue 28/03/23**	
16	First generation protot	520 days	Wed 01/04/2	Tue 29/03/22	
17	Second generation pro	520 days	Wed 31/03/21	Tue 28/03/23	16SS+260 days
18	Theoretical studies	780 days	Wed 01/04/2	Tue 28/03/23	
19	Electron density measurements	260 days	Wed 23/06/21	Tue 21/06/22	16SS+320 days
20	Alpha source and detector tests	160 days	Wed 22/06/22	Tue 31/01/23	19
21	Laser-driven source	1300 days	Wed 01/04/2	Tue 25/03/25	
22	Laser-capture interface	780 days	Wed 01/04/2	Tue 28/03/23	
23	Investigation of space charge algorithms	260 days	Wed 01/04/20	Tue 30/03/21	
24	Stage 1 beam line performance evaluation	90 days	Wed 29/03/23	Tue 01/08/23	26
25	Vertical bend	90 days	Wed 04/01/2	Tue 09/05/23	26SS-60 days
26	Capture technology	0 days	Tue 28/03/23	Tue 28/03/23	15
27	**Stage 2 R&D**	**1300 days**	**Wed 01/04/2**	**Tue 25/03/25**	
28	**FFA**	**1300 days**	**Wed 01/04/2**	**Tue 25/03/25**	
29	Design and simulation	1300 days	Wed 01/04/2	Tue 25/03/25	
30	Detailed magnet desig	960 days	Wed 03/03/21	Tue 05/11/24	
31	Magnet prototype	520 days	Wed 02/02/2	Tue 30/01/24	
32	RF cavity design and performance	780 days	Wed 03/03/21	Tue 27/02/24	
33	Injection and extraction design	300 days	Wed 29/03/23	Wed 22/05/24	34SF
34	Stage 2 performance evaluation	220 days	Wed 22/05/24	Tue 25/03/25	29FF
35	Longitudinal phase space manipulation design, simulation and	520 days	Wed 25/05/22	Wed 22/05/24	34SF
36	Final beam preparation for in vivo end station	520 days	Wed 25/05/22	Wed 22/05/24	34SF
37	**End stations**	**1300 days**	**Wed 01/04/2**	**Tue 25/03/25**	
38	Automation, sample handling, imaging	1300 days	Wed 01/04/20	Tue 25/03/25	
39	Simulation of the end sta	780 days	Wed 30/03/2	Tue 25/03/25	38FF
40	**Instrumentation**	**1300 days**	**Wed 01/04/20**	**Tue 25/03/25**	
41	Low-energy beam diagno	520 days	Wed 01/04/2	Tue 29/03/22	
42	Online dosimetry and dose profile	780 days	Wed 01/04/20	Tue 28/03/23	
43	Absolute dosimetry at ultra-high dose rates	780 days	Wed 01/04/20	Tue 28/03/23	
44	Fast feedback and contro	780 days	Wed 30/03/2	Tue 25/03/25	41
45	High-energy beam diagn	780 days	Wed 30/03/2	Tue 25/03/25	41
46	**Software and Computing**	**780 days**	**Wed 30/03/2**	**Tue 25/03/25**	
47	Development of a global data acquisition and processing system	780 days	Wed 30/03/22	Tue 25/03/25	27FF
48	Development of the controls and monitoring	780 days	Wed 30/03/22	Tue 25/03/25	27FF
49	**Construction**	**1670 days**	**Wed 30/08/2**	**Tue 22/01/30**	
50	LhARA Stage 1 construction	520 days	Wed 30/08/2	Tue 26/08/25	60
51	LhARA Stage 2 construction	1300 days	Wed 29/01/2	Tue 22/01/30	13
52	**Project office**	**2666.5 days**	**Mon 01/06/2**	**Tue 20/08/30**	**57SS**
53	Project leader	2666.5 days	Mon 01/06/2	Tue 20/08/30	
54	Project manager	2666.5 days	Mon 01/06/2	Tue 20/08/30	
55	WP managers	2666.5 days	Mon 01/06/2	Tue 20/08/30	
56	**Gateway process**	**847 days**	**Mon 01/06/2**	**Tue 29/08/23**	
57	GW0 -- Strategic assessmen	0 days	Mon 01/06/2	Mon 01/06/20	
58	GW1 -- Business justificatio	0 days	Fri 05/02/21	Fri 05/02/21	57FS+9 mons
59	GW2 -- Delivery strategy	0 days	Fri 15/10/21	Fri 15/10/21	58FS+9 mons,11
60	GW3 -- Investment decision	0 days	Tue 29/08/23	Tue 29/08/23	12FS+1 mon

Figure 54: Gantt chart for the LhARA project.

1. Full lConceptual Design Report;
2. Technical Design Report for Stage 1; and
3. Technical Design Report for Stage 2.

The project office will be created when the Gateway 0 milestone is achieved. It will look after the administrative aspects of the project and will require one person to administer the project and provide support for the project leader, the project manager and the work package managers. The conceptual design report deliverable will be an input to achieve the "Gateway 2 – delivery strategy" milestone and the technical design report for Stage 1 will be an input to achieve the "Gateway 3 – investment decision" milestone. The Construction of Stage 1 will commence after the investment decision is made and construction of Stage 2 will commence after the technical design report for Stage 2 has been completed.

Capital resources for the project and the total FTEs required are detailed in Appendix B.

B Costs

The top-level breakdown of the capital costs for the LhARA project is given in table 10. The costs presented in this appendix should be regarded as first estimates that will be challenged and refined as the full CDR, and subsequently the Technical Design Reports for Stage 1 and Stage 2 are developed. The following subsections include further detail and breakdown of these costs.

Description	**Optimistic cost (£k)**	**Most likely cost (£k)**	**Pessimistic cost (£k)**
Laser	2197	2746	3295
Capture	409	545	681
Stage 1	607	759	1139
Stage 2	6924	8656	12984
End stations	799	999	1198
Integration	2612	3265	4898
R&D	400	500	600
Safety	595	850	1275
Building	4060	9160	18320
Installation and commissioning			
Total	18603	27480	44390
Total (incl. VAT)	22324	32976	53268

Table 10: Cost breakdown for the LhARA project.

Details of the staff effort required is given in section B.12. The uncertainty on the cost is based on the method used to derive the cost for each item. This is categorised as: guess, comparative, parametric, budget price from a supplier and firm quote from a supplier.

B.1 Laser

The cost for the laser system was derived using a bottom up approach and known costs, where available. A summarised cost breakdown for the laser system is given in Table 11.

Description	Optimistic cost (£k)	Most likely cost (£k)	Pessimistic cost (£k)
Laser	1967	2458	2950
Chambers and Vacuum System	39	49	59
Laser Plasma Accelerator	82	102	123
Leakage Laser Diagnostics	21	26	32
Cameras	39	49	59
Proton Spectrometer	7	8	10
Motorised stages	20	25	30
Pointing Stabilisation System	2	3	3
Computing	5	6	7
General Electrical	16	19	23

Table 11: Cost breakdown for the laser system.

B.2 Capture

The cost breakdown for the capture system that is based on Gabor lenses is given in Table 12. In the event that after studying the Gabor lens it is decided to use an alternative technology for the capture, then the cost is likely to increase.

Description	Optimistic cost (£k)	Most likely cost (£k)	Pessimistic cost (£k)
Gabor Lens (x5 @ £100 each)	375	500	625
Power Supply (x5 @ £3k each)	11.25	15	18.75
Cooling	22.5	30	37.5

Table 12: Cost breakdown for the capture system.

B.3 Stage 1

The cost for Stage 1 was derived using a combination of comparative, parametric and budget price methods. The magnet, power supplies and beam dump costs have been compared to equipment of approximately equal size and use at ISIS. The beampipe, frames and rails have been parametrically determined from costs of new proton beamlines under development at ISIS. The cost of diagnostics has been based on budgetary prices from suppliers for a specified quantity of installations. The breakdown of the cost for Stage 1 is given in Table 13.

B.4 Stage 2

The cost for Stage 2 was derived using a combination of comparative, parametric, guess and budget price methods. The quadrupole and dipole magnets, power supplies and beam dump costs have been compared to equipment of approximately equal size and use at ISIS. The beampipe, frames and rails have been parametrically determined from costs of new proton beamlines under development at ISIS. The FFA magnets and RF cavities have been estimated via guesses, while also comparing to the most closely comparable equipment in use at ISIS. The cost of diagnostics has been based on budgetary prices from suppliers for a specified quantity of installations. The breakdown of the cost for Stage 2 is given in Table 14.

Description	**Optimistic cost (£k)**	**Most likely cost (£k)**	**Pessimistic cost (£k)**
Quadrupole Magnets (x12 @ £10k each)	96	120	180
Dipole Magnets (x9 @ £10k each)	72	90	135
Power Supplies (x21 @ £3k each)	50	63	95
Beam Dump	24	30	45
Beampipe (12m @ £3k/m)	29	36	54
Frames (12m @ £5k/m)	48	60	90
Rails (12m @ £5k/m	48	60	90
Diagnostics (12m @ £25k/m)	240	300	450

Table 13: Cost breakdown for Stage 1.

Description	**Optimistic cost (£k)**	**Most likely cost (£k)**	**Pessimistic cost (£k)**
Quadrupole Magnets (x20 @ £10k each)	192	240	360
Dipole Magnets (x10 @ £10k each)	80	100	150
Power Supplies (x32 @ £3k each)	77	96	144
Beam Dump (x2 @ £15k each)	48	60	90
FFA Magnets (x10 @ £250k each)	2000	2500	3750
FFA magnet power supply (x10 @ £75k each)	600	750	1125
RF Cavities (x4 @ £300k each)	960	1200	1800
RF Power supply/drive system (x4 at £400k each)	1280	1600	2400
Kicker Magnets (x2 @ £200k each)	320	400	600
Septum Magnets (x2 @ £200k each)	320	400	600
Kicker & Septum power supplies (x4 @ £60k each)	192	240	360
Bunching Cavities (x4 @ £30k each)	96	120	180
Beam pipe (25m @ £3k/m)	60	75	113
Frames (25m @ £5k/m)	100	125	188
Rails (25m @ £5k/m	100	125	188
Diagnostics (25m @ £25k/m)	500	625	938

Table 14: Cost breakdown for Stage 2.

B.5 End stations

The cost breakdown for the end stations is the cost to equip the end stations, see Table 15. These costs have been based on budget prices from suppliers. The costs for other equipment such as consumables is not included and the cost for the end station automation is included in the costs for the R&D programme.

Description	**Optimistic cost (£k)**	**Most likely cost (£k)**	**Pessimistic cost (£k)**
Refrigerated centrifuge (x2) - Eppendorf 5804R	9.6	12	14.4
Refrigerated ultracentrifuge - Beckman Coulter Optima MAX-XP	40	50	60
Hypoxia chamber - Baker InvivO2/Don Whitley	32	40	48
Ice Flaker machine - Scotsman AF80	2	2.5	3
CellRad x-ray irradiator - Faxitron	56	70	84
Class II cell culture cabinet (x4) - Esco Airstream	22.4	28	33.6
Digital microscope - Invitrogen EVOS M5000	16	20	24
Light microscopes (x3) - Nikon Eclipse TS100	7.2	9	10.8
CO2 cell incubator (x2) - Panasonic	11.2	14	16.8
Fridges/-20°C Freezers (4 each)	1.6	2	2.4
-80°C Freezers (x2) - Panasonic	16	20	24
MilliQ water - Avidity 60L	4.8	6	7.2
Colony counter - Oxford Optronix GelCount	20	25	30
Fluorescence microscope/Live cell imaging	80	100	120
Robotic workstation (research laboratory) – Tecan/Beckman	160	200	240
End station cabinet (hypoxia enabled) - BakerRuskinn/Don Whitley	160	200	240
Robotics within end station cabinets (x2)	160	200	240

Table 15: Cost breakdown for the end stations.

B.6 Integration

The costs for the integration were estimated using comparative and parametric methods based on new proton beamline projects currently in development at ISIS. The costs for integration are given in Table 16.

B.7 R&D

The costs for R&D were derived using a combination of comparative and guess methods. Material costs for computing includes cost for CPU nodes as well as infrastructure related costs such as networking (including cable pulling), etc. The costs for the R&D are given in Table 17.

Description	Optimistic cost (£k)	Most likely cost (£k)	Pessimistic cost (£k)
Vacuum systems (35m @ £34k/m)	952	1190	1785
Electrical services (35m @ £25k/m)	700	875	1312.5
Water services (35m @ £20k/m)	560	700	1050
Control system	400	500	750

Table 16: Cost breakdown for integration.

Description	Optimistic cost (£k)	Most likely cost (£k)	Pessimistic cost (£k)
Gabor lens prototype material	200	250	300
Computing hardware	160	200	240
Instrumentation prototype hardware	40	50	60

Table 17: Cost breakdown for the R&D programme.

B.8 Safety

The costs for the necessary safety systems have been based on parametric and comparative methods using examples from safety systems at ISIS. The costs for the safety systems are given in Table 18.

Description	Optimistic cost (£k)	Most likely cost (£k)	Pessimistic cost (£k)
Shielding	385	550	825
Access Controls and PPS	210	300	450

Table 18: Cost breakdown for the safety system.

B.9 Building

The building cost was derived from the actual cost for a building of comparable size to that needed for LhARA. The optimistic cost for the building structure is listed as zero in the event that an existing building can be re-purposed for use with LhARA. The supporting works, such as mechanical and services, would still be required for this existing building. The costs for the building requirements are given in Table 19.

B.10 Installation and commissioning

The cost breakdown for installation and commissioning is given in Table 20. This cost covers global installation, commissioning and integration costs. Installation and commissioning costs for specific equipment will be included in the cost of that item.

B.11 Project

There are no specific capital costs envisaged to managed the project. There is one person included in the project plan to administer the project and provide support for the project leader, project manager and work package

Description	**Optimistic cost (£k)**	**Most likely cost (£k)**	**Pessimistic cost (£k)**
Building structure	0	3360	6720
Mechanical and electrical	980	1400	2800
Externals and services	1750	2500	5000
Enabling and preparation works	980	1400	2800
Cranes	350	500	1000

Table 19: Cost breakdown for building.

Description	**Optimistic cost (£k)**	**Most likely cost (£k)**	**Pessimistic cost (£k)**

Table 20: Cost breakdown for the laser system.

managers and this is included in the staff requirements detailed in section B.12.

B.12 Staff

The required staff effort is given in Table 21 in terms of FTEs needed for the different roles specified in the project plan, see section A. Thus this only includes staff where specific positions have been identified. It is expected that more effort will be needed, especially for construction, though to determine this with any confidence requires a more detailed analysis of the project plan. A rough guide for the number of FTEs needed for this can be taken from past experience and is expected, in terms of cost, to be of the same order as the capital cost.

Type of position	**Number of FTEs**
Academic	10.7
Administrative	10.3
Engineering	27.9
Post-doctoral Research associate	61.2
Post-graduate student	50.7
Technical/support	5.1

Table 21: Breakdown of the staff effort estimated as required for the execution of the LhARA project.

It should be noted that the academic FTEs are for work package managers, which have been included in the project plan at 20%. Other academic effort, for example for supervising students and providing specific technical expertise, is not included but will be required.